UNIVERSIDAD MIGUEL HERNÁNDEZ DE ELCHE

ESCUELA POLITÉCNICA SUPERIOR DE ELCHE

Máster Universitario de Investigación en Tecnologías Industriales y de Telecomunicación

Especialización en Robótica, Automática y Electrónica

"Design of an optical fibre based angular position sensor for wire scanners complying with ultra-high vacuum, high temperature and radiation conditions of the CERN´s accelerators"

TRABAJO FIN DE MASTER

Septiembre 2012

AUTOR*: Jose Luis Sirvent Blasco*

DIRECTORES*:*
José María Azorín Poveda(UMH)
Jonathan Emery(CERN)

MASTER UNIVERSITARIO DE INVESTIGACIÓN EN TECNOLOGÍAS INDUSTRIALES Y DE TELECOMUNICACIÓN

VISTO BUENO DEL DIRECTOR Y PROPUESTA DE EVALUADORES

Título proyecto:

Design of an optical fibre based angular position sensor for wire scanners complying with ultra-high vacuum, high temperature and radiation conditions of the CERN´s accelerators

MATERIA DE ESPECIALIZACIÓN:

☐Electrónica & Comunicaciones
☐Mecánica & Materiales
☐Óptica & Fotónica
✔Robótica & Automática

Proyectante:
Jose Luis Sirvent Blasco

Director/es:
José María Azorín Poveda (UMH)
Jonathan Emery (CERN)

Evaluadores propuestos:
Dos profesores del Master propuestos como posibles miembros del Tribunal evaluador.
José María Sabater Navarro
Carlos Pérez Vidal

VºBº director/es del proyecto:

Fdo.: José María Azorín Poveda

Fdo.: Jonathan Emery

Lugar y fecha:

Elche, 05 Septiembre 2012

Acknowledgements

In the personal field I would like to give my most special acknowledgement to my girlfriend Angela for being there always it was necessary, I thank her very much to share this experience with me coming to France, and all her patience during the first weeks in particular and this whole year living together in general. Her sympathy and constant support has always been the key to overcome the inevitable some not so good moments, and stress that a research project involves sometimes. I couldn't forget to thank to my parents and family who always trusted in me and whose unconditional support I really appreciate, finally I would also like to thank my little sister Maria and sister-in-law Irene, we really spent a very good time during their visit.

In the professional field I would like to express my gratitude to Mr. Jonathan Emery, who constantly supervised very closely this project from beginning to end, since the proposition of the topic (…interview by Skype included) to the amount of time spent during the revision of this thesis. His advice about signal processing and electronics has been a very important contribution for the thesis development. I also appreciate very much his support and suggestions, the stimulating conversations during the coffee time and his motivation after each new measurement. I'm also sincerely thankful to Dr. Bernd Denhing for giving me the opportunity to join in the design team for this Wire Scanner, his support and wisdom has introduced me to the fascinating world of the Beam Instrumentation. His constant supervision has been essential to develop this project, his advice has been the light that guided the steps followed during the thesis, even if there are hundreds of things to do, he always had a gap for me, I appreciate very much his effort with the definition of my next academic adventure, the PhD. I also would like to acknowledge in general to all those great people from the CERN BE/BI-BLM group that made me feel like one more of the family from the first day I arrived at my office.

I would like to acknowledge in particular Dr. Jose Maria Azorin my academic supervisor, who initially introduced me in the research world and who have followed closely this project; I appreciate very much his support and consideration when new opportunities were available in the NBio Group. I couldn't forget to thank to Andres Úbeda, great friend and college for all his help during the printing process of this thesis and the paperwork I needed to do from the distance and Dr. Ausias Sirvent, who initially encouraged me to apply for this great experience, the Technical Student Programme at CERN.

TABLE OF CONTENTS

CHAPTER 1

Particle Accelerators at CERN

CHAPTER 2

Wire scanners at CERN

CHAPTER 3

Context and objectives of the thesis

CHAPTER 4

Theoretical concepts

CHAPTER 5

Component selection and analysis

CHAPTER 1

Particle Accelerators at CERN

During this chapter CERN'S facilities will be described, acting as an introductory chapter important concepts such as the basics of a particle accelerator, luminosity and the importance of the beam monitorization will be explained. Here it will also be exposed the beam profile measuring devices installed at CERN and their main characteristics.

1. Introduction

CERN is the European Organization for Nuclear Research, one of the world most influential particle physics center. Founded in 1954, the laboratory was one of Europe's first joint ventures, and has become a shining example of international collaboration. From the original 12 signatories of the CERN convention, membership has grown to the present 20 Member States.

CERN's history is bound up with the construction of large accelerators: the Synchro-Cyclotron (SC, 1957) and the Proton Synchrotron (PS, 1959) were followed by the Intersecting Storage Rings (ISR, 1971), the Proton Synchrotron Booster (PSB, 1972) and the Super Proton Synchrotron (SPS, 1976). From 1981 the SPS was operated as proton-antiproton collider. In 1983 it allowed the discovery of the W-bosons and the Z-boson, the carriers of the weak nuclear force, thus confirming the theory of electro-weak interactions and unifying the weak and electromagnetic forces.

The Large Electron-Positron storage ring (LEP) was completed in 1989 and was installed in a tunnel of 27km circumference, located between 80 and 150 m underground. It was operated between 1989 and 2001 and lead to the experimental verification of several elements of the Standard Model, such as the Z and W bosons mass accurate determination.

The Large Hadron Collider (LHC) [1] is accommodated in the same tunnel that housed the LEP, once the LEP was completely disassembled the tasks to mount the complete LHC started, giving his first results in 2005 by using the LHC computing Grid. As CERN's first accelerators were catalysts for European collaboration, the LHC sets a precedent for a worldwide collaboration in physics research, and was the main tool used in the search of the Higgs boson, whose existence has been recently proved recently in 2012.

1.1.1 The LHC, injectors and experiments.

The LHC is accommodated in a 27 km tunnel that used to house previously the LEP; this tunnel is located in the region between the Geneva airport and the nearby Jura Mountains, the LHC is the most powerful tool for Particle Physics research. It is designed to collide proton beams with a centre-of-mass energy of 14 TeV and an unprecedented luminosity of 10^{34} cm^{-2} s^{-1}. It can also collide heavy (Pb) ions with an energy of 2.8 TeV per nucleon and a peak luminosity of $10^{27} cm^{-2}$ s^{-1}.

The LHC working principle is based in an injector chain shown in the Figure 1.1 this chain is the responsible of supplying the LHC with protons. These protons are generated by a *Duoplasmatron source,* after they are injected in the *Linac*. The linac is a beam transport line of about 80m along in which the particles are accelerated to 50MeV and grouped in buckets by mean of radio frequency cavities. The next step is to inject the protons in the *Proton Synchrotron Booster (PSB)*, a 157m circumference device capable of accelerating high intensity beams up to 1.4 GeV, from the PSB the particles are transferred to the *Proton Synchrotron (PS)*, a 628m circumference ring, where they are accelerated to 26 GeV.

All this process is done at ground level, after, a beam transport line connects the PS to the *Super Proton Synchrotron (SPS)*, which has a circumference of 6.9km and lays at about 50m underground. In the SPS the beam energy increases from 26 to 450 GeV.

The particles beams will be injected from the SPS to the LHC via two transfer lines to establish two circulating beams in opposite directions in order to collide these beams into each other.

There are several experiments around him in order to study the particle collisions from a different point of view, the experiments ATLAS, CMS, ALICE and LHC-b.

ATLAS (A Toroidal LHC AparatuS) [2] and CMS (Compact Muon Solenoid) [5] which was conceived to study proton-proton (and lead-lead) collisions at a centre-of-mass energy of 14 TeV and at luminosities up to $10^{34}cm^{-2}s^{-1}$, could be considered general pourpose detectors, ALICE (A Large Ion Collider Experiment) [3] is another detector specialized in heay-ion which address the physics of strongly interacting matter and the quark-gluon plasma at extreme values of energy density and temperature. Finally LHC-b (Large Hadron Collider beauty experiment) [4] was conceived to precision measurements of CP violation and rare decays of B hadrons in the LHC. The location of the four experiments is also shown in the Figure 1.1.

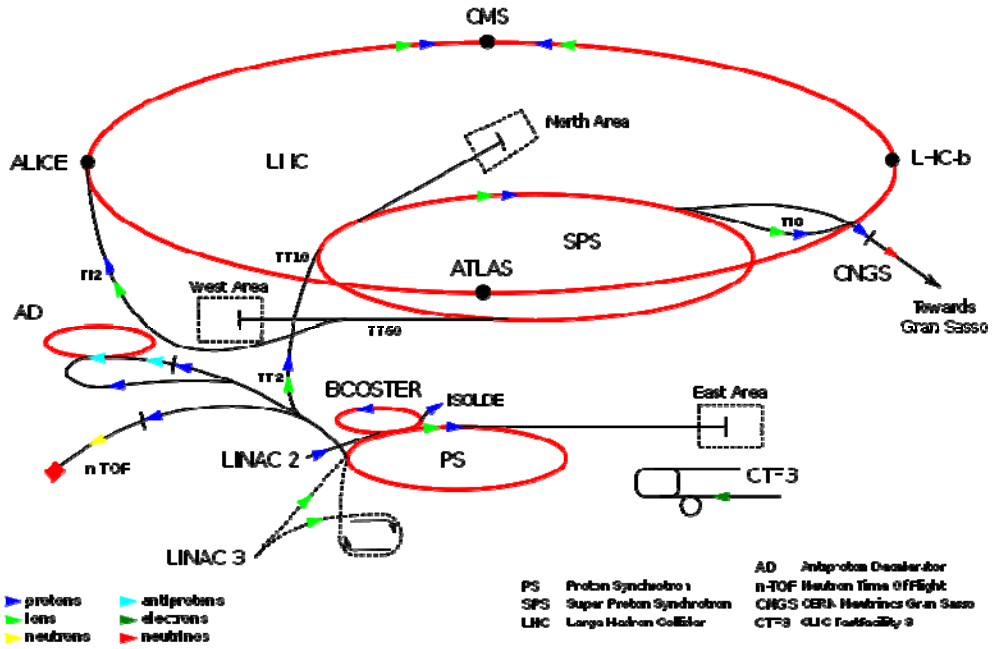

Figure 1.1 *Cern's facilities scheme.*

1.1.2 The basics of a particle accelerator

The basic conception of an accelerator starts assuming a constant energy and high stable beam trajectory. The elements of the machine are designed in such way that the particles are guided along an ideal reference path, then accelerated and strongly focused at particular locations designed for collision.

A high energy accelerator complex is composed of ion sources, bruncher/debruncher, chopper, pre-accelerators such as the high-voltage source or FRQ, drift-tube linac (DTL), booster synchrotrons, storage rings and colliders. Particle beams are produced from ion sources, where charged ions are extracted by a high-voltage source to form a beam. Before injection into various types of accelerators, the beam pulse is usually prebunched and chopped into apporpiate sizes. The beam can be accelerated by a DC accelerator or RFQ to attain the proper velocity needed for a drift-tube linac. The beams can be injected into a chain of synchrotrons to reach high energy [6].

The elements responsible for the guiding of the beam particles along the reference path are the accelerator magnets, the most important kind of magnets used in accelerators to create the guiding fields are the dipole and quadrupole magnets, this magnets produce

electromagnetic forces to the charged particles in order to provide certain trajectory and bend the beam, while the RF cavities provide acceleration. However in practice it is not possible to keep all the particles in the same trajectory, in general, the beam is populated by a number of particles performing small amplitude oscillations around the reference orbit. The guiding of the charged particles is done by applying electromagnetic forces in certain directions, by applying the principles of the Lorentz law, which describes the force acting on a particle or charge e travelling in an electromagnetic field

$$\vec{F} = e(\vec{E} + \vec{v} \times \vec{B})$$

where E and B are the electric and magnetic fields, and v the particle's speed.

In general two kind of fields are used along the accelerator, longitudinal electric fields are mainly used to accelerate the particles and transversal magnetic fields, which are responsible of the bending and focusing of the beam.

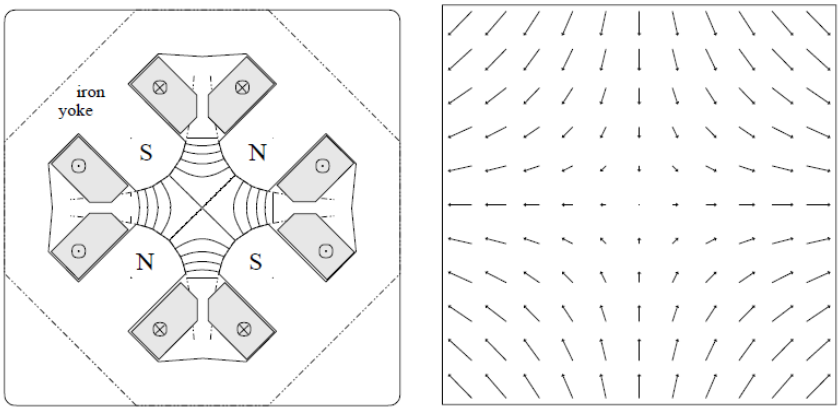

Figure 1.2: *Cross section of a quadrupole magnet with indicated the magnetic field lines and Lorentz forces in vectorial representation. The force felt by a particle is increasing with the distance from the magnet center [7].*

As it is visible in the Fig.1.2 the forces applied in a quadrupole affects only to the particles surrounding the center (the particles that are already there does not experiment any variation), giving as a result the focusing in just in one plane, while defocusing in the other. In order to compensate this problem the most common scheme in accelerators is to use alternated quadrupoles with opposite polarities, which provide this way a focusing effect in the two transverse directions, this structure is also known as FODO cells. This cells consists on a horizontal focusing quadrupole (F), a drift space (O), horizontal

defocusing (D) quadrupole, and another drift space. The bending dipoles are placed in between the quadrupoles, the final effect is the focusing of the beam. On the other hand, the dipoles are used to guide charged particle beams along a desired orbit.

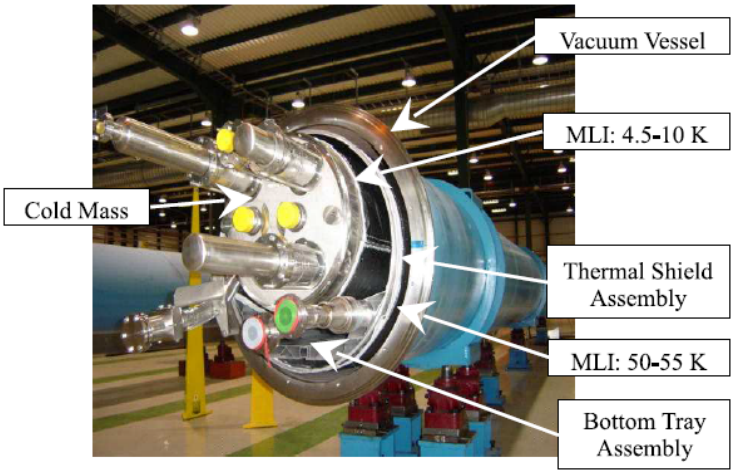

Figure 1.3: *Example of LHC dipole cryomagnet assembly. [1]*

The advances reached at CERN in the field of particle physics and accelerators are not only applied in research areas as it's usually though, the discoveries and improvements of the existing systems could be applied later to the industry. It is widely known the case of the security issues in the airports where the radiation is used to detect unwanted objects in the luggage of the travellers. The particle beams have also been used to detect defects and metal fatigue of airplanes, ships and strategic equipment. In the case of the medicine, the most obvious is radiotherapy where X-ray machine is the simplest accelerator as an example. Circular accelerators initially designed for research purpose are also applied in medicine with some modifications; this is the case of the betatron, microtron (for x-ray and electron beam radiotherapy), cyclotron (for proton and neutron radiotherapy) and synchrotron (for hadrons radiotherapy). Even linear accelerators (linacs) have been used in the past few decades as the predominant machine in treatment of cancer with ionizing radiation, this linacs, mounted isocentrically allow practical radiation treatment aiming the beam toward the patient from various directions to concentrate the dose in the tumour and spare healthy tissues as much as possible. [8]

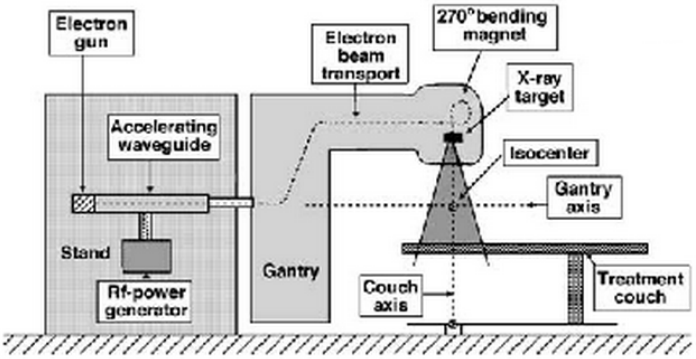

Figure 1.4: *Example of Design configuration for isocentric medical linac. [8]*

1.1.3 Luminosity

The research done at CERN works with the highest standards and with the best quality possible, in terms of particle accelerators the parameter which measures their quality is the luminosity.

When working with beams collisions it is very important to reach the highest number of useful interactions or events to increase the statistics and reduce the time between rare events, and even more taking into account that the rare events studied has a very small cross section Op. The luminosity is the magnitude that measures the ability of a particle accelerator to produce the required number of interactions; this is also a proportional factor between the number of events per second dR/dt and the cross section Op. As a certain beam quality is necessary to achieve optimum conditions for running experiments it is highly recommendable to reach the highest luminosity possible. The higher this rate is, the lower the statistical error of a measured particle parameter. See Fig 1.3 for a comparison between colliders.

	Energy (GeV)	$\mathcal{L}$ $cm^{-2}s^{-1}$	rate s^{-1}	$\sigma x/\sigma_y$ $\mu m/\mu m$	Particles per bunch
SPS ($p\bar{p}$)	315x315	$6\ 10^{30}$	$4\ 10^{5}$	60/30	$\approx 10\ 10^{10}$
Tevatron ($p\bar{p}$)	1000x1000	$50\ 10^{30}$	$4\ 10^{6}$	30/30	$\approx 30/8\ 10^{10}$
HERA (e^+p)	30x920	$40\ 10^{30}$	40	250/50	$\approx 3/7\ 10^{10}$
LHC (pp)	7000x7000	$10000\ 10^{30}$	10^{9}	17/17	$11\ 10^{10}$
LEP (e^+e^-)	105x105	$100\ 10^{30}$	≤ 1	200/2	$\approx 5\ 10^{11}$
PEP (e^+e^-)	9x3	$3000\ 10^{30}$	NA	150/5	$\approx 2/6\ 10^{10}$
KEKB (e^+e^-)	8x3.5	$10000\ 10^{30}$	NA	77/2	$\approx 1.3/1.6\ 10^{10}$

Table 1.1: *Example of different colliders. It is shown the energy, luminosity, beam sizes and interaction rate for a comparison. [9]*

According to [9] the luminosity L can be calculated by:

$$L = f_{rev} n \frac{N_1 N_2}{4\pi\sigma_H \sigma_V} \qquad (1)$$

Where f_{rev} is the revolution frequency, n is the number of brunches in one beam, N the number of particles in each brunch and $\sigma_{H,V}$ are the horizontal and vertical transverse beam dimensions. This shows that the luminosity is inversely proportional to the beam size at the collision points. It is not possible to measure the beam size at this position, so it is measured elsewhere and then the emittance of the beam is calculated. The emittance is constant around the ring and allows relating a beam size measurement done at any location of the ring to the beam size at the interaction point.

At this point wire scanners plays an important role, the wire scanners are able to measure the transverse beam size σ, which will be explained later, in both planes, horizontal and vertical, recovering this way the beam emittance.

1.2 The importance of transverse beam distribution measurements

Measuring the beam transverse emittance is of relevant interest in every accelerator complex, in order to allow the characterization of one of the key parameters for high luminosity performance. The projection of the distribution n(*u*) of the particles in the beam on the coordinate *u* in the phase space (*u*, *u0*) defines the beam profile (See Fig.1.5). The r.m.s. sizes of the Gaussian beam at the point of measurement, H for horizontal (*u* = *y*) and V for vertical (*u* = *z*), are written then for a non-dispersive region:

$$\sigma_{H,V} = \sqrt{\beta_{H,V}\, \epsilon_{H,V}} \qquad (2)$$

With $\beta_{H,V}$ the horizontal or the vertical betatron function and $\epsilon_{H,V}$ the horizontal or vertical emittance.

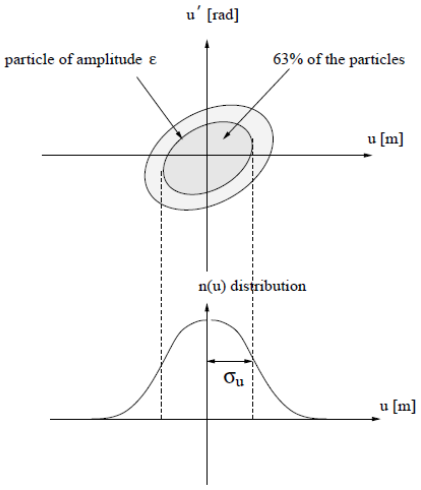

Figure 1.5: *Definition of the beam profile and projection on the h and V planes of the particle distribution [10].*

For the control of the machine, it is important to know precisely the transverse dimensions of the beams $\sigma_{h,v}$. Since the emittance is an invariant of the beam, the knowledge of $\sigma_{h,v}$ and $\beta_{H,V}$ at a given point of the circumference yields the emittance $\epsilon_{H,V}$ with Eq. (2).

Along the trajectory, the ellipse represented for the beam is continuously changing in shape and orientation, but its surface remains constant and it returns to its initial shape after having described one complete period.

1.3 Beam profile measurement devices

There are several devices already installed at CERN and working with the different accelerators in order to measure the transversal beam density distribution. Some devices could measure it in a constant way and give a constant monitorization, meanwhile others such as the wire scanners are used for calibration and are not able to provide information in real time. These measurement devices could be classified in two categories: perturbative (where there is a direct interaction of matter with the beam and by this interaction, generation of secondary particles and beam losses), and non-perturbative (where the measurement is done without direct interaction with the beam and no loses are produced)

Wire scanner: When a thin wire crosses the beam, secondary electrons of low energy are emitted by the wire, thus creating an induced current in the wire which can then be measured. Secondary particle are also emitted which can be measured by means of a scintillator. This system has a good resolution and it is used to calibrate the other

instruments (due to its high precision), such as the BGI and BSR, over the whole energy range of the LHC beam by using a reduced number of bunches. This measurement is perturbative and will create a beam blow-up. In addition, a study carried out at CERN [11] showed that this system could not be used with the nominal intensity in the LHC since the heat produced will destroy the wire. During this project it will be shown more in detail the working principle of the wire scanners as well as the improvements expected with the new design.

Beam Gas Ionization Monitors (BGI): the beam ionizes the residual gas in the vacuum chamber around 10−8 Pa. An electric field separates the ions and the emitted electrons [13]. Electrons, guided by a magnetic field to limit the angular divergence, or the ions, are collected and the signal is amplified by a multichannel plate (MCP). The electrons produced by the MCP are accumulated onto a screen of phosphorus and one observes the emitted light. This system has a higher efficiency than luminescence but may suffer from space charge effects. This technique is non-perturbative if no gas is injected (as in the case of the LHC), but requires a cross-calibration with the wire scanners.

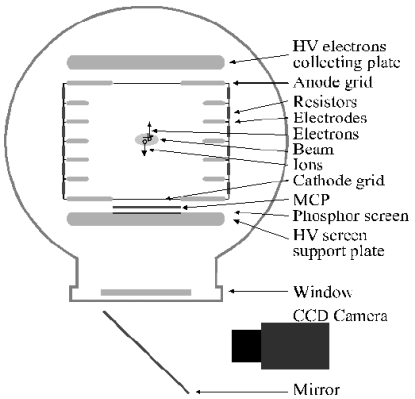

Figure 1.6: *Scheme of a BGI monitor [13]*

Luminescence: A gas (nitrogen N2) is injected into the vacuum chamber [12]. As the beam passes through, the gas molecules are ionized and excited in N+2 ions which are de-excited by emitting photons of 391.4 nm wavelength. The direct observation of the emitted photons makes it possible to measure the beam profile. It is a simple device, but with a low sensitivity due to the low efficiency of luminescence. It should be of interest for high density beams.

Synchrotron Radiation Monitors (BSRT): The synchrotron light monitor profits from the radiation emitted by the accelerated particles to image the transverse beam distribution. This technique avoids any interaction with the beam but, depending on the particles mass and energy, may require the installation of additional bending elements to generate enough radiation. Its absolute calibration is rather difficult but possible by means of using wire scanners [14]. When passing through a magnetic bending element, the beam emits radiation of which the visible spectral part is used and focused on a detector (Intensifier and CCD) by an optical system described in the Fig 1.7.

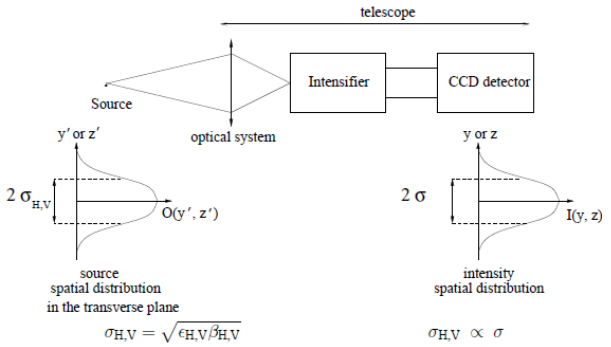

Figure 1.7: *Principle of the synchrotron radiation monitor [9]*

CHAPTER 2

Wire scanners at CERN

In order to understand the main characteristics of the wire scanners and their limitations, this chapter will explain in detail its working principle and the different models installed at CERN.

2.1. Working principle

A wire scanner is an electro-mechanical device which measures the transverse beam density profile in a particle accelerator by means of a moving thin wire. As the wire passes through the beam, the interaction generates a cascade of secondary particles. These are intercepted by a scintillator, coupled with a photomultiplier, which measures the intensity of the light produced, this way the intensity of the beam in each point can be measured.

The acquisitions of the wire position and the intensity signal are synchronized with the particle revolution frequency and are combined to construct the transverse beam density profile. It is possible to have a redundancy in the measurements; while the carbon wire crosses the beam a small current is induced in it, this current is proportional to the number of particles present on the beam at the wire position. This magnitude can also be used to obtain the beam profile.

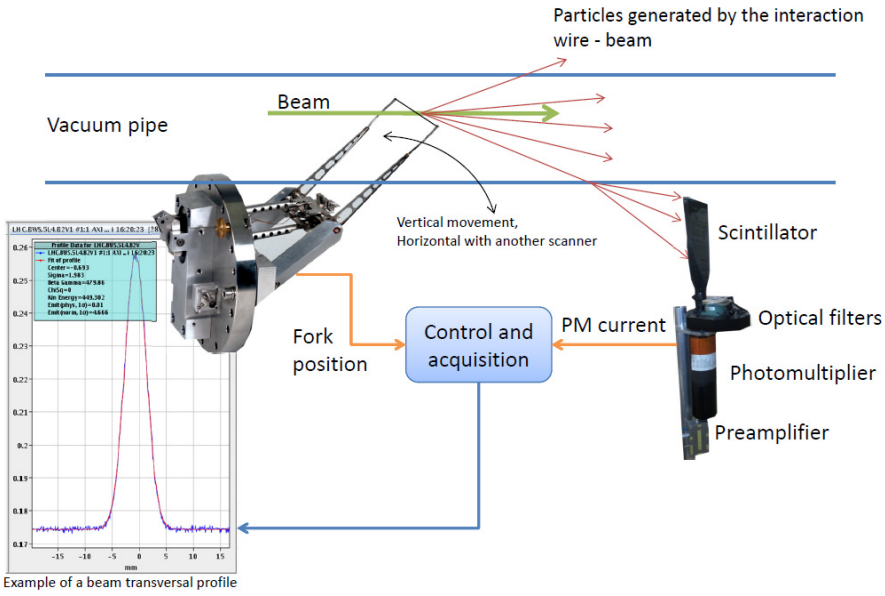

Figure 2.1: *Wire Scanner working principle*

2.1.1 Folk Mechanics

There are many kind of wire scanners installed around the world with different mechanics, but all of them have a common characteristic, there is a mechanical movement produced in the air side which should be transferred to the vacuum chamber by means of bellows. These are small mobile pieces of metal designed to transmit movements while isolating the environments (vacuum and air side), the limitations of this devices will be explained in detail later.

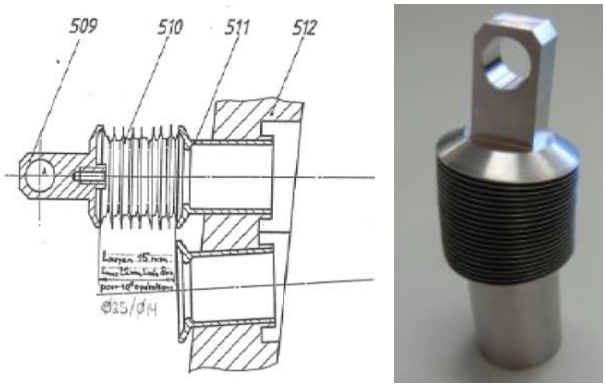

Figure 2.2: *Bellow scheme (left) and real bellow used for the Fast Wire Scanners (right)*

This option was chosen in previous designs because of the difficulties of placing motors in vacuum, to limit the possible sources of outgasing and avoid the high sensitivity to the bake out temperature that standard motors have.

According to mechanics, the wire scanner could be classified in three types [15]:

- *Linear Displacement Monitors* [16]: Used for a nominal speed of 1m/s. The linear movement is created by a standard dc motor and a rotary to linear mechanism. The position is acquired by a linear potentiometer or by an optical ruler. (See Fig 2.3 left).
- *Pendulum movement monitors* [17]: Also commonly called fast wire scanners at CERN (FWS), this design can work at speeds up to 20m/s (See Fig 2.3 right).
- *Rotating movement monitors*: Used for speeds up to 6m/s (See Fig 2.3 centre)

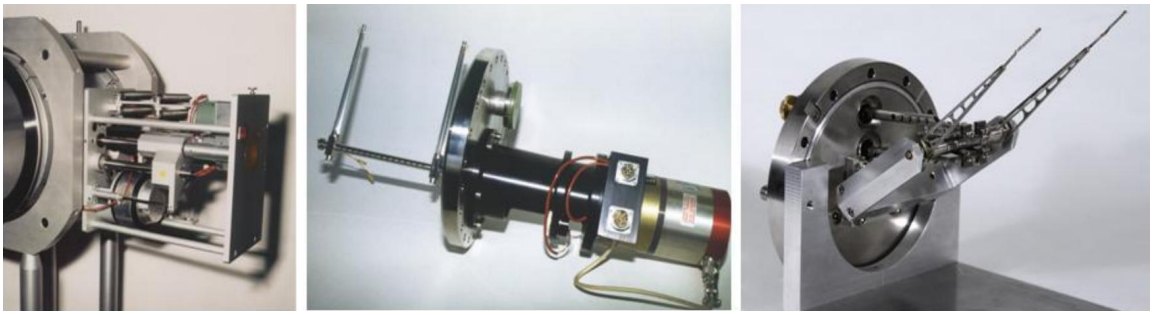

Figure 2.3: *Different devices used along the pre-accelerators at CERN.*

All this models installed already at CERN are controlled by DC motors located outside of the chamber, and by means of bellows the movement is translated from outside to inside. The speed of the wire is determined by design. The performance of the motor and the inertia of the mechanics to move the folk also play an important role in this limitation.

2.1.2 Position acquisition

The position of the folk is constantly acquired during the operation of a wire scanner by means of a linear or rotary precision potentiometer (depending of the kind of scanner); a simple voltage divider circuit is used to generate a variation of voltage proportional to the absolute position of the motor in each. The voltage variations are acquired by a 16 bit differential ADC and stored in a SRAM [18].

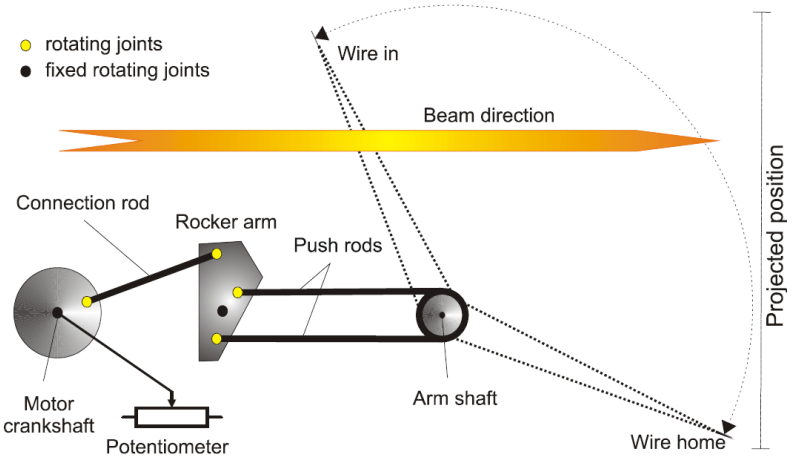

Figure 2.4: *Scheme of the working principle of a Fast Wire Scanner [19]*

In the case of the FWS, the complex mechanics and the non perfect linearity of the potentiometer force us to calibrate this type of scanner. This calibration is performed with a bench that is mounted around the scanner; the particle beam is substituted by a laser whose position is well known [19]. The laser beam is split into two parallel beams of nearly equal intensity distant by 2.7 mm by means of special optics, through which the wire travels at high speed. In the other side a large fixed mirror is positioned. The carbon wire scanning through the beams creates thus twice a shadow detected by one single photodetector, resulting in 2 negative peaks and otherwise constant signal. Correlating the measured peak positions with the real laser beam position allows the creation of a correction table.

2.1.3 Motion Control and data acquisition

All the wire scanners installed at CERN are working with the same electronics in order to control the movement of the folk in a suitable and unified way. For this, it is necessary to use several control modules. The modules are installed in VME64X rack; the different task to perform are controlled with different cards (see Fig 2.5):

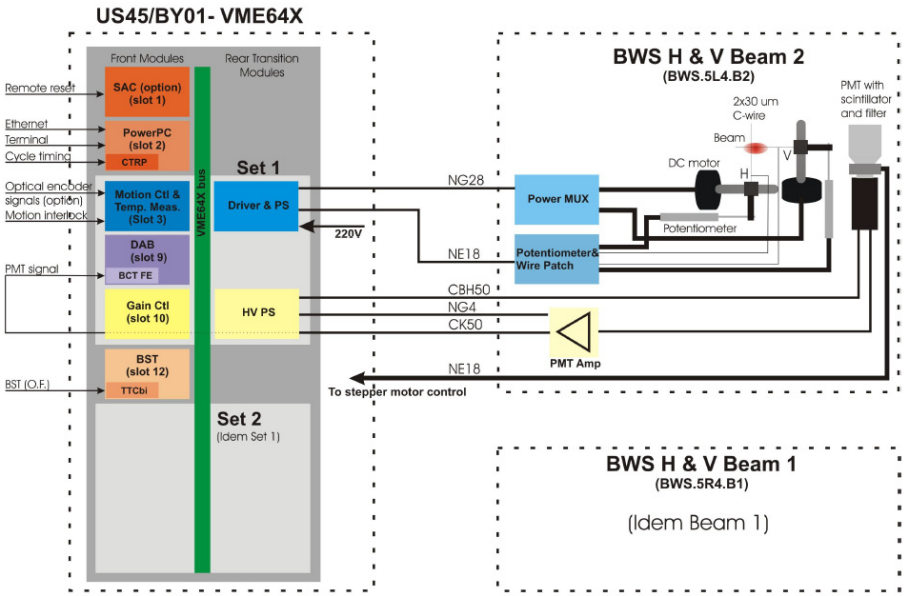

Figure 2.5: *Functional scheme of a wire scanner electronics.*

The PowerPC controller: This is the VME Master, which makes possible to access the VME-bus through the Ethernet. It runs LynxOS where a specific server is running in order to control the different electronic cards.

The WSMCC (Wire Scanner Motion Control Card): It controls the motion of the wire scanner, acquires the exact position of the wire and measures the wire temperature and resistivity. It also stores all this data in a reachable place and accessible by the VMEbus. The movement control is done by following a reference curve of speed and comparing this with the sampled position data [18].

Driver and power supply: This card is able to control 4 scanners multiplexed (one at a time). Depending of the scanner type, the speed is adapted. This driver receives the control voltage from the WSMCC and drives the wire scanner. This driver is based on linear power operational amplifiers and big capacitors to be able to provide high current peak in short time, needed for the high acceleration applied in the motors.

Beam synchronizing: Used to synchronize the wire scanner with the particle revolution frequency of the accelerator used.

High Voltage power supply: Controls the photomultiplier (PM) voltage.

Digital acquisition board: Acquires the PM current at high frequency (40MHz).

2.1.4 Scintillator

The scintillator is the device that converts the hadronic shower produced by the wire-beam interaction into light; it must be placed out of the vacuum chamber and at a certain distance and angle from the interaction point, according to where the secondary particle shower is most appropriate for detection. The scattered particles interact with a scintillating material which is able to produce photons due to this interaction. In order to amplify the optical power produced, the scintillator is directly coupled with a photomultiplier tube (PM), see Fig 2.1. The PM has two basic stages: the conversion of protons into electrons and the electron multiplication, which enhances the signal level and improve the signal over noise ratio, this simplifies the acquisition electronics.

The transverse beam density is drawn by acquiring the PM current and plotting it with the position of the folk.

2.2 Installed systems

There are different models of wire scanners already installed in each of the CERN´s accelerators, PS, PSB, SPS and of course in the LHC. All the different models installed share the same working principle (crossing the beam with a carbon wire and measuring the secondary particles with scintillators), and they are built using the same basic components, but with different designs (explained in the previous section) and adapted to the characteristics of each of the accelerators. The pictures below and the next table show some examples of installed systems.

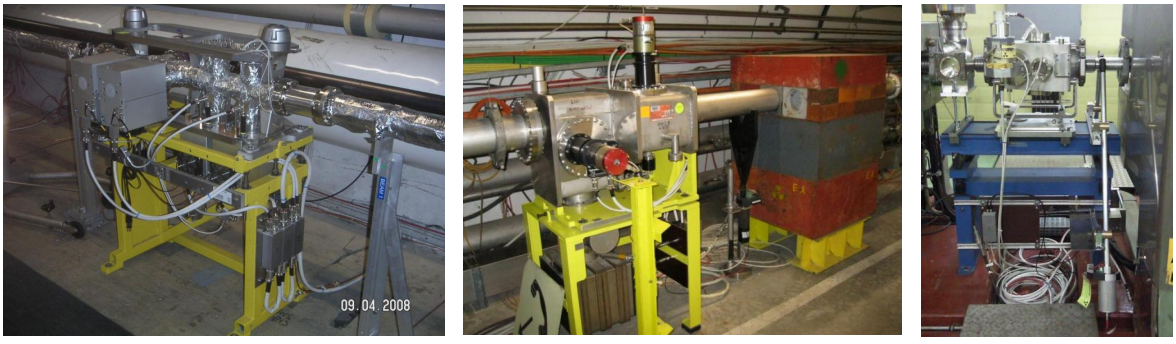

Figure 2.6: *Examples of Wire Scanners installed in LHC (left), SPS (Center, it´s clearly visible the two scanners) and PS(right)*

Machine	Scanner type	Number	Scintillators	Max. Speed (m/s)
PSB	Rotating Fast	8	1 for 2 scanners	20
SP	Rotating Fast	5	2 per scanner	15-20
SPS	Rotating	6	1 for 2 scanners	6
SPS	Linear	4	1 for 2 scanners	1
LHC	Linear	8	1 for 4 scanners	1

Table 2.1: *Wire scanners and types installed at CERN*

The CERN's wire scanners are operated on a daily basis on all circular accelerators of CERN. In order to measure the horizontal and vertical transversal profiles two WS are used at the same point, they work under the same working principle and are rotated 90^{o}.

2.3 Limitations

The actual designs of wire scanner present some limitations which will be mitigated in the new design, these limitations could be characterised in different categories.

-Breakage of the wire:

- For high intensity beams, the energy deposited by the incident particles on the wire may be sufficient to melt or sublimate the thin wire, since their speed is quite low.
- The wire can melt or sublimate also due to the energy transferred by the beam to the wire through its accompanying electromagnetic field [19].

-Accuracy:

- The designs present inaccuracy of position measurement of the wire, primarily due to vibration.
- The accuracy is also limited by the use of complex mechanics needed for high speed.

-Resolution:

- The improvements done in the accelerators and the need of high luminosity reduce the beam diameter; this means that an improvement in the measurement resolution is needed.

-Vacuum Leakage:

- The usage of bellows limits the operational life of the wire scanners, due their inherent fatigue, bellows are limited by certain number of working cycles, after this there is no warranty of good vacuum isolation. Moreover the high inertia of this component makes difficult to move the folks at 20m/s.

In order to improve the optimization of the luminosity in the Large Hadron Collider (LHC), much higher measurement accuracies than currently achievable are required. The new performance demands include a wire travelling speed up to 20 m/s and a position measurement accuracy of the order of 1 μm. All these characteristics and the hard working environment implies a design with extremely low vibration, radiation hard/tolerant in order to avoid aging, suitable for high temperature and vacuum. In the new design it is also desirable to develop a compact and modular vacuum vessel that could be easily integrated into different accelerators, this way one unique design would be suitable for all of them.

CHAPTER 3

Context and objectives of the thesis

This chapter will describe the design of a new wire scanner as well as all the environmental characteristics in which it should operate. Here it is also explained the objective of the present work and the main design criteria to follow in terms of vacuum compatibility, high temperature, and radioactive environment.

3.1. The design of the wire scanner

The baseline solution consists on a small diameter rotary brushless synchronous motor with the rotors magnetic field provided by permanent magnets, the rotor is installed inside the vacuum chamber and coupled to the stator, which is outside the chamber, through a non-magnetic permeability stainless steel wall. This way, the use of bellows can be avoided. The rotor is supported on a shaft by roller bearings with solid lubricants. Attached to the same shaft there are two arms on which the wire is stretched. A position transducer, mounted on the rotating shaft shall provide its absolute angular position for the feedback control loop of the motor. For highly repeatable relative position measurements, an optical optical sensor will provide more accurate measurements of the wire position. One of the main advantages of this design comparing to the previous ones in terms of maintenance is that the complete scanner assembly visible in Fig3.1 right can be disassembled and the whole scanner moved to the laboratory for maintenance operations, such as calibration, without removing the whole tank.

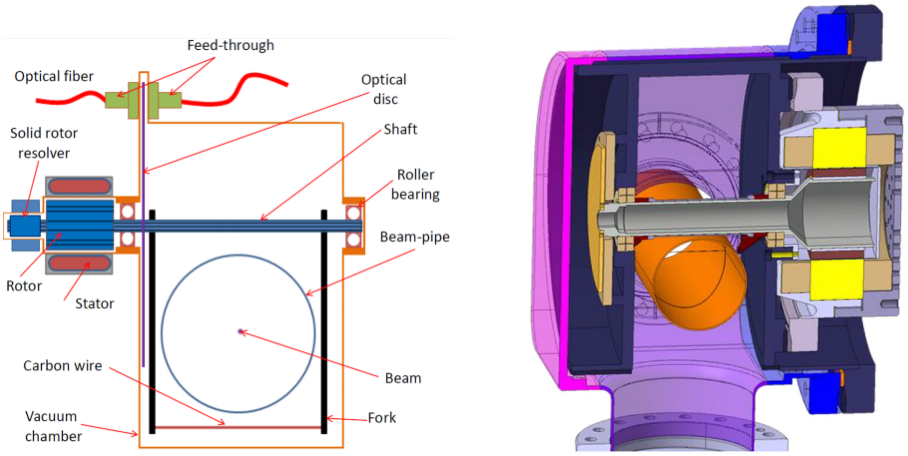

Figure 3.1: *Scheme of the wire scanner assembly (left) and CAD view of it inserted in its tank (right)*

3.1.1 Motor design

A frameless PMSM motor from Parker for the prototype of the scanner has been selected for its performance and flexibility of the ordering possibilities in terms of separated pieces, custom magnets and separated rotor. The motor itself consists mainly in two parts, a three phase stator, and a rotor with permanent magnets mounted on its surface, these two pieces are completely independent [21]. These characteristics allow a direct integration in a WS. To make the rotor vacuum compatible the fixation of the magnets in the rotor (by glue)

must be changed by a mechanic fixation, in Fig 3.2 there is a fixation possibility. The rotor consists on a piece of stainless steel and samarium cobalt as magnetic elements; these magnets were chosen by their resistance to high temperatures.

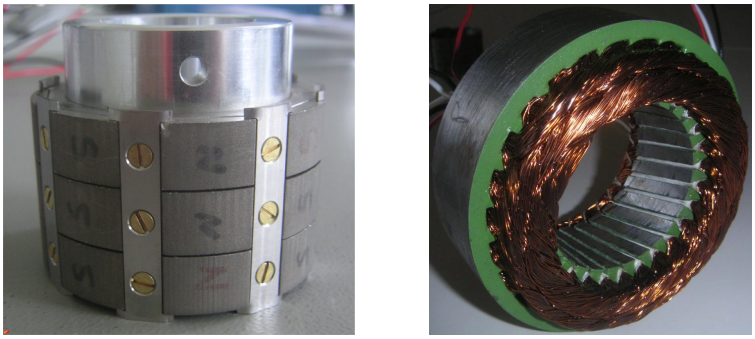

Figure 3.2*: Picture of the rotor with samarium cobalt magnets and fixation for vacuum compatibility (left) and three phase stator (right).*

Moreover the air gap between the two pieces (between 0.7 and 0.85mm) it's enough for the vacuum barrier integration.

3.1.2 Solid Rotor resolver

For the control of the motor a Rotasyn solid rotor resolver is used, as for the motor, the stator of the resolver is placed outside whereas the rotor is placed inside the vacuum chamber. The separation between them is a no magnetic permeability thin wall located in the air gap between the two pieces. There is no coil in the rotor, primary and secondary coils are on the stator. The rotor modifies the coupling efficiency of the magnetic field between the coils when it's moved. This configuration makes the component vacuum compatible, and the usage of kapton, as electrical isolation, tolerant to high temperatures. The resolver provides an accuracy of ±17mili Rad, and high reproducibility which allows digital calibration to increase the accuracy (±1.745mili Rad), see Fig 3.3, once calibrated with a high precision optical encoder (Heidenhain RON225) [23] the accuracy reached is not considered enough to identify the exact position of the folk according with the specs, however it's considered precise enough for the control loop of the motor. In order to obtain a precise measure of the position of the folk and also determine accurately the width of the beam it's necessary to use a second device much more precise.

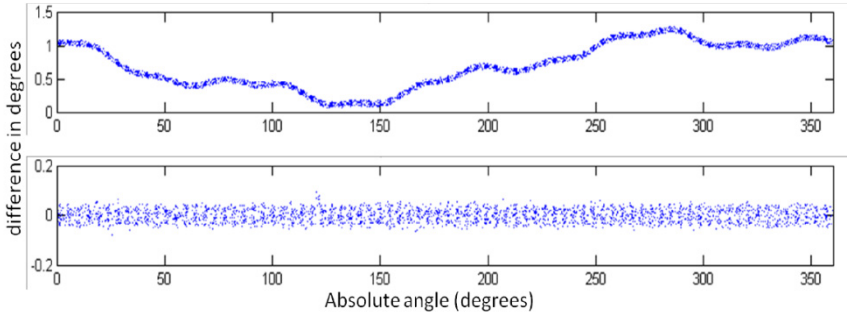

Figure 3.3: *Difference between the resolver and the encoder measurement according to the encoder angle. Before calibration (top) and after calibration (bottom) [22].*

3.2. Scope of this thesis

The main objective of this thesis is to design and implement the relative optical position sensor based on optical fibre, related to the new design of wire scanner, also taking into account the general specifications of the whole design of the Vacuum Wire Scanner (VWS from here in advanced). According to the limitations of the environment this sensor must work under very hard conditions and provide as much accuracy as possible, this means that all the components must be carefully selected and also rated to high temperature, ultra high vacuum and radiation environment to provide the longest life time as possible.

3.2.1 Base solutions to study

The initial configurations to study for the sensor part is the four proposal bellow:

Transmission: Two fibers into the vacuum chamber will be used, the fibers will be placed in front of each other, in a way that one of them sends light to a disc and the other, placed in the other side, acts as receiving fiber. While the disc rotates, the receiving fiber senses the optical power changes produced when the slits cross the space between the fibers.

Reflection: In this configuration only one fiber and a disc with reflecting slits would be used. The same fiber that emits light will be responsible to collect the reflected signal from the slit surface. In this case an optical circulator should be used outside of the chamber in order to separate the emitted and reflected light. Based on this approach, 3 configurations have been studied.

F**iber and disc**: The fiber will be placed in front of the disc without optical interfaces.

Focuser in the vacuum chamber: A focuser could be used at the end of the fiber and placed into the vacuum to improve the coupling efficiency of the reflected light. With this solution, it is possible to use a magnification factor in the lens system in order to obtain a spot size smaller than the core of the fiber. It will be very important to find suitable glasses and assemblies in order to be able to work in Ultra High Vacuum and High Temperature.

Focuser outside of the vacuum chamber: In this configuration an optical viewport for vacuum should be used and a system of lenses must be designed to obtain long focal distances to focus the light from the fiber outside the vacuum chamber to the disc inside the vacuum.

All this configurations should be studied in terms of tolerance, coupling efficiency and material availability. The final aim will be to design the most adapted system as possible to comply with the specifications of the following section.

3.3. Characteristics and specifications.

3.3.1 General

As there will be no moving parts outside the vacuum chamber, the transducer must be partly or entirely installed inside the ultra-high vacuum environment.

The shaft will have a reciprocating movement of 180º, which comprises three phases divided in equal parts, acceleration over 1/3 (60º) up to a peak velocity of 200 rad/s (for a folk length of 100mm), constant scanning velocity over 60º and deceleration to stop over the remaining 60º stroke.

3.3.2 Accuracy requirements

The transducer must provide the angular position of the shaft for two independent functions, with different requirements in terms of accuracy. The first consists on the absolute position readout needed for the

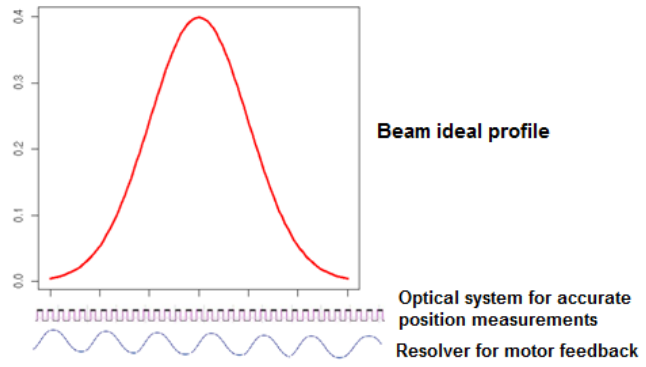

Figure 3.4: *Sensor accuracy comparison approximation while constant speed phase*

motor control, which implies an online measurement throughout the full stroke but with relatively low accuracy as per current technology standards. The second function of the position measurement is directly related to the overall performance of the wire scanner system, as it is required to obtain a very accurate position determination of the wire as it crosses the particle beam. The requirements for each of these functions are listed hereafter.

3.3.2.1 Accurate wire position measurement for beam size determination

The required angular resolution to reach is 500 μRad with an accuracy of 25 μRads during the scanning part of the stroke (constant speed phase). For this, higher linearity errors are acceptable if the system has good repeatability and calibration is possible and performed. The signal processing may be performed offline if accurate timing of data recording can be implemented. The dynamic parameters of the movement are as follows:

- Relative position measurement over a stroke of ±60º.
- Angular velocity up to 200 radians.s-1.
- Negligible torque from the motor, therefore nearly constant velocity.

3.3.3 Materials and vacuum compatibility

The surfaces of the transducer exposed to vacuum shall have, after bakeout, a total outgassing not exceeding 10-9 Pa.m3.s-1. Outgassing of hydrocarbons shall not be measurable using the state of the art residual gas mass spectrometers. Preferred materials are stainless steel, copper, aluminium and ceramics. The usage of other materials is subjected to approval by CERN. Polyimide may be acceptable as a conductor insulator if its usage does not compromise the total outgassing specification. The leak rate across any barriers between atmosphere and vacuum shall not exceed 2x10-11 Pa.m3.s-1.

3.3.4 Temperature

The transducer will operate at room temperature; however, every exposure of the vacuum chamber to atmosphere requires a subsequent vacuum conditioning comprising a thermal cycling at high temperature. All parts of the transducer installed in the vacuum chamber or in contact with it shall withstand thermal cycles at 200º C during 24 hours. The transducer is not expected to operate during the high temperature cycles.

3.3.5 Radiation

All components to be installed nearby the point where the measurement is taken must be resistant to a cumulated ionizing radiation dose of 20 kGy (roughly 1 kGy/year). Non radiation hard electronics must be installed in shielded galleries away from the particle beam, which implies cables up to 250 m long.

3.3.6 Assembly and integration

The assembly procedures must follow the best practices applicable to ultra-high vacuum systems, such as to prevent leaks, virtual leaks and outgassing. The sensor construction must allow the chemical cleaning of all surfaces exposed to vacuum by immersion in a degreasing bath with ultrasonic agitation.

The scanner must fulfil the required performance with the previously enumerated limitations such as the long cablings between the instrument and its control and measurement electronics.

3.4 System analysis

Due to the main considerations of the project specifications, it is not possible to place electronics near the radioactive area. Other consideration as EM interference and the hardness of the environmental conditions have to be taken into account. Based on this constrains the sensor should be to work under hard environments, the light emiting source, the receiver, and the subsequent electronics should be placed at least 250m far from the sensitive device. One technical solution is to use **optical fibers** to transport the light signals through the space. Moreover, taking into account that the disc will be placed inside vacuum, the light must be transported from air to vacuum conditions, this implies the use of **optical feedthroughs or Vacuum Viewports** (see Fig 3.5 for an schematic of the system).

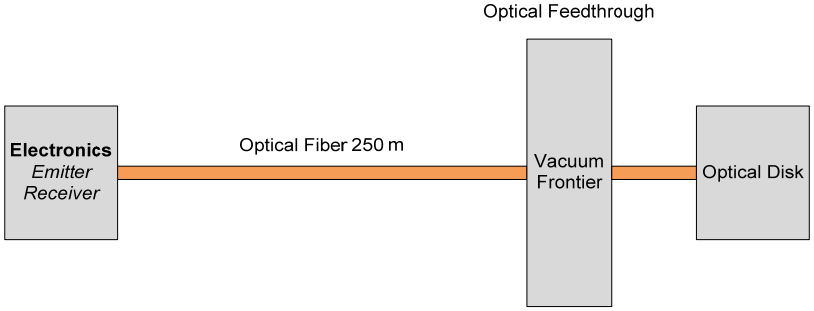

Figure 3.5: *Simplified general system scheme*

One important consideration is to expose **as fewer components** as possible to the Ultra High Vacuum (UHV), radiation, and high temperature. This will reduce the sources of error, making the sensor more reliable, as well as avoid possible vacuum leakages. By reducing the components the maintaining operations may be easier.

The components selection has to take into account the environmental conditions and specially the radiation. It is assumed that the radioactive environment will reduce the life time of the components, modifying their molecular/physical structure and losing this way their initial properties, for this it will be important to select components radiation tolerant/resistant.

All this considerations have driven the selection of the rotating encoder method using optical fiber to detect light variations by a disc installed directly in the vacuum tube. The system should be **optimized in terms of light losses**, scaled with a big margin of optical power in order to overcome the possible and inevitable aging of the components and have a comfortable power margin.

CHAPTER 4

Theoretical concepts

This chapter will include the basic working principles of the commercial optical position sensors available in the market. Several kinds of encoders will be presented in detail as well as the most typical methods to increase their accuracy

4.1 The optical encoder

Very often, it is required to detect the position, velocity, acceleration and direction of movement of rotors, shafts, pistons or the actuating devices such as a rotary machines and translational systems. This can be achieved by the use of optical encoders. The optical encoder is a device, which provides pulsed signals in response to the movement. Continuous optical signals are modulated (coded) by the use of a rotating disc with code patterns called “tracks”. The pattern on the disc consists on alternate appearance of opaque and transparent segment. There are two types of optical encoders, such as incremental encoders and absolute encoders.

4.1.1 Incremental optical encoder

The Fig4.1 illustrates the schematic diagram of an incremental encoder. The central element in the encoder is the circular disc that contains the alternative evenly spaced opaque and transparent segments over a circle. A light source is located on one side of the disc and a photodetecting device (photodetector) is placed on the other side of the disc. Light Emitting Diode (LED) are used as light source providing continuous light power. A photodiode is commonly used as the light detector, which is placed at the other side of the disc. The light source and detector are faced each other. With this configuration as the disc rotates, the photodetector receives pulsed light signal every time it “sees” the light through a slit.

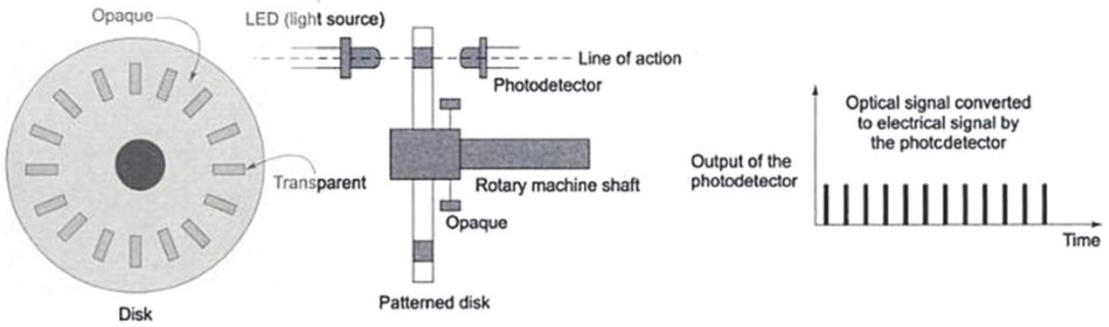

Figure 4.1: Incremental o*ptical encoder example [41]*.

The disc is rigidly fixed on the rotor or shaft of the rotating element. And information such as the position is extracted from the number of pulses after certain reference, whereas the number of pulses per second measures the velocity of the disc. In order to obtain the

position rotary incremental encoders use electronic counts to calculate to count the angular increments.

According to [41] a common way to build encoders uses two channels, later called ChA and ChB, plus an absolute reference mark which marks the beginning of each turn. The channels A and B are separated as shown as in Fig4.2 (ChA, the two left photodetectors and ChB, the two right photodetectors), physically spaced 90 degrees electrical or one quarter or a cycle. This configuration is also known with the name of "quadrature encoder" where rotating direction can be known by detecting the phase relationship between channels (if the Channel-A leads Channel-B, then the direction of movement is clockwise direction, and vice versa). In order to avoid imperfections on the discs such as scratches in the glass or not perfect slits, the receiver uses the information of several slits in parallel by means of using a fixed pattern (that has the same grating as the disk) in front of the light source. When the disk turns, the light is shuttered in the receiver plane, receiving the optical power average from multiple slits once the disk is in phase with the window. In order to obtain an absolute position, a counter is used. This counter is initialised each time the index channel is detected. The only problem with these encoders is the lack of initial absolute information when the system is powered up.

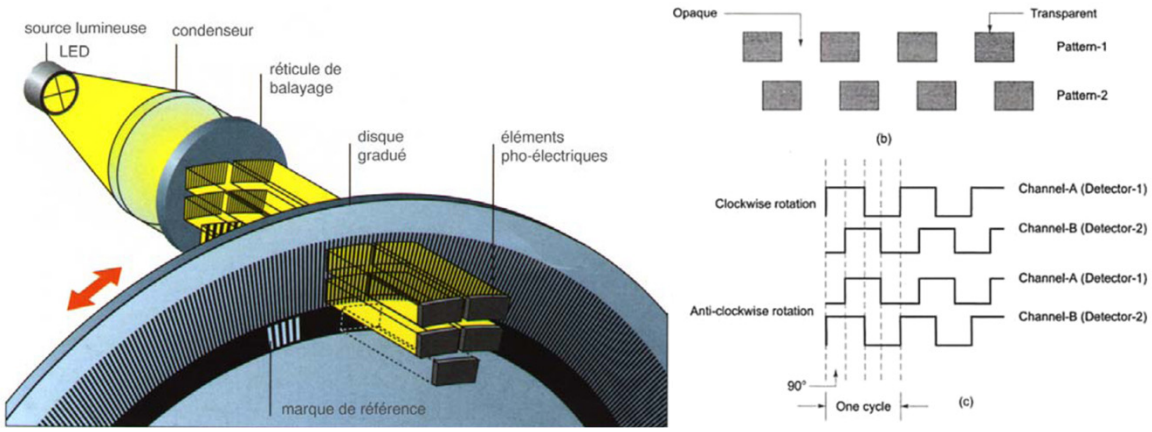

Figure 4.2: *Quadrature incremental optical encoder with two patterns. (b) Relative angular placements of two patterns. (c) The quadrature output of the two photodetectors.*

4.1.1.1 Techniques applied to increase the resolution of incremental encoders

a) Electronic multiplication

The resolution of a digital-output incremental encoder can be increased by electronic multiplication of the channels. By considering the positive edge of the channel A only, the resolution is the same as the line pair count of the disc. If both positive and negative edges are used, twice the count/revolution of the disc is achieved. By adding the edges of the channel B, the resolution becomes four times the line count of the disc. Some care must be taken with the four times resolution: if the quadrature phase shift is not close to 90° (electrical), the positions will not be evenly divided and accuracy will suffer. Commercial IC's are available to perform the x4 multiplication function and extraction of the direction information.

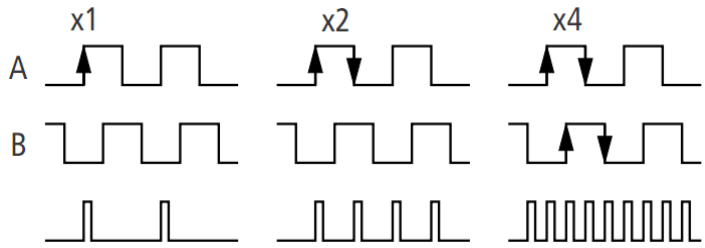

Figure 4.3: *Electronic multiplication example*

In most encoder circuits, a hysteresis comparator and digital filters are used to process the analog signals coming from the sensor and filter out the noise, while quadrature decoding is used to obtain the count pulses. The Fig. 4.3 shows the sine cosine waveform outputs of an optical encoder after the hysteresis comparator circuit, and the output up/down count pulse. The resolution of the up/down count pulse is 4 times the optical encoder's resolution.

Quadrature decoding is the most common method to decode the phase A-B signals into up/down count pulses. This has the advantages of simplicity and full digital implementation. However, the count pulse resolution is limited to four times its optical resolution.

b) Sine-Cosine Interpolation

To increase the resolution of optical encoders more than fourfold, a form of sine-cosine interpolation method has to be used. As in the previous case; the signals should be

carefully displaced 90 degrees electrical, but instead of cutting the original signals and obtaining square waveform, the full information of the waveforms is used. Through this interpolation method, intermediate values of sine cosine waveforms can be found, and, through the detection of these intermediate values, much higher resolution of count pulses output can be achieved, Figure 4.4 shows a typical 16 fold interpolation.

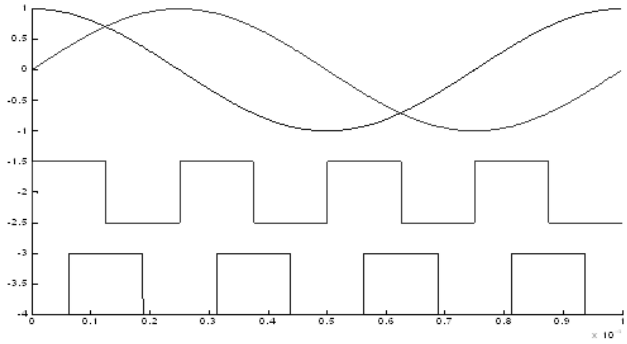

Figure 4.4: Ideal 16 fold sine-cosine interpolation [39]

Presently, there are basically 2 commonly used methods to increase the resolution of optical encoders in this context:

1. Use a resistor network to detect the magnitudes of the sine cosine waveforms.
2. Use ADC converters to acquire the current magnitudes of the sine/cosine waveforms.

Method 1: Use a resistor network to find the intermediate positions

The first method is to use analogue comparators to obtain the angle of the magnitude of the phase A and B signals. Since the output of the two signals from the optical encoder has a sine-cosine relation, there is a one-to-one mapping of these signals to the intermediate position values of the optical encoder.

Essentially, the translation of the output signal is a circle, when they are plotted on a 2D plane.

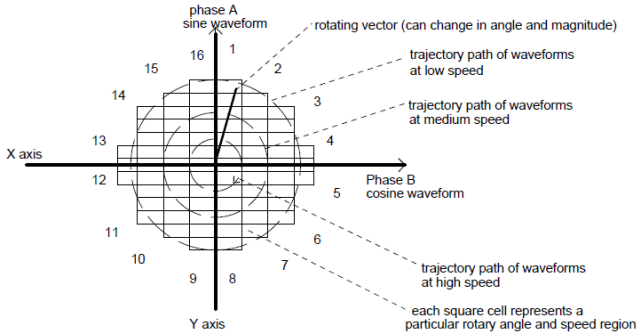

Figure 4.5: *Mapping the rotating angle, bounded* regions [38]

However, the magnitude of the signals decrease as the speed of the optical encoder is increased.

For high performance motion systems, it is necessary to track the values on the whole 2D circular plane (see Figure 4.5). A 2D lookup table based on a large resistor network and analogue comparators is needed. This method has the advantage of employing straightforward circuit, with no software programming. However it presents several disadvantages:

1. Difficulties to construct a precise resistor network
2. A large number of comparators are needed.
3. Resolution decreases at high speeds

Method 2: Use a two channel data acquisition circuit

This is the most common interpolation method used in motion control systems. Rather than building a large resistor network with a large number of comparators, the interpolation process can be implemented by a high speed data acquisition circuit, using DSP or FPGAs. Such an approach has the advantages of high flexibility and large resolution increase. In some cases, resolution increase of up to **×1024** can be achieved.

The higher the resolution, the higher will be the pulse output rate, and the higher will be the computing requirement. Under this configuration, it is very expensive to implement a high speed and high-resolution interpolation decoder.

To overcome this problem, many systems are using variable resolution scheme. When the disc speed is too fast for the computing unit to handle, its resolution decreases to reduce the computing requirements.

4.2 Error sources in incremental encoders and calibration methods

Ideally in the encoders, the sampling events are evenly spaced around the circular scale with certain nominal spacing of $\Delta_0 = 1/N$, were N is the number of spatial events in one revolution. The rotational angle is found by counting the number of spatial events read by the scanning unit $\theta_k = k\Delta_0$.

This ideal case assumes a perfect mechanical mounting where the centre of the scale is aligned with the rotational centre of the shaft, so no radial error is considered. This case

also assumes a perfect equal spacing between marks in the disc. Each spatial event is then treated by the scanning unit as an equal increment in rotational angular position. This ideal case has no angle errors, but is not realistic (see Fig 4.6a).

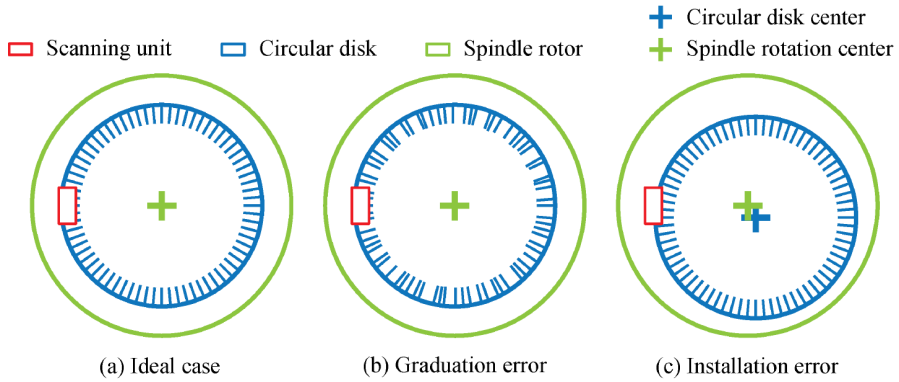

Figure 4.6: *Sources of error in the encoder's accuracy [24].*

In general the circular scale will be always mounted with some eccentricity with respect to the shaft rotational centre (see Fig 4.6c), this imperfect mounting of the scale, or offset of its centre, is read by the scanning unit as slow speed changes among a full rotation of the disc, which leads to repeatable angular errors. The scanning unit is more sensitive to this error when the mounting offset is parallel to the scanning direction. In this error configuration, a change in speed is detected (see Fig 4.7a). However when the eccentricity moves the disk closer (Fig 4.7b) or far away from it, there is no considerable error noticed by the sensor. This mounting error dominates over other errors in the system and can be modelled as shown in the equation of the Fig 4.7. Where D is the disk diameter, e the mounting offset and θ_e the error in angular position (given in radians). Even with a highly precise mounting alignment as low as 0.5um of eccentricity with a 200mm disk, the contribution of this error is in the order of 2.86e-4 (1 arc-sec), which is comparable to the accuracy we are seeking.

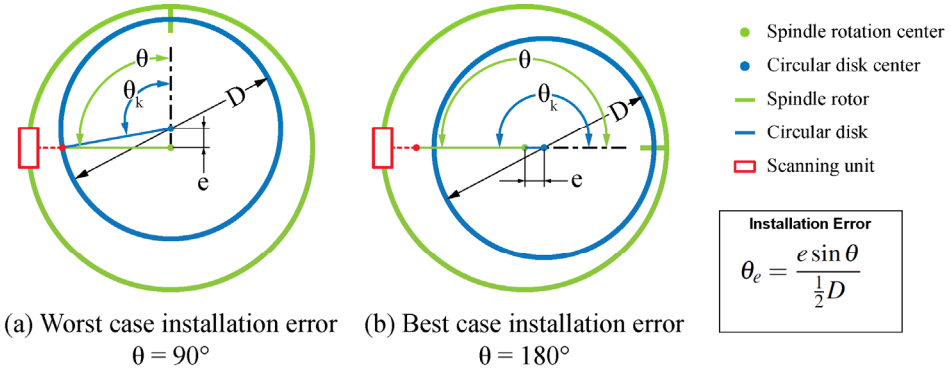

Figure 4.7: *Eccentricity error due to disc mounting [24].*

Another source of uncertainty is that the manufacturer of the encoder disc cannot guarantee perfectly even spaced marks. There are certain tolerances in the order of few microns, which results of repeatable errors in the rotational position measurement.

The last repeatable error source is due to spindle radial error motion, since the spindle axis does not rotate perfectly and during rotation the axis will move radically. This external error could be seen as an error similar to the mounting error, but in general this it is quite small and not the dominant error source of the systems, the providers give quite small tolerances in the components related (in the order of few dozens of nanometers).

In general the measurement error of an encoder system is not only a property of the disc itself but also a combination of the system where it is installed. Graduation, installation and spindle motion error exist in all incremental angle encoder and limit the measurement accuracy that can be achieved, the state of the art in this context is +- 1 arc-sec (2.7e-4^{o}).

In order to avoid repeatable angle measurement errors and obtain a precise rotational angular position, encoder calibration must be performed. The objective of applying a calibration algorithm is to find the encoder map, where it's included as much information as possible about the repeatable error sources. This map will be used after to correct the position measurements obtained by the encoder. According to the literature two main categories of calibration algorithms could be applied, angle comparator calibration and on-axis self-calibration.

Angle Comparator Calibration:

This method is widely used by encoder companies to extract the encoder maps of their products and characterize them in terms of accuracy. An angle comparator consists basically in multiple rotary encoders coaxially mounted on two rotary axes. This device is an angle metrology system specifically designed for angle encoder measurement errors. They have shown very good calibration repeatability, but this method is not applied directly in the working axis. The incorporation of an angle comparator on would be counterproductive, this means that after the calibration, the errors contribution of the encoder working axis are not considered.

On-axis Self-Calibration:

Calibrating the device in the working axis offers better results, since the identification of the complete repeatability errors is done. There are several possible strategies that can be applied in this context; we'll highlight some of the most promising for the project.

a) **Based on the Equal Division Averaged method (EDA)**: In this method several reading units equally spaced must be used (5 such as explained in [26]). The time that each grating line passes each scanning unit is measured and using the combined measurements, it is possible to compensate the graduation error and the disc eccentricity as well.

b) **Constant speed calibration**: This dynamic method is first presented in [25], it samples the time intervals between successive grating lines passing the scanning unit (T_k). The spatial distance between each grating line, A_k, is found assuming the angular velocity of the shaft constant during the entire revolution. By this way, it's possible to build the encoder map. However, non uniformities due to damping and rotary disturbance due to interaction between rotor and stator are not taken into account.

c) **Free Response modelling**: Another method is presented in [24, 27], based on modeling and mathematical analysis. This method involves a procedure where the encoder is spinning at constant speed and the power is stopped to let the system decelerating by itself while the encoder position is recorded. If a precise model of the system is built and the parameters are known, the expected angular curve can be obtained. By comparing it to the measurement taken, a calibration map can be extracted.

4.1.2 Absolute Optical Encoder

Absolute rotary optical encoder also provides angular position and velocity value. By use of coded disc, but under a different scheme than the incremental ones. The principle of operation is that they provide a unique output for every position. The coded disc consists of a number of concentric patterns of opaque and transparent segments. Fig 4.8 shows a typical disc of an absolute encoder having only four tracks. However, typical encoders have usually 8 to 14 tracks. The number of tracks determines the resolution of the encoder. Each track has its own photodetector. Notice the length of the transparent segments of each

track on the Fig 4.8. The length of the transparent segments of the track towards the centre of the disc increases in a specific order to satisfy the binary coding technique. This encoder can detect 16 positions (4 bits) for a single turn. If the number or tracks are 12, then the encoder will be able to detect 4096 positions for the same rotation.

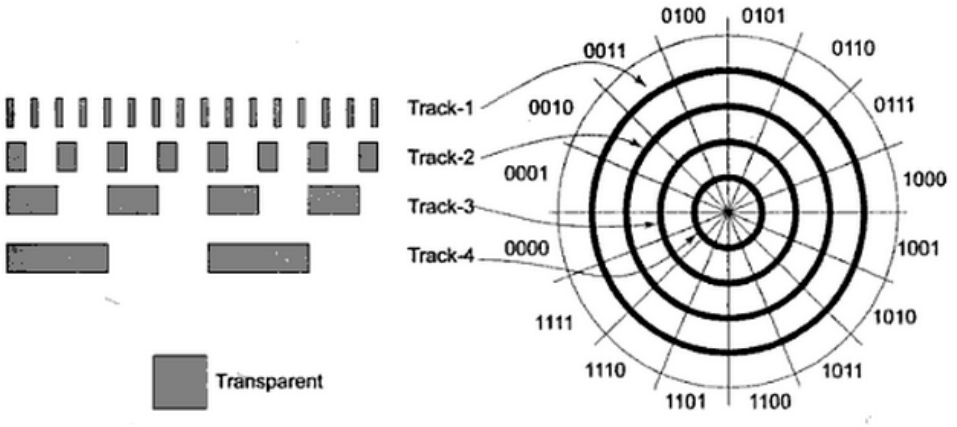

Figure 4.8: *A binary conformant coded disc for an absolute encoder [41].*

In the practice, binary patterned coding techniques are usually not employed. The most preferred coding technique used in absolute encoder is the "Gray" encoding as it has the ability or error detection and are reliable.

As a hint, note the difference between the binary code and gray code bit patterns of their corresponding decimal number presented in the Figure 4.9. When Gray code is used, only one bit change occurs while moving to the next number. This particular characteristic is not found in the binary codes and helps to identify possible errors in position. The transparent segments of the tracks are thus tray code conformant. An important advantage of the absolute encoder is the fail safe behaviour in case of power cut, since no memory is needed to have the absolute position.

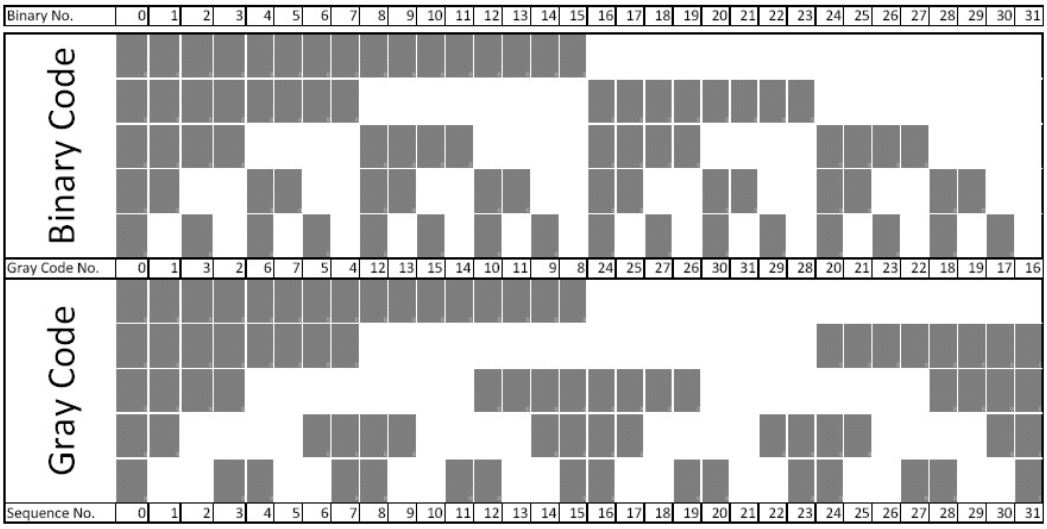

Figure 4.9: *Comparison between Gray coding and Binary coding [41]*

4.4 Principles of optical fiber

One of the main points of the project resides in the optimization of the coupling efficiency between fibers. In this context, it is important to understand, simulate and experimentally validate the equations of the coupling efficiency in the two main kinds of optical fibers, Multi-mode (by using the common rays optics approximation) as well as Single-mode (by using the Gaussian optics approach).

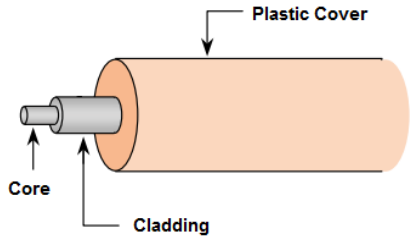

Figure 4.10: *Fiber optic architecture*

Basically a fiber optic consists on a core of silica with some dopants such as Germanium, or Fluodine (in the order or tens of microns), surrounded by a cladding (normally of 125um), and a plastic cover in order to protect the cladding and the core from curvatures, tensions or environmental conditions as shown in Fig.4.10 .

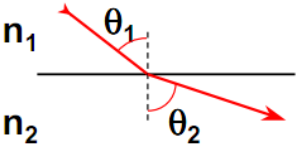

$n_1 \sin\theta_1 = n_2 \sin\theta_2$

Figure 4.11: *Snell law*

4.4.1 Fiber Optic light propagation

The light propagation in a fiber optic could be practically explained by using the Snell law: "Given two environments with different refraction index, the deviation of the refracted light will depend of the angular incidence and the relationship of the refraction indexes."

As it could be seen in the Fig 4.11, $n_2 < n_1$, n2 is smaller than n1 induce that the velocity is higher in the second medium ($v_2 > v_1$), the angle of refraction θ_2 is then bigger than the angle of incidence θ_1; that is, the ray in the lower-index medium is closer to the normal. In case of having an incident angle $\theta_1 >$ arcsin(n2/n1) is considered total reflection. This is the main definition of the numerical aperture of an optical fiber (N.A. cone of light acceptance), explained in the following figure (Fig. 4.12).

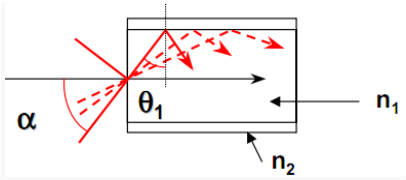

$$NA = \sin(\alpha_{max}) = n_1 \sin\left(\frac{\pi}{2} - \theta_{1max}\right) = \sqrt{(n_1{}^2 - n_1{}^2)}$$

Figure 4.12: *Fiber optics light propagation principle and numerical aperture definition*

To consider a source as perfectly coupled into an optical fiber, the light of the source should be inside the acceptance cone formed by the numerical aperture of the fiber. Other effects such as light attenuation in the optical fiber must be taken into account in order to select a suitable wavelength. The main sources of losses in the optical fiber are due to:

UV attenuation: Produced by electronic transitions between the valence and conduction band of the material of the fiber. This generates resonances out of the communication bands but it´s tails are inside of it.

IR attenuation: Produced by the existence in the far infrared of very intense abortion bands, composed by vibrations and oscillations of the structural units which forms the material of the fiber.

Rayleigh: Produced by the existence of local fluctuations and imperfections smaller than the wavelength in the refraction index of the fiber core.

OH absorption: The OH radical presents an absorption resonance in the band located between 2.7 and 4um, giving as a result harmonics in 1.38, 0.95 and 0.72 um.

This sources of losses, once combined in the chart of figure 4.13 (dB of losses per Km Vs Wavelength), is known as the attenuation chart of an optical fiber. This chart explains the three typical transmission windows used for telecommunications, which are centered at 850nm, 1310nm and 1550nm, where most of the optical components are available on the market.

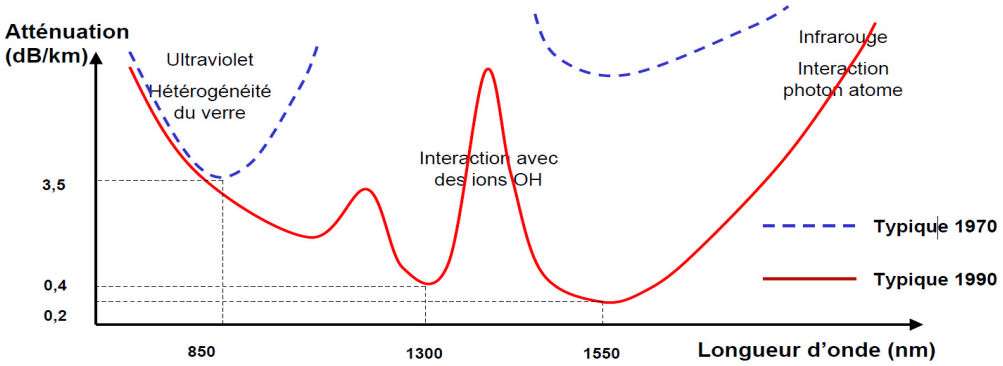

Figure 4.13: *Attenuation chart of an optical fiber.*

4.4.2 Multimode fiber

In general multimode fibers are characterised by the size of its silica core, which is available from 50um to hundreds of um. In order to transmit light, multimode fibers use step index or graded index configuration. By using step index profile the light is transmitted by consecutive reflections, whereas in the case of gradual index, the light is curved softly since the refraction index of the core changes with the radius.

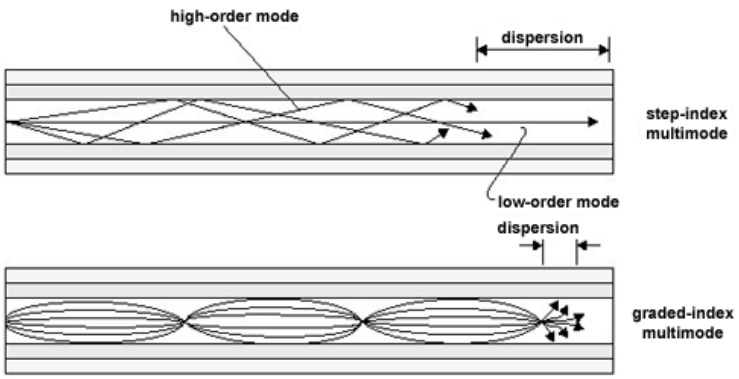

Figure 4.14: *Step-Index MMF and Graded-Index MMF*

One of the main problems that multimode fibers present is the pulse dispersion (Intermodal dispersion) in high speed communications. If we define modes as the different paths that light could take inside the fiber, the path length difference between modes could be big enough to change the shape of the pulse, this effect can be minimized by using graded-index MMF (See Fig 4.14).

In order to simplify the understanding of the Multimode fiber, we will introduce the concept of normalized frequency or V number. This parameter is defined by the diameter of the core, the refraction index and the wavelength used. With this parameter it´s possible to determine the number of modes transmitted on the fiber at a given wavelength, the mode cut off conditions, and propagation constants. For example, the number of guided modes in a step index multimode fiber is given by $V^2/2$, and a step index fiber becomes single-mode for a given wavelength when V<2.405.

$$V=2\pi \cdot NA \cdot a/\lambda \qquad (Ec.4.1)$$

Mathematically, the value of V is defined as in the ecuation 4.1 where "a" is the fiber core radius. The propagation constant of the first modes that could be excited in an optical fiber are shown in the figure bellow (Fig. 4.15), it is possible to check two regions, monomode and multimode, the light footprint of the two first modes are also shown (LP01 and LP11). Another effect that can also be applied for the single mode fiber is that for higher values of v, the mode (light path) is more confined into the core of the fiber.

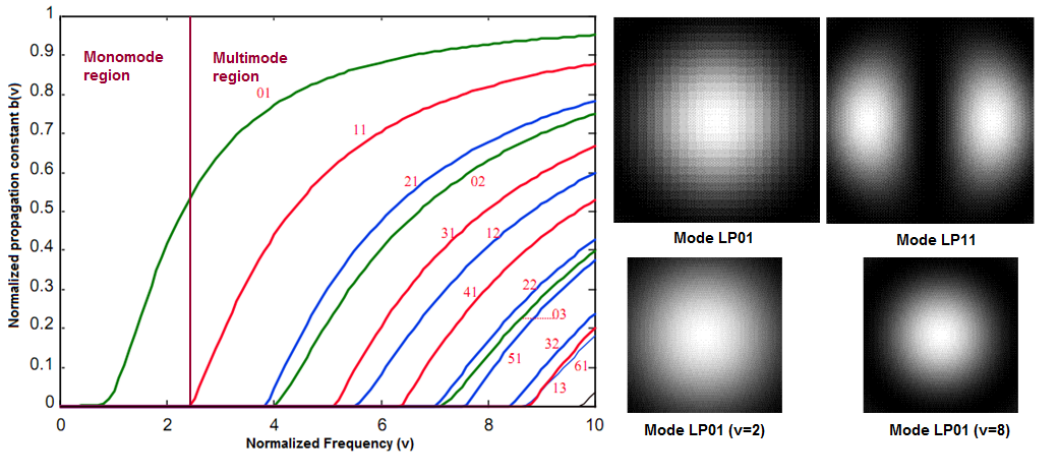

Figure 4.15*: V-B Curves (left) and light modes in a fiber (rithg)*

In order to have a good coupling efficiency a precise positioning of the fiber to center the core is required. For multimode fibers, with their large cores, fiber positioners can achieve good coupling efficiency.

The characteristics of the focused beam must match the fiber parameters for good coupling efficiency. For multimode fibers is enough in general to have a focused spot comparable to the core size, and the angle should not exceed the arcsine of the NA of the fiber (e.g. 23º for0.2NA)

4.4.3 Single mode fiber

The core of the single mode fibers is in the order of 8.3 to 10 um, this small core diameter makes them suitable to transmit only one mode, obviously this core size will depend of the wavelength of the light transported for which they are designed. Since the condition for single mode behaviour is that the V number should be bellow 2.405. In general, this fibers are used in the telecommunication industry to work in the IR range (1310nm & 1550nm), but there are models designed to work in 850nm and lower. In the single mode approach it is considered that there is only one ray of light being propagated inside the fiber, just in the centre of the core, so, there is no intermodal or intramodal dispersion. These characteristics makes them suitable for long and high bandwidth fiber communications.

Companies are usually providing the V number of their fibers, the working wavelength and the mode field diameter (MFD) of the light inside the fiber, which could be bigger than the silica core. This data is provided for easier matching of lens to optical fiber for a Gaussian beam.

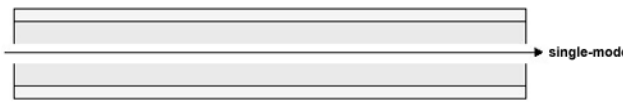

Figure 4.16: *Single mode fiber scheme*

Single-mode fibers are requiring more elaborate couplers with submicron positioning resolution. To maximize coupling into a single-mode fiber, it is necessary to match the incident field distribution to that of the fiber mode. For this, Gaussian optics should be used. For example, the mode profile of the HE_{11} mode of a step index fiber can be approximated by a Gaussian distribution with a 1/e width w given by:

$$w = d\left(0.65 + \frac{1.619}{V^{1.5}} + \frac{2.879}{V^{6}}\right) \qquad \textit{(Ec.4.2)}$$

Where:

d is the core diameter, and V is the "V-number."

For a F-SV fiber, which V = 2, the Gaussian width is approximately 28% larger than the core diameter, so the light should be focused to a spot size 1.28 times the core diameter at the fiber surface.

4.4.4 Sources of loses in fiber coupling

The main sources of loses in fiber optic light coupling comes from displacements, misalignments or tilted fibers. In order to quantify these sources of loses a tolerance analysis will be conducted during this project. Due to the environment in which the sensor will be placed and the vibrations associated to the scans this could be a major task in this work. The following sources of loses will be studied in the project and verified with practical data in order to select the best solution for the optical position sensor. The following cases uses the analytical equations are considers a wavelength of 1310nm and a mode field radius of wo=4.65um

Lateral Misalignment:

Lateral misalignment is an offset of the two fibers as shown in the Fig 4.17. It is described as a radial offset of the fiber core.

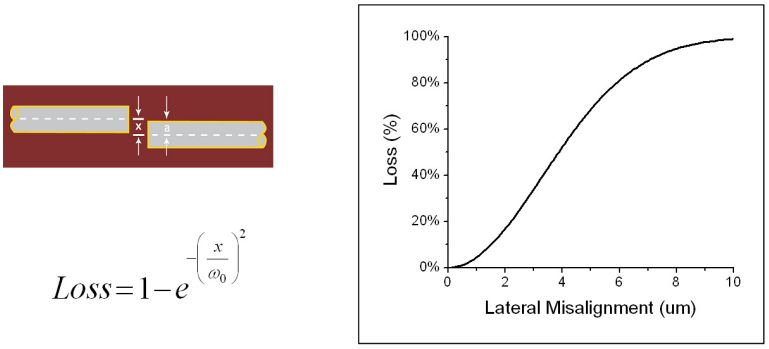

Figure 4.17: *Lateral misalignment (drawing, analytic equation and chart)[43]*

The percentage of loss due to a lateral misalignment is as in the equation of the Fig 4.17. Where ω_0 is the mode field radius ($1/e^2$). It could be seen that x/ω_0 is the ratio of the offset to the mode field radius. The chart shows the loss for a wavelength of 1.3um with a mode field radius of 4.65um. The fiber coupling is very sensitive to lateral misalignments. For example, when two single mode fibers are displaced by only 1um the loss is 4.2%.

Angular Misalignment:

The loss due to an angular misalignment of the fiber has a very similar functional form to the lateral misalignment.

In the equation of Fig 4.18, ω_0 is the mode field radius ($1/e^2$), λ is the wavelength, n_0 is the index of the material outside the fiber. It is again of the functional form $e^{-\theta^2}$. This can be seen by emphasing that there are a few constants out in front of a sin(θ) term. For small

angles sin(θ) is approximately θ. The coupling is very sensitive to an angular misalignment. The loss is about 4% for 1 degree of angular misalignment.

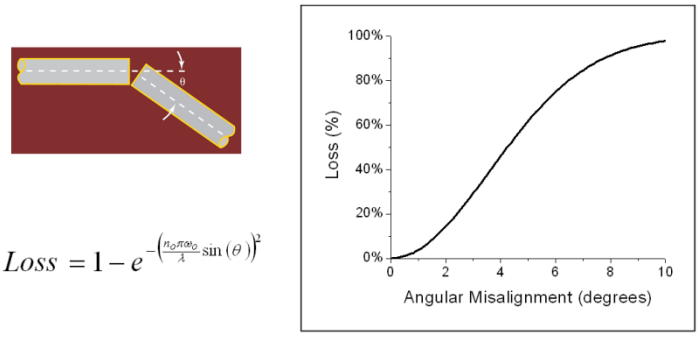

Figure 4.18: *Angular misalignment (drawing, analytic equation and chart) [43].*

Longitudinal displacement:

This is one of the most common and sensitive source of loses. The loss due to this displacement is given by the equations of Fig 4.19. Where ω_0 is the mode field radius ($1/e^2$), λ is the wavelength; n_0 is the index of the material outside the fiber. A 20 um displacement will cause a loss of about 3%.

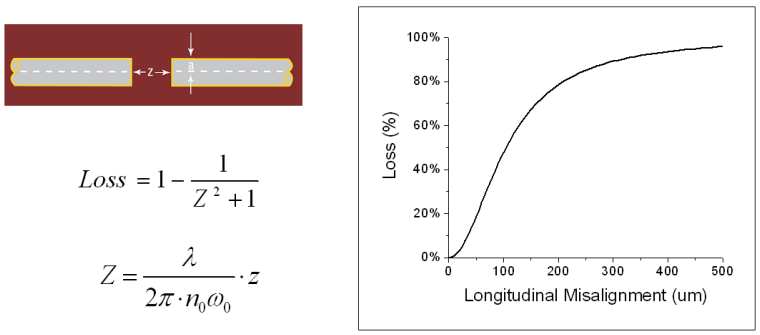

Figure 4.19*: Longitudinal displacement (drawing, analytic equation and chart) [43]*

Mode field diameter mismatch:

Another consideration for the coupling of two single mode fibers is the loss that occurs when two fiber cores have different sizes. There will be a different mode field diameter in the two fibers leading to a coupling loss.

The coupling loss is explained in the equation of the Fig 4.20, where ω_1 is the mode field diameter of one of the fibers and ω_2 is the mode field diameter of the other fiber. Note the equation depends on the ratio of the two fibers. If one of the fibers is 20% larger than the other fiber ($\omega_1 / \omega_2 = 1.2$) , the loss is about 3%.

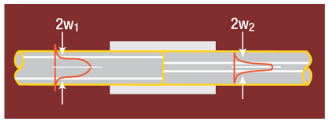

$$Loss = 1 - \frac{4}{\left(\frac{\omega_1}{\omega_2} + \frac{\omega_2}{\omega_1}\right)^2}$$

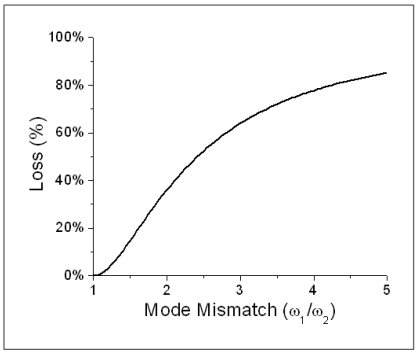

Figure 4.20: *Longitudinal displacement (drawing, analytic equation and chart)[43]*

CHAPTER 5

Component selection and analysis

This chapter will describe the components used in the assembly of the fiber optical position sensor, the main characteristics, providers and working limitations will be explained in order to reproduce or maintain the system.

5.1 Laser diodes and Photodiodes

During this project two wavelengths will be studied in parallel to verify which one is the most suitable for our design. For this, both, photodiodes and laser diodes, should be ordered in different wavelengths 850 and 1310 nm (standard wavelengths in telecommunications) and tested. The component selection in this case is done under the next criteria: power budget (by mean of laser power and photodiode sensibility, the working dynamic range can be optimized and the power budget maximized in order to compensate the loses of other components), bandwidth (the system must sense from 0Hz to at least 10MHz), ocular safety (working with optical powers bellow 5mW), noise immunity (the signal send and received must be as clean as possible) and mechanical (metallic standard connectors with straight tip, ST, are desired for these components).

5.1.1 Components for 850nm

In general the components of this wavelength cheaper than for 1310nm, however they show good performances. The components for 850nm are commonly used with multimode fibre (MMF). To evaluate emitters and receivers, a set of 3 laser diodes and 5 photodiodes were ordered from the companies "Optek", "Kyosemy" and "Laser Components", the selection was done based on their performances. Power and frequency response test where carried out to select the best fitting combination. The table 5.1 shows the results of the evaluation.

LASER DIODES							
Company	Component	Class	Max Curr.	Max Power (dBm)	Max Power (mW)	Stability	Comments
OPTEK	OPF372A	GaAlAs LED	100mA	-10	0.1	Stable	Fine, Low Power
KYOSEMI	KLD085VC	VCSEC	12mA	1.59	1.44	Stable	
LASER COMP	PL85B002ST83-T-0		45mA	6.98	5	Noisy	Noisy (Reflections)

PHOTODIODES							
Company	Component	Class	Sensibility (dBm)	Sensibility (mW)	Saturation (dBm)	Saturation (mW)	Comment
KYOSEMI	KPGX1G	GaAs PD-TIA	-24	3.98E-03	-	-	High-Pass filter F> 1Mhz
KYOSEMI	KPIX150M-H33	Si PD-TIA	-31	7.94E-04	-	-	
KYOSEMI	KPIXAIG-T-ST	Si APD-TIA	-33	5.01E-04	-	-	
OPTEK	OPF562A	Si PD	-41	7.94E-05	-7	0.200	
LASER COMP	PDSIU500ST83-W-0	Si PD	-21.9	6.46E-03	3	1.995	TIA Circ OK F<2Mhz

Table 5.1: *Laser diodes and Photodiodes for 850nm evaluated and results.*

As shown in the table 5.1, the laser diode Kiosemy KLD850VC was selected for its relative good power and stability when there are back reflections. This laser is considered Class 3R, in case the fiber is not connected, and Class 1 once fiber is connected (according to the standard laser classification). Its power is around 1dBm (1.5mW) coupled with MMF, and it is considered enough as it will be seen in following chapters. In terms of stability is also the best candidate: the laser from "Laser Components" showed some noise/inestabilities

due to backreflections in the fiber. In spite of its high power, it is not suitable. Regarding the receivers, the Kiosemy components where discarded, they were designed to work for optical communications its high-pass filter that made them not suitable for low frequencies. Also the "Laser components" photodiode was discarded since it does not have an embedded transimpedance amplifier (some electronic had to be developed to test it and it limited its performance from 0 to 2MHz), moreover it´s dynamic range is not as good as the finally selected component. The "Optek" photodiode proved to be the most suitable; it senses from -41dBm to -7dBm and also has a suitable transimpedance amplifier that works perfectly from DC to more than 100 MHz giving a voltage output easily amplifiable. With this combination of laser diode and photodiode the power budget is about 40dB, which is considered acceptable.

5.1.2 Components for 1310nm

In order to evaluate also single mode fiber usage, some lasers and photodiodes for 1310nm were ordered. The initial selection of components is shown in the following table. In terms of power, the lasers were connected to a single mode fibre (SMF) and its maximal optical power coupled (applying the maximal working current for each laser) was measured. It could be seen that the "Laser components" laser without pigtail (ST direct connection), coupled a very low percentage of power in the SMF (-18dBm), whereas for MMF is suitable (4.56dBm). The BOB Lasers coupled in SMF a power of 4dBm by using a pigtail with ST connector; due to its high coupling efficiency and stability (very little noise) this laser was considered the best for the SMF usage.

LASER DIODES							
Company	Component	Class	Max Curr.	Max Power (dBm)	Max Power (mW)	Stability	Comments
LASER COMP	PL13B002ST83-S-O	InGaAsP	35mA	-18	0.015	Stable	Fine, Low Power
BOB LASERS	BOB1310FP	Fabry Perot	35mA	4	2.5	Stable	

PHOTODIODES							
Company	Component	Class	Sensibility (dBm)	Sensibility (mW)	Saturation (dBm)	Saturation (mW)	Comment
LASER COMP	PTINS155ST83-N-O	InGaAs PIN-TIA	-36	0.00025	-9	0.126	BW = 0Hz to > 15MHz
BOB LASERS	KPIX150M-H33	InGaAs PIN-TIA	-21	0.00794	-3	0.501	High-Pass filter F> 5KHz

Table 5.2: *Laser diodes and Photodiodes for 1310nm, tests and results*

In terms of photodiodes, both components were tested again to check the saturation point and the maximal sensibility reached, as shown in the table 5.2, the BOB photodiode shown a high pass filter that made it not suitable for low frequencies. Its sensibility and saturation where between -21dBm and -3dBm respectively. On the other hand the Laser components photodiode showed a very good behavior and stability in the range between 0 Hz and 15 MHz, having a saturation point of -9dBm and a sensibility of -36dBm, once selected this

combination of laser and photodiode, we have also a power budget of 40dB, as for the MMF.

5.2 Optical Fiber

The selection of an optical fiber is not a trivial problem with the constraints of this application, in the literature is widely known the negative effects observed in the crystalline structure of optical fibre core due radiation exposure [28][42]. In general it can be considered that ionizing radiation can lead to increase its attenuation due to darkening. This radiation response is strongly correlated with the manufacturing procedure of the fiber (materials and dopants) and to the irradiation conditions (dose rate, and cumuled dose). The most remarkable effect in optical fibers exposed to radiation is the Radiation Induced Attenuation (RIA), this RIA depends also of the working wavelength, since the induced losses are not constant along the spectrum.

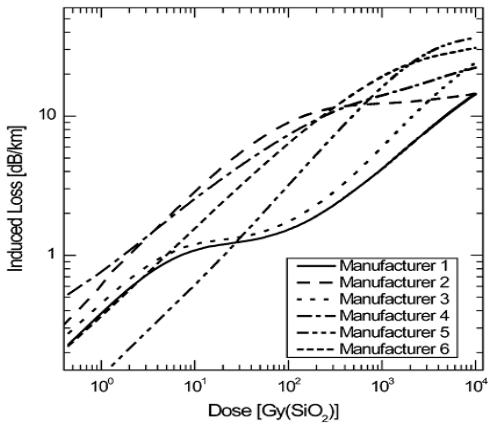

Figure 5.1*: Example of RIA for different fiber providers under the same conditions [42].*

As it has been explained in previous chapters, around 250 m of optical fiber is needed between sensor and electronics and it's potentially exposed to radiaition. The Standard loses and also the RIA should be and taken into account to scale and optimize the optical power budget of the system. According to the specifications, the total radiation dose in 20 years would be 20 kGy (roughly 1 kGy/year), so as less RIA as possible is needed.

"Franhoufer Institute of Technology" has been responsible to carry out studies with different providers, materials, radiation conditions and wavelength response in a big number of optical fibers in order to obtain the standard fibers that should be used in the LHC [29,30,31,32]. These studies reveal that GE-dopped (Germanium) fibers are not good for our environment and that pure silica core could be radiation tolerant. It is also revealed that the usage of other dopants such as Fluorine or high OH ions concentration (bad for high wavelengths such as 1310nm) can improve the radiation resistance of optical fibers under certain conditions. According to their studies and reports, the recommended fibers to use in this project are as follows.

A) Single mode fiber for 1310nm: Draka Elite SMF (F-Dopped)

Table 2: Test conditions for irradiations.

Parameter	Test condition	Remarks
Wavelengths	1310 nm / 1570 nm	Highly stable SLED sources
Attenuation	5 dB	
Light power	6 µW / 6 µW (1310 nm / 1570 nm)	
Sample length	250 m / 250 m	Adjusted for expected total induced attenuation
Distance from source to fibre	8.37 cm / 8.37 cm	Mean distance from fibre sample to point like irradiation source
Dose rate	0.211 Gy/s / 0.210 Gy/s	Uncertainty: ~6%
Total dose	9854 Gy / 9849 Gy	Irradiation time: 46 800 s
Inhomogeneity	< 11%	Relative to mean dose
Total induced attenuation	1.0 dB / 1.0 dB	Total induced loss at the end of irradiation in sample
Annealing time	> 20 000 s	
Temperature	24°C ± 1°C	Room temperature

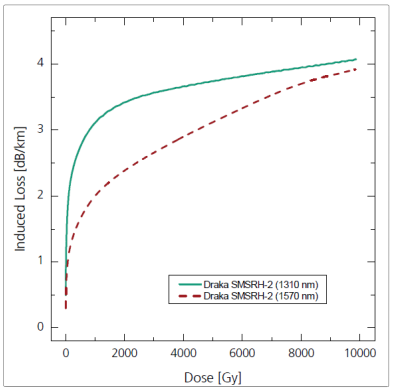

B) Mulimode Fiber for 850nm: Fujikura RRMMFO (High concentration OH)

Table 2: Test conditions for irradiations.

Parameter	Test condition	Remarks
Wavelength	830 nm	Highly stable LED source
Attenuation	none	
Light power	~ -18.6 dBm	~14 µW
Sample length	60 m	Adjusted for expected total induced attenuation
Distance from source to fibre	8.25 cm	Mean distance from fibre sample to point like irradiation source
Dose rate	0.217 Gy/s	Uncertainty: ~6%
Total dose	10164 Gy	Irradiation time: 46 800 s
Inhomogeneity	< 5%	Relative to mean dose
Total induced attenuation	0.63 dB	Total induced loss at the end of irradiation in sample
Annealing time	> 20 000 s	
Temperature	24°C ± 1°C	Room temperature

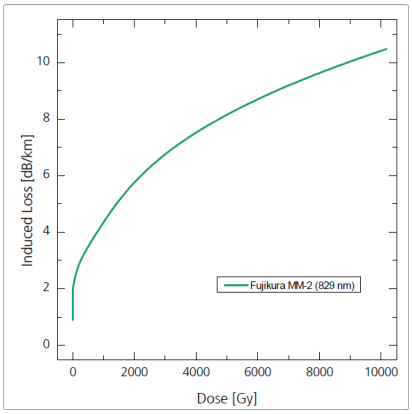

C) Multimode Fiber for 1310nm: Draka Elite GIMMF

Table 2: Test conditions for irradiations.

Parameter	Test condition	Remarks
Wavelengths	830 nm / 1300 nm	Highly stable LED sources
Attenuation	none	
Light power	25 µW / 9 µW (830 nm / 1300 nm)	
Sample length	40 m / 250 m	Adjusted for expected total induced attenuation
Distance from source to fibre	8.23 cm / 8.38 cm	Mean distance from fibre sample to point like irradiation source
Dose rate	0.218 Gy/s / 0.210 Gy/s	Uncertainty: ~6%
Total dose	10204 Gy / 9834 Gy	Irradiation time: 46 800 s
Inhomogeneity	< 4% / < 11%	Relative to mean dose
Total induced attenuation	1.6 dB (830nm) / 1.4 dB (1300 nm)	Total induced loss at the end of irradiation in sample
Annealing time	> 20 000 s	
Temperature	24°C ± 1°C	Room temperature

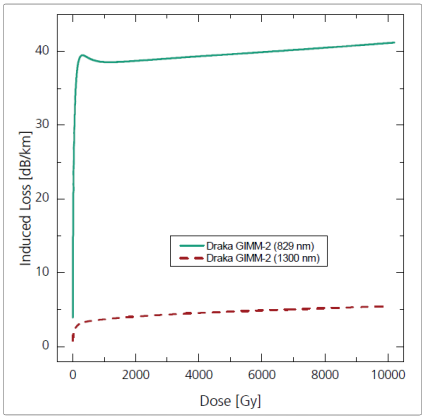

This means that the best candidate is Draka Elite SMF for 1310 nm where the RIA threshold of 5dB/Km has not been reached with a dose of 10 KGy. For usage with MMF and 850nm the Fujikura fibre should be used.

5.3 Circulators and Splitters

In the reflection approaches as explained in section 4.3, where only one fiber is inside the vacuum and responsible to send and collect light, it is necessary to be able to separate the light that the fiber send to the disc, and the light reflected by the slits, which is used for detection. For this circulators or splitters should be used.

A splitter could be defined as a passive device that splits the optical power carried by a single input fiber into two output fibers. This device is able to distribute the optical power carried by input power in an even and uneven manner, giving 10% of the light in one output port and 90% in the other for example, or splitting the signal in equally in the 2 outputs. This is normally done by placing optical fibers very near each other in a way that the light could be coupled. The splitters also work in coupler configuration, the two output ports are used as input to obtain at the input port the sum of the optical power in the other ports. Considering the usage of a Newport Multimode F-CPL-M12855-FCPC MMF 50/50 splitter to separate the light from the laser and the disc reflected by the disc, the losses due to the device are as shown in Fig5.2, considering a perfect mirror in port 2.

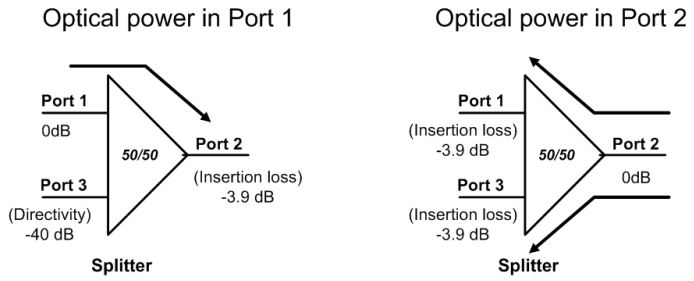

Figure 5.2: *Splitter working principle and power balance*

Validation measurements were carried out on commercial devices and shown in Table 5.3. Considering a perfect mirror in port 2, we´ll have 20% of the optical power in port 3 due to the reflection of the disc in port 2 and a small offset due to the internal communication between port 1 and port 3 of 0.01% (directivity). Another 20% of the power will go back to the port1 where the laser is (this is not good because the stability of the laser could be affected).

In order to reduce the component loses and avoid undesired backreflections in the laser, an optical circulator for single mode fiber **PIOC-3-13-P-2-1-55** was ordered from "Fiberer" and tested. This is another passive device, but not simetrical, as shown in the Fig 5.3, the

internal optical elements (polarizing cubes, Faraday rotators, phase retarder and Birefringent Walls), are configured in such way that the light from port 1 goes directly to port 2, the light from port 2 goes directly to port 3, and the light from port 3 goes directly to port1 with as less losses as possible.

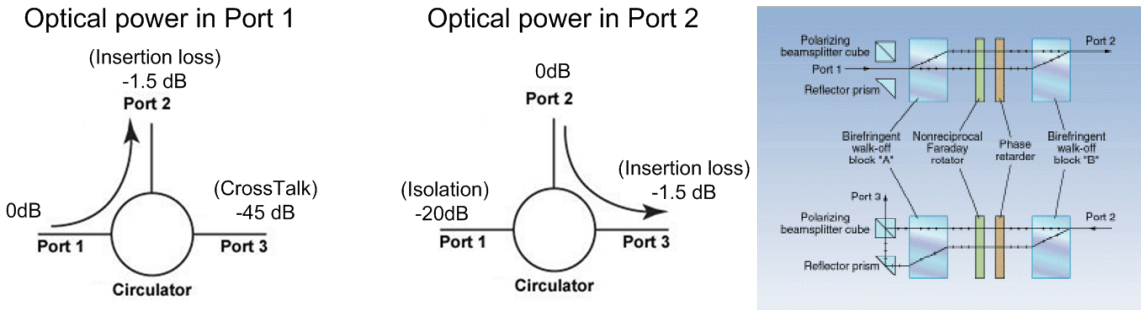

Figure 5.3: *Circulator working principle (left) and internal components (right)*

By using an optical circulator it is possible to see an important improvement, the loses have been reduced, this time instead of a 20% we have a 68% of the light power in port 3 due to the reflection of a perfect mirror in port 2. It is also possible to see that there is not light back in the emitter plane (just 0.001%), so, the stability of the laser is now not perturbed by the undesired reflected optical power.

Light power in ports when 100% in port 1 (Measurements in %)												
	P1in		P2Out		P2in		P3out		P3Offset		Return to soruce	
	Theoric	Real	Theoric	Real	Theoric	Real	Theoric	Real	Theoric	Real	Theoric	Real
Splitter 50/50	100,00	100,00	40,74	47,21	40,74	47,21	16,60	20,84	0,01	0,80	16,60	21,58
Circulator	100,00	100,00	83,18	78,34	83,18	78,34	69,18	68,39	0,003	2,51	0,001	0,001

Table5.3: *Loses comparative Splitter VS Optical Circulator.*

There is also an interesting factor to take into account, there is a signal offset in the port 3 due to reflections in the end of the fiber in port 2, this reflections are produced by the interface silica/air at the end of the fiber, this effect will be explained in detail in the section 6.3.

5.4 Optical Feedthrough

An optical feedthrough is a device designed to introduce optical fiber into the vacuum. This piece consists on a standard flange (normally CF16) that can be soldered or fixed with screws in order to preserve the ultra high vacuum, and a tube that has inside optical fiber with connectors in both sides, rubber pieces or glues are avoided because of the UHV constraints. Since in this project both fiber technologies will be tested and verified in order to select the best approach, two feedthroughs were selected, for MMF and SMF.

5.4.1 Multimode Feedthrogh

The selected feedthrough is **FO-0300-CF16** from the company "Vaqtec". The main characteristics of this piece is that it has metallic SMA905 premium connectors in both sides and step index multimode fiber 62.5/125 (core/cladding), this component is suitable for our bakeout temperature (200 deg) and the ultra high vacuum level reached (1x10^-10 torr). In the vacuum side optical fiber **FOV625-39SMA2** (SI MMF 62.5/125) should be attached to the vacuum connector by using a **FOVENT-C** SMA adapter for vacuum service, these last components were selected from "Accu-Glass Products" and are also compatible with our environment.

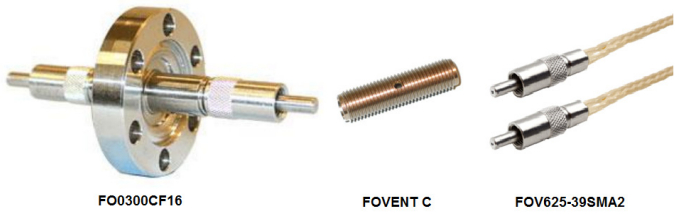

Figure 5.4: *MMF components for Vacuum*

5.4.2 Single-Mode Feedthrough

The provider in this case is "Lewvac", from this company the necessary components would be **FO-SM1300-16CF**, a SM feedthrough of 9.2/125 with FC connectors in both sides, an adapter **FO-FC-CV** and a SMF patchcord for UHV **FO-SM1300VC-900**. All this components reach the specs in terms of vacuum and temperature.

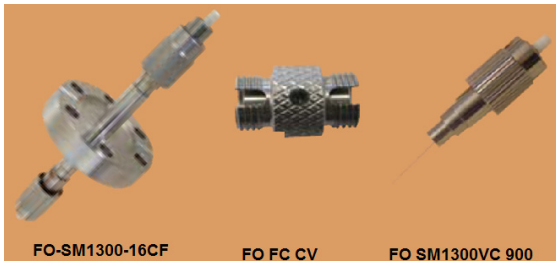

Figure 5.5: *SMF components for Vacuum*

5.5 Lenses

As explained in the in section 4.3, two approaches will need lenses. In our case we need one set of lenses to test a focuser for vacuum and another set of lenses to build focuser that will be placed outside of the chamber and will focus the light on the disc through a viewport. Due to the fact that we are dealing with optical fiber

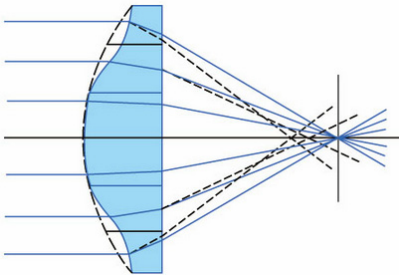

Figure 5.6: *Visual comparison between aspheric lenses (blue rays) and spheric lenses (black rays)*

coupling and that the desired spot size is as small as the core of the fibre, aspheric lenses are needed.

The main advantage of the aspheric lenses with respect to spherical lenses is the reduction of the spherical aberration. This effect reduces the performance of spherical lenses, which are not able to focus perfectly a small spot or collimate perfectly a beam without set of lenses to correct this effect. Aspheric lenses avoid this effect and simplify the design of an optical system, reducing the number of elements needed to obtain very good collimations or focused spots of light. The previous Fig 5.6 show a comparison between aspheric lenses (blue rays) and spherical lenses (black rays).

5.5.1 Vacuum Focuser

The first part of the work was to model and simulate different configurations by using the optical professional software Zemax, its optimization tool helps to find a solution with a single lens. The system is able to modelate an optical fiber with N.A. of 0.22 (for MMF) or 0.14 (for SMF) and focus its output light in a spot size as small as possible with the minimum aberration possible. Simulations over several commercial lenses were performed using, two wavelengths (850 and 1310nm). Finally the lens model 352400 from "Lightpath" was selected. One of the main advantages of this lens is that has a magnification factor of 2, so the focused spot size could be 2xFiber Core diameter (or Mode Field Diameter) or ½xCore diameter.

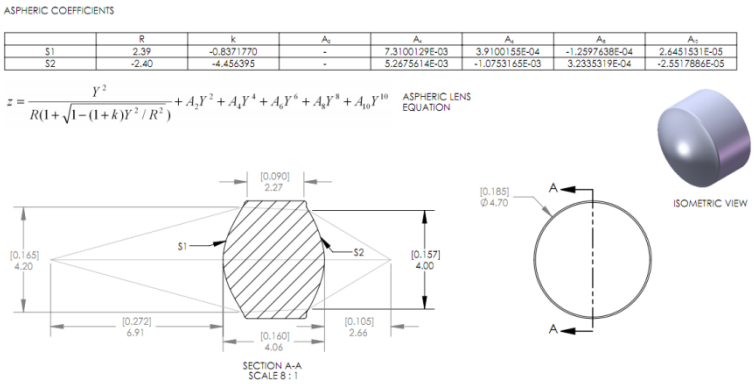

Figure 5.7: *Characteristics of lens 352440*

This lens is made of ECO550 glass, according to the characteristics of this kind of glass the transformation temperature is 364ºC, the deformation point is at 398ºC and the expansion coefficient of 13.1×10^{-6}/ºC. These characteristics are compatible with the specifications and hable to cope up with the constrains of the working environment. Private

communications with the provider also confirm that the glass can be used in UHV without problems. Since no information about radiation was available, further studies will address this part of the specs. The custom housing that should be built to hold the lens and connect the focuser to the end of the optical fiber shown in Fig 5.8. All the components are made of aluminium, without plastic pieces, not painted, nor glued, so the vacuum and temperature compatibility is guaranteed. This assembly is flexible enough to calibrate and fix the distances D1 and D2 (shown in Fig 5.8 right).

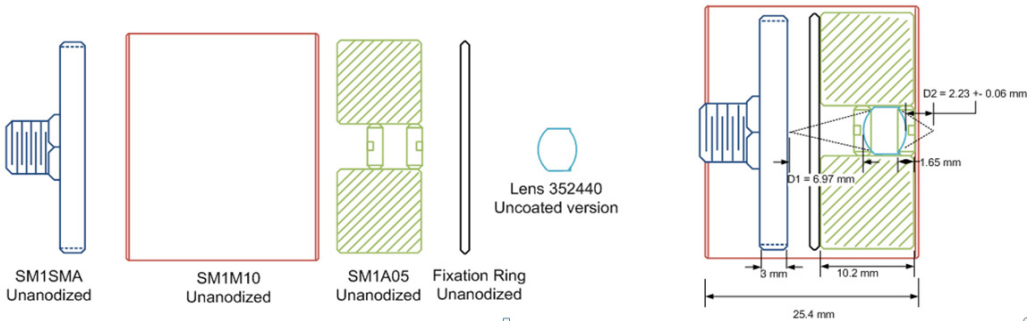

Figure 5.8*: Vacuum Focuser assembly with "Thorlabs" commercial components*

5.5.2 External Focuser

The main constrain of using an external focuser is the need of very long focal distance D2 in order to focus and collect the light on the disc after crossing the tank wall through an optical viewport. The mechanical characteristics of the current design impose this distance to be bigger than 80mm. Since no commercial single aspheric lens was found with such long focal distances, a pairs of aspheric lenses was used to build our external focuser. A focal distance of 100mm between the end of the focuser and the disc was imposed. Moreover, its known that the magnification factor of a system of lenses depends of the relationship between the first and second focal distance, so for a system 1:1 we need two lenses of F=100mm, for a system 1:2 on F2=100mm and F1=50mm, and for a system 1:1/2 F2=100mm and F1=200mm.

Again Zemax simulations were done to obtain the most suitable aspheric lenses with the best response and characteristics in terms of spherical aberration and behaviour, the aim was to select a pair of aspheric lenses to build a system 1:1 and another pair to build a system 1:2. To limit the size of the focuser the option 1:1/2 was discarded, since the resulting focal distance F1 should be 200mm. The lenses selected are the models from Thorlabs 2xAL50100-C (Focuser 1:1 in figure5.9) and Thorlabs AL2550-C & AL50100

(Focuser 1:2 in Fig.5.10). In this case the focal distance between the connector and the first lens is fixed and the separation between lenses is variable to calibrate the focused light on the disc. The lens is done of standard lens glass N-BK7 while the assembly is made of anodized aluminium. One of the main advantages of this external focuser is that could be easily calibrated from outside once the system is installed in the tunnel.

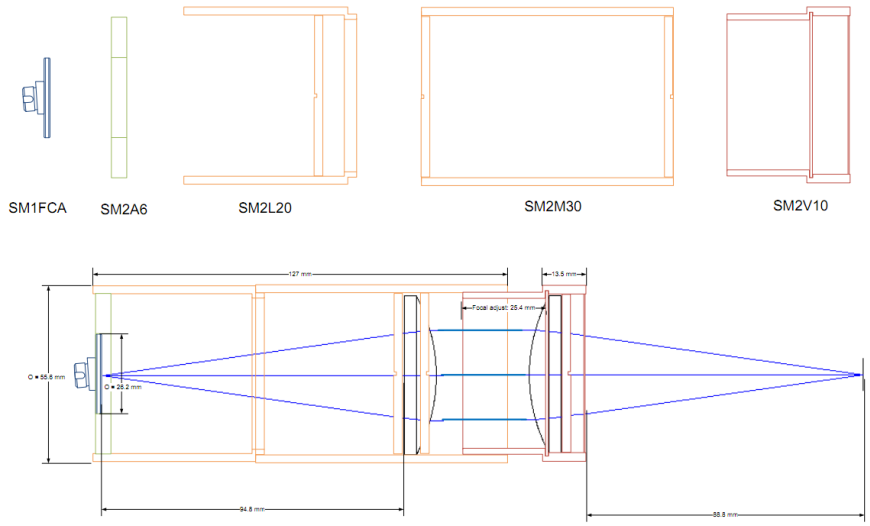

Figure 5.9*: External focuser with system 1:1 full assembly (down) and components (up)*

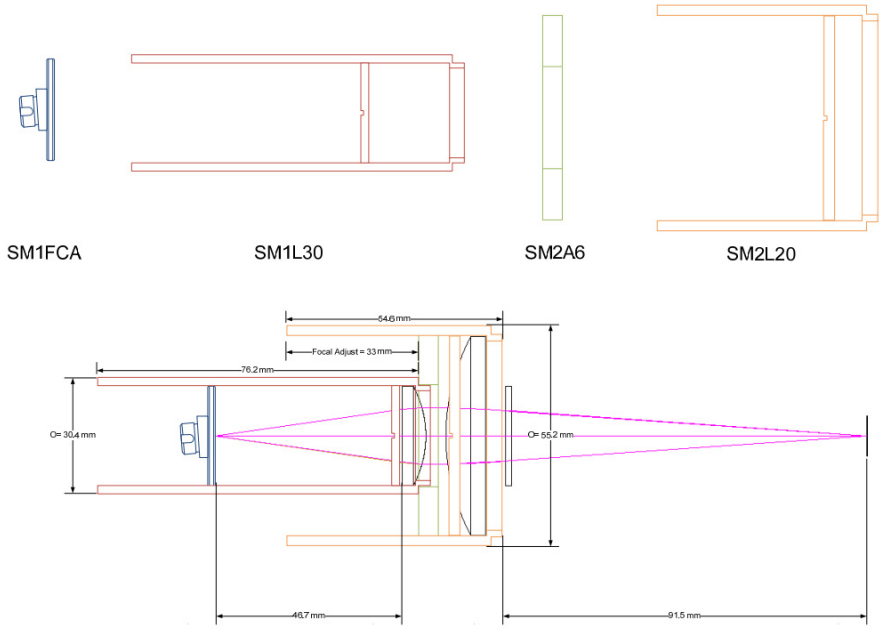

Figure 5.10: *External focuser with system 1:2 full assembly (down) and components (up)*

5.6 Optical encoder disc

The optical encoder disc is the central part of the system, and its design (slit size and accuracy) is what defines the maximum accuracy and resolution reachable by the system. Selba.S.A is the provider of this part.

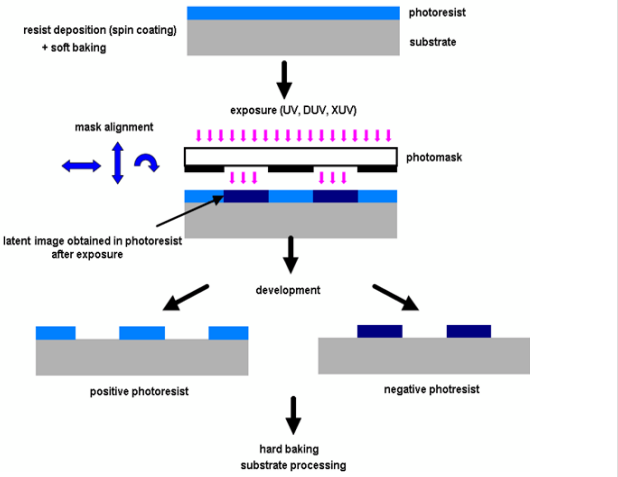

Figure 5.11: Manufacturing an encoder disc.

To obtain one endoder disc the photolithography process is used, this process uses UV light to transfer a geometric pattern from a photomask to a light-sensitive chemical resine on the substrate that protects the metal located bellow. The steps followed are represented in the figure 5.11.

The initial material is a glass substrate with a metallic layer on one of its faces; finally a layer of protecting photosensitive resine is deposited by spin coating. To have a pattern of metal, the desired places of this material are exposed to UV light by using a photomask, this makes the resine react with the UV light changing its properties (as in the case of electrical circuits). The next step is a chemical bath to remove the metal that is not protected by the resine.

During this thesis two designs were used in order to have as different slit sizes to verify all the approaches proposed in the previous chapters.

5.6.1 Optical Disc Version 1

The disc material used is the Borofloat glass ue to its excellent transmittance (Transmittance=90%) in a wide range of wavelengths, with this glass it´s possible to verify in practice the transmission approach minimizing the absorption loses. The patterns of slits are made of high reflexivity chrome (Reflexivity=60%) in order to verify the reflection approaches. The design of this first version consist of a disc of 140mm of diameter with a hole of 40mm in the centre with 8 tracks of slits with different width (50, 75, 100 and 150 μm) with an accuracy of 2μm, using a positive and a negative mask as shown in the Fig 5.12. Several disc of different thickness were ordered (0.5, 1 and 1.5mm).

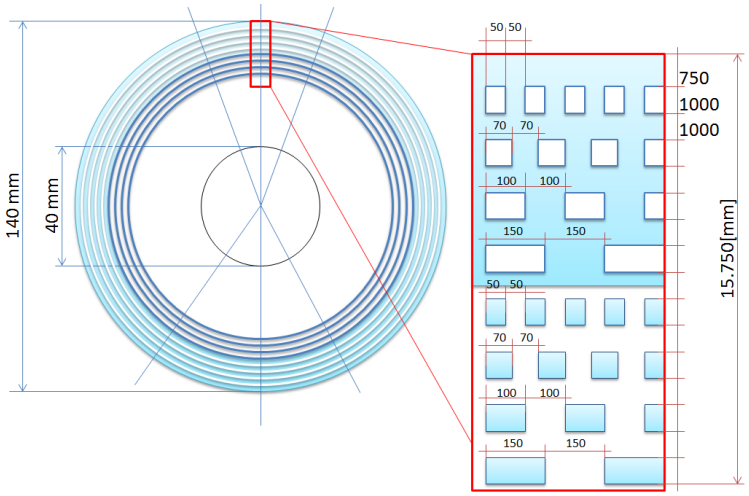

Figure 5.12: *Optical Disc V1*

On the table 5.4 the different characteristics of the tracks are calculated. It is shown that the accuracy and resolution are not met with this disk. Interpolation methods may be used to overcome the lack or resolution (desired: 0.0286 deg), with regard to accuracy (desired: 1.43e-3 deg); it is determined by the fabrication process and calibration algorithms must be used to reach the specs.

DISC V1 SLITS DETAILED SPECIFICATIONS						
Track	Alpha (deg)	Acc (deg)	Edges	Freq (Hz)	Diam center Slit (mm)	Do (um)
1	*0,042*	*1,67E-03*	*8633*	*1,37E+05*	***137,5***	*50,036*
2	*0,063*	*1,69E-03*	*5678*	*9,04E+04*	***135,5***	*74,968*
3	*0,086*	*1,72E-03*	*4196*	*6,68E+04*	***133,5***	*99,958*
4	*0,131*	*1,74E-03*	*2754*	*4,38E+04*	***131,5***	*149,985*
5	*0,044*	*1,77E-03*	*8145*	*1,30E+05*	***129,5***	*49,950*
6	*0,067*	*1,80E-03*	*5341*	*8,50E+04*	***127,5***	*74,992*
7	*0,091*	*1,83E-03*	*3943*	*6,28E+04*	***125,5***	*99,991*
8	*0,139*	*1,86E-03*	*2588*	*4,12E+04*	***123,5***	*149,935*

Table 5.4: *Specifications of the Optical Disc V1*

5.6.2 Optical Disc Version 2

The second version of the disc contains much smaller slits (8 tracks: 5, 10, 15, 20, 25, 30, 35 and 50 um) with an accuracy of 1um; the reflective surface is again high reflexivity chrome. The aim of this design is to reach as much resolution as possible with the same disc diameter. In this disc there are two gaps without slits (see Fig 5.13) in order to have absolute references for the position processing and to calibrate the scanner.

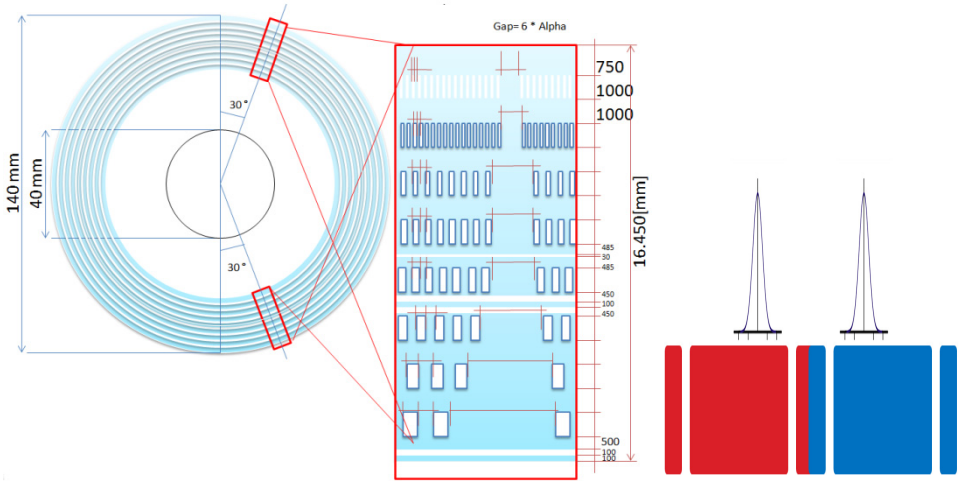

Figure 5.13: *Optical Disc V2 (left) and representation of a scan up (red) and down (blue) to locate the beam (right)*

This second version of the encoder disc reaches in 6 of its 8 tracks the specifications in terms of accuracy and resolution by using only one channel.

DISC V2 SLITS DETAILED SPECIFICATIONS						
Track	Alpha (deg)	Acc (deg)	Edges	Freq (Hz)	Diam center Slit (mm)	Do (um)
1	0,004	1,67E-03	90000	1,43E+06	137,5	4,800
2	0,009	1,69E-03	40000	6,37E+05	135,5	10,642
3	0,012	1,72E-03	30000	4,77E+05	133,5	13,980
4	0,015	1,74E-03	24000	3,82E+05	131,5	17,213
5	0,020	1,77E-03	18000	2,86E+05	129,5	22,602
6	0,025	1,80E-03	14400	2,29E+05	127,5	27,816
7	0,030	1,83E-03	12000	1,91E+05	125,5	32,856
8	0,045	1,86E-03	8000	1,27E+05	123,5	48,498

Table 5.5: *Specifications of the Optical Disc V2*

5.7 The optical test bench

To validate the proposed approaches with high accuracy, an optical test bench was built by the design team of the wire scanner. This test bench has all the needed components to simulate the behaviour the optical sensor of a wire scanner, as it shown in Fig 5.14 there is a DC motor and a rotating shaft hold by rolling bearings.

The optical disc is in the middle of the shaft, fixed with custom pieces in order to be able to exchange the disc easily. Finally the optical feedthroughs are mounted using micrometer mobile stages, they are mounted in such way that Fiber A is fixed in XYZ but can be tilted and the other fiber (Fiber B) is mobile in XYZ and can also be tilted (group 1, red arrows), this way two fibers can be aligned to couple light with as less losses as possible. There are also other group of mobile stages (group2, green arrows) which is able to move the whole

system (the two fibers) at the same time, keeping this way the alignment of the fibers, and allowing a precise positioning of the two fibers with respect to the disc to select the desired track. The whole system has accuracy in the order of tens of micrometers.

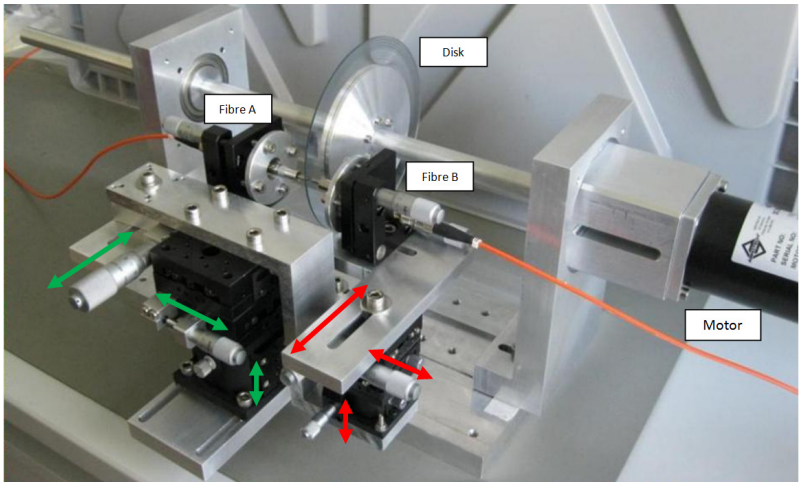

Figure 5.14: *Optical Test Bench*

The relative disc movements with respect to the fibers were precisely identified. The measures taken reveals movements in the axial direction in the order of 25µm, whereas in redial direction eccentricity of the disc and the shaft produces movements in the order of 100µm, all this imperfections should be taken into account in order to design a tolerant system able to cope with it and not lose accuracy or light power.

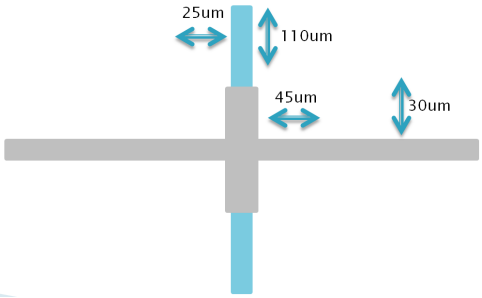

Figure 5.15: *Test Bench characterization*

5.8 Electronic development

Since the system should be as flexible as possible, in some cases the power of the laser can saturate the photodiode in the presence of signal. To avoid this, an electronic circuit was designed to control the laser power. This driver controls the intensity of the laser by limiting the current in the diode in order to reduce or increase the output light power.

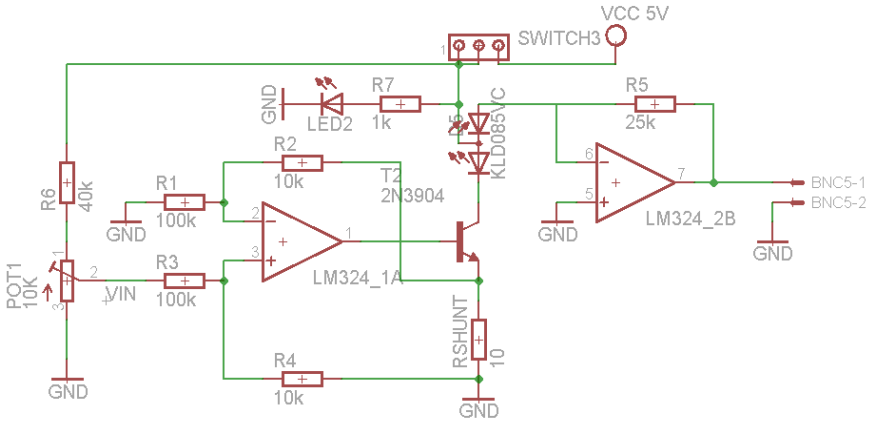

Figure 5.16: *Voltage controlled current source and transimpedance amplifier for the LD's*

The laser driver developed (Figure 5.16) is a voltage controlled current source, this circuit uses a Howland current pump with a current booster. Basically the output of an operational amplifier LM324 uses a transistor 2N3904 as current booster. To sense the current, this circuit uses voltage drop across a shunt resistor (RSHUNT), in series with the Collector/Emitter of the transistor and at the same time with the laser, this voltage drop is measured differentially. The voltage input which controls the current of the laser is provided by a voltage divisor formed by a resistor and a potentiometer (R6 and Pot1). Giving this way, a voltage input between 0 and 1V. The values used in the figure bellow are calculated to control the 850nm Laser for MMF KLD085VC, the max Vinput= 1V equals 10mA in the laser, 2mA less than the maximal current applicable to this component according its datasheet. Other values of scale factor (Vin/Iout) to test different lasers can be set by choosing different resistor values using the equation 5.1:

$$\frac{V_{IN}}{I_{OUT}} = \frac{R_3}{R_4} \bullet R_{SHUNT} \text{ and, } R_1 = R_3, R_2 = R_4 \qquad (5.1)$$

Some laser diodes also have a photodiode integrated such as the laser KLD085VC with the aim to design a feedback network to control automatically its output light power. For this, since the photodiode offers a current proportional to the light (0 to 40uA in this case with max optical power), a transimpedance amplifier is needed, see the figure 5.16 right part, this simple circuit is build by the resistor (R5) and another amplifier LM324. The photodiode is polarized with a reverse voltage of 5V; since the desired output is Vo=-1V when Ipd=40uA the value of R5 will be Vo/Ipd=25Kohm.

All the electronics needed to power the laser and see the signal collected by the receiver photodiode in an oscilloscope, has been integrated in a metallic box (see Fig 5.17). This way the components are well hold and the test can be done easily. It has been built in a way that the power of the laser can be modified with the potentiometer, and the response of both, the integrated laser photodiode, and the system receiver (OPF562A for MMF) could be measured using a BNC cable. It also could be possible to modulate the laser directly with a function generator in order to test receivers (see Figure 5.17).

Figure 5.17: *Electronics for the optical E/R system (up) and for RON225 commercial encoder (down)*

As it was also needed to acquire the signal from a commercial encoder RON225 series from Heidenhain, a 15-pin D-Sub female connector and some bnc's were integrated in the box, as well as the internal cabling needed to power and acquire the signals, figure 5.18 shows the encoder and its pinout.

12-pin flange socket or coupling M23 — 12-pin connector M23

15-pin D-sub connector at the encoder — 12-pin PCB connector

	Power supply				Incremental signals						Other signals		
	12	2	10	11	5	6	8	1	3	4	7	/	9
	4	12	2	10	1	9	3	11	14	7	13	5/6/8	15
	2a	2b	1a	1b	6b	6a	5b	5a	4b	4a	3a	3b	/
	U_P	Sensor U_P	0 V	Sensor 0 V	U_{a1}	$\overline{U_{a1}}$	U_{a2}	$\overline{U_{a2}}$	U_{a0}	$\overline{U_{a0}}$	$\overline{U_{aS}}$ [1]	Vacant	Vacant [2]
	Brown/ Green	Blue	White/ Green	White	Brown	Green	Gray	Pink	Red	Black	Violet	–	Yellow

Figure 5.18: *Heidenhain RON 200 series encoder and pinout*

CHAPTER 6

Simulations, experimental tests and results

This chapter focused on the analysis of different solutions in order to obtain the best accuracy with as less loses as possible in the interface Disc/Fiber. Optical simulations with Zemax and experimental validation will be performed. A power balance will be shown in this comparison as well as various problems found and solved during the work.

6.1Experiments designs and tolerance analysis

In order to characterize the different solutions for the system, the two kind of optical fibers (SMF and MMF) will be considered, as well as two different wavelengths (850 and 1310 nm) to check if there is any dependence between the loss produced for the free space and the wavelength used. The methodology followed includes, at first optical modeling and simulations with the professional software Zemax ® V.12, and practical verification with the testbench. The simulations are performed in a different way depending if the fiber coupling is SM or MM, considering Gaussian Optics for the first case and geometric optics for the second one.

For the Gaussian optics and SMF configurations Zemax ® Physical optics propatation (with POPD and FICLP operands) and Fiber coupling Calculation (with FICL operand) are used. The fiber is modeled with light 5 sources (one in each side of the fiber and other in the centre) with a N.A. 0.14 and telecentric configuration see Fig. 6.1. In the Phisical optics, a Gaussian beam will be considered with a waist radius of 4.6um, according to the characteristic mode field diameter (MFD) of the fiber for at 1310nm.

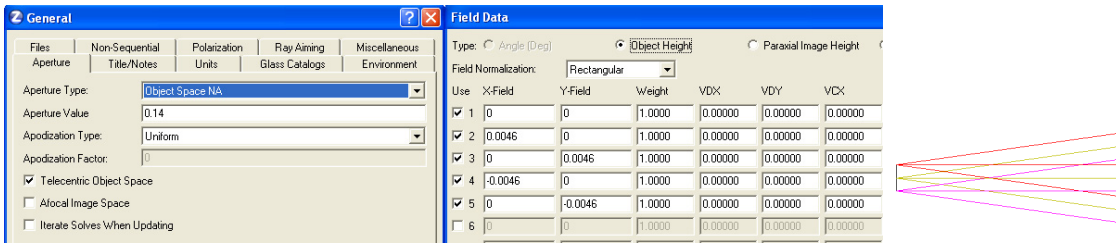

Figure 6.1: *Modelization of a SMF in Zemax ®.*

For the geometrical optics calculations for MMF, the module "Geometrical image analysis" is used (with the IMAE operand). In this case the fiber is modeled with a N.A=0.22 and five fields, one in each side of the fiber and other in the centre again, forming this way a fiber with a core of 62.5um.

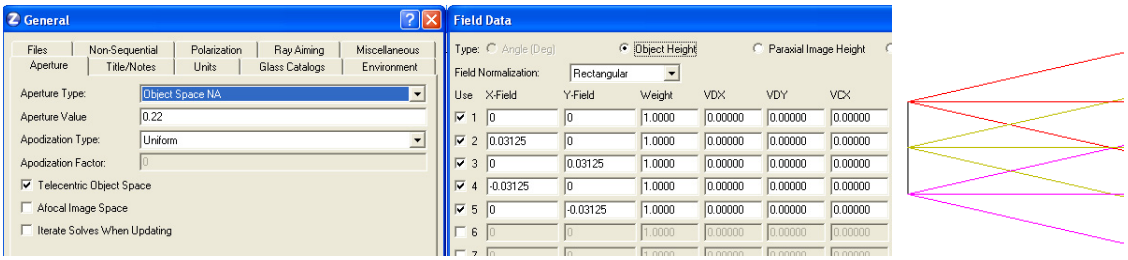

Figure 6.2: *Modelization of a MMF in Zemax ®.*

6.1.1 Transmission

In this first configuration the disc is located between two optical fibers for vacuum, attached to two feedthroughs (or directly between two feedtrhoughs as in Fig 6.3) according to the components for vacuum explained in the previous chapter. In this assembly, one fiber sends light whereas the other collects the light as the disc turns, detecting this way obstructions produced by the chrome slits, see Fig. 6.3. The minimum detection capability is defined by the core size of the receiving fiber. The system can detect ideally slits about 62.5um for MMF and slits of 10um for the case of the SMF. Since in this configuration the minimal distance between fibers is the thickness of the disc, the losses are important. Additionally to this distance, a security margin between the disc ant the fiber of 250 or 500µm is added in each side of the disc to avoid contact case of vibrations or imperfections, which adds even more loses to the coupling efficiency.

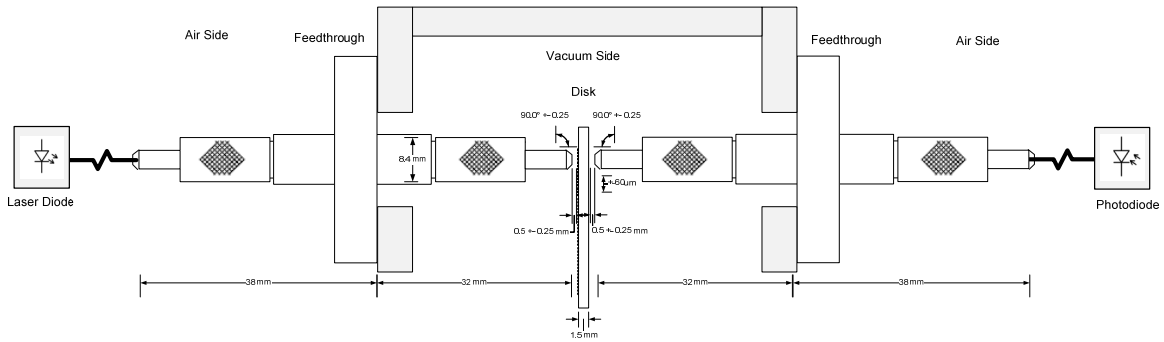

Figure 6.3*: Transmission layout assembly with tolerances*

As shown in the Fig. 6.4, the coupling efficiency expressed in decibel (dB) versus fibers separation in millimeters has been produced. The Zemax simulations for SMF, in green, and for MMF, in red, are shown. The continuous lines represent two fibers that have been separated without the disc, whereas in the dashed a disc of Borofloat has been introduced in the middle with a thickness of 1.5mm. The loss in SMF presents more dependency to distance (short distances) due to its small core. The dashed lines are also showing that with the disc, the coupling efficiency is better than without. The effect of the disc presents a reduction in the N.A inside the glass, which means in the receiver plane that the cone of light is smaller. These theoretical values have been validated with experimentations obtained on the testbench for the two wavelengths (850nm in orange and 1310nm in blue), following the same notation. The experimental verification (done only with MMF) shows a behavior similar to the simulations and moreover no significant wavelength dependency in the coupling efficiency. It can be considered as a fixed loss due to the free space around

18dB for MMF and 22dB for SMF taking into account a distance fiber/disc of 250um in both sides. In order to complete a power budget analysis, the related components loss should be added to these free space losses (2 x Feedthrough + Cables loss ~ 5dB).

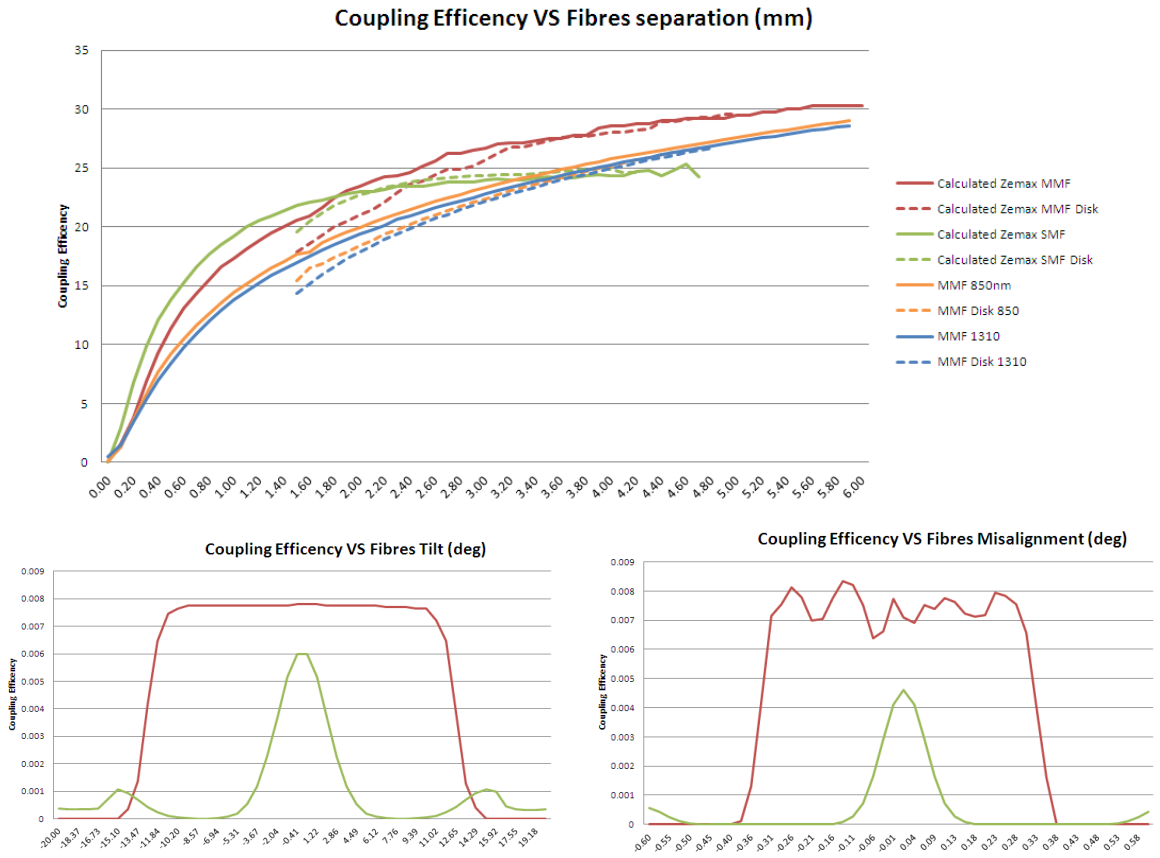

Figure 6.4: T*olerance analysis of the transmission approach*

Other possible sources of loses have been analyzed, such as the misalignment and the tilt, in order to provide a robust tolerance analysis in case of building the encoder with this approach. With this methodology way a frame of specifications can be provided. Following the same colors, a fiber tilt analysis has been performed with the two fibers (coupling efficiency in %), taking into account again the disc and 250um fiber/disc in both sides. As shown in the Fig 6.4 (down left) for MMF (core of 62.5 um and N.A 0.22) the tilt tolerance is much bigger than in the case of SMF (core 9.2um and N.A. 0.14). This is due to the bigger core and the numerical apertures, being around 13^{o} whereas for SMF is 2.5^{o}. In the case of the misalignment analysis, the tolerances are much more relaxed with MMF, being 350um whereas with the SMF the maximum misalignment allowed is 50um.

Some simulations were performed also with Zemax in order to verify the detection capability of this approach. For that slits of 100, 50 and 10 um for MMF and 50, 10 and 5um for SMF were taken into account. The slits were applied to a glass surface type N-BK7 with 1.5mm of thickness to model the disc. The charts of Fig 6.5 are representing the coupling efficiency while the desired pattern is moved 180um; by these techniques we can have an idea of the expected when the disc will be moving. Comparisons with experimental values are also shown.

Sim. MMF 100um

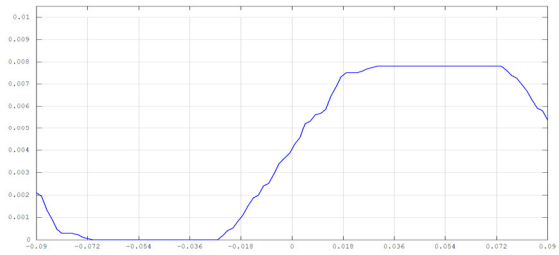

Sim. MMF 50um

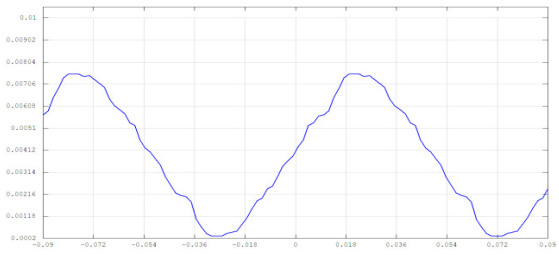

Sim. MMF 10um

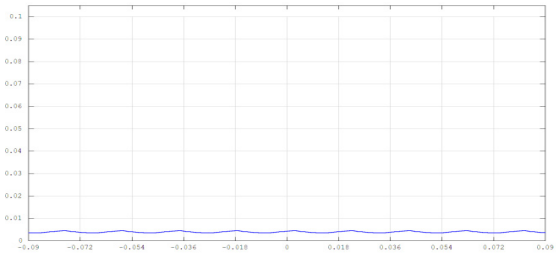

Real MMF 50 um

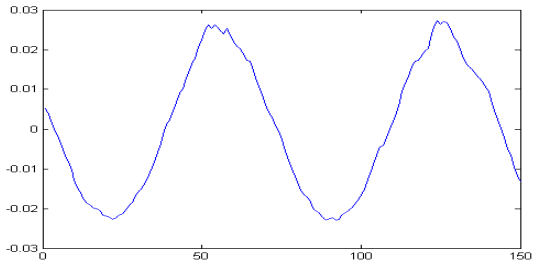

Figure 6.5: Transmission *MMF simulations with different patterns size and experimental verification.*

Sim. SMF 50um

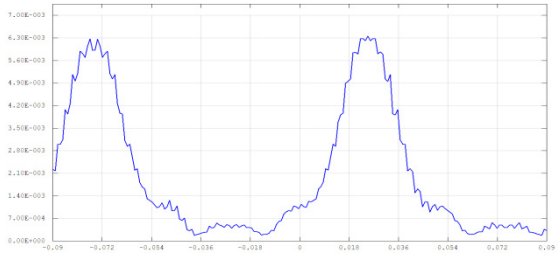

Sim. SMF 10um

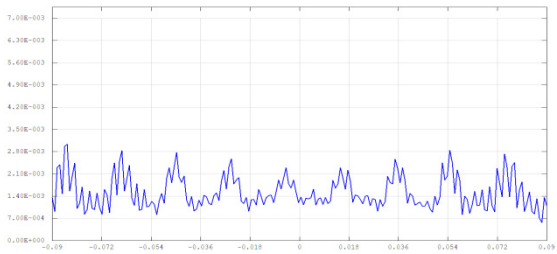

Sim. SMF 5um

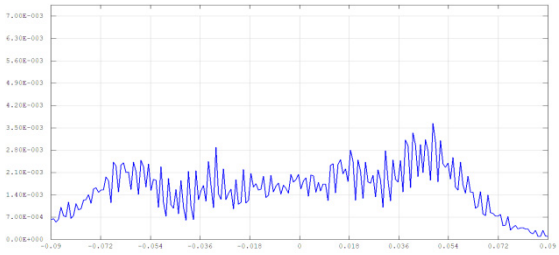

Figure 6.6: Transmission *SMF simulations with different pattern sizes.*

In the case of the MMF, it can be seen how the signal is easily detectable within the slit range 100-50um having the same peak coupling efficiency. But once the slits goes smaller, the light coupled is reduced almost to no signal, and the difference between states is not clear (see Fig 6.5). The experimental verification of the MMF simulations shows how the real acquired signal respects the shape simulated, being almost a perfect sinusoid.

In the case of the SMF, physical optical effects such as Fresnel diffraction are playing an important role. Once laser light crosses a slit, a new source is created and since in the SMF fiber is a coherent source, the different light sources created by each slit are generating interferences in the receiving fiber. This effect can be observed in the simulations with slits of 10µm, where the light signal received is quite sharp and noisy (see Fig 6.6). Moreover it is possible to see that in this case the coupling efficiency with SMF is quite low. In order to understand the Fresnel effect shown in Fig. 6.7, and its distance dependence, a Matlab graphical user interface (GUI) was developed. This GUI simulates the Fresnel diffraction effect with two slits, see Table 6.1 where the red lines represent the slits of 10um and the blue ones is the intensity profile of the light in a screen located at different distances. The source is considered at 1.75mm of the slits (Disc thickness + emitter fiber distance), the receiver plane at has been placed at different distances (50,100,150 and 250um).

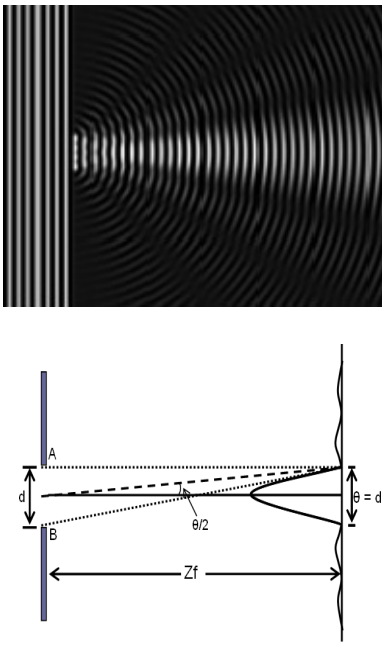

Figure 6.7: *Fresnel diffraction representation*

Fresnel diffraction at different distances (Far field)			
D=50um	**D=100um**	**D=150um**	**D=250um**
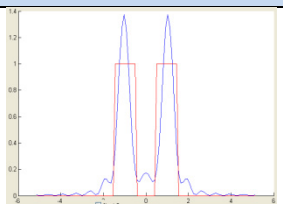	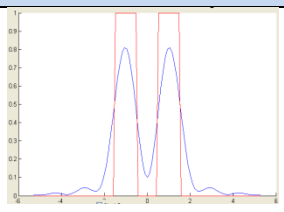	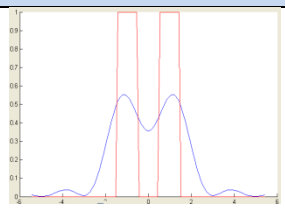	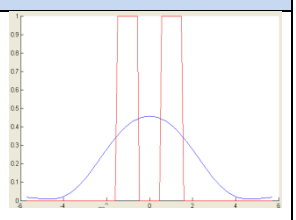

Table 6.1: *Light intensity distribution after two slits in different receiver distances, modelised with the Matlab GUI tool developed for this project.*

According to the Fresnel diffraction, the Fresnel distance is defined as $F_{dist} = {SlitDiam^2}/{\lambda}$, giving as a result a Fresnel distance of 7um for a laser of 1310nm. This means that, in theory, if the distance slits/receiver is bigger than F_{dist}, it can be considered as far field approximation and the light diffracted will be bigger than the slit. In this situation, is possible that close slits are creating interferences to each other, losing this way a good detection capability for this transmission approach. For this reason, as it's shown in the Table 6.1, the SMF is not considered as suitable for the transmission approach. The receiver fiber must be placed too near from the slits to have a good detection capability. To sum up, the Table 6.2 presents a synthesis of the transmission configuration results.

	Fibre type	Disk/Fibre	Distance Tol.	Tilt Tol.	Misalilgnment Tol.	Free Space Loss	Component Loss	Received signal	Detection
Transmission	MMF	250 um	250 um	13 deg	350 um	18 dB	5 dB	0.50%	>62.5um
	SMF	250 um	250 um	2.5 deg	50 um	22 dB	5 dB	0.19%	>10um

Table 6.2: *Remarks of the transmission approach analysis*

6.1.2 Reflection

In this second approach, the light reflected by the high reflectivity chrome pattern of the disc is used to detect angular movements. With this configuration, only one fiber is needed inside the vacuum to send and receive light, as shown on Fig. 6.8, the characteristic of this approach is that a device must be used outside to split the light sent to the disc and the received by the reflection. An optical circulator or splitter is needed for this function (see section 5.3). Avoiding the usage of the disc transparency characteristics that implies a minimal separation between the emitter/receiver fibers, the fiber can be placed close to the disc reducing this way the free space loses. However the chrome reflectivity is 60%, and this percentage the light is returned (fixed loss of 2.21dB). As in the transmission approach, the slit detection capability depends of the fiber core size ideally 62.5um for MMF and 10um for SMF.

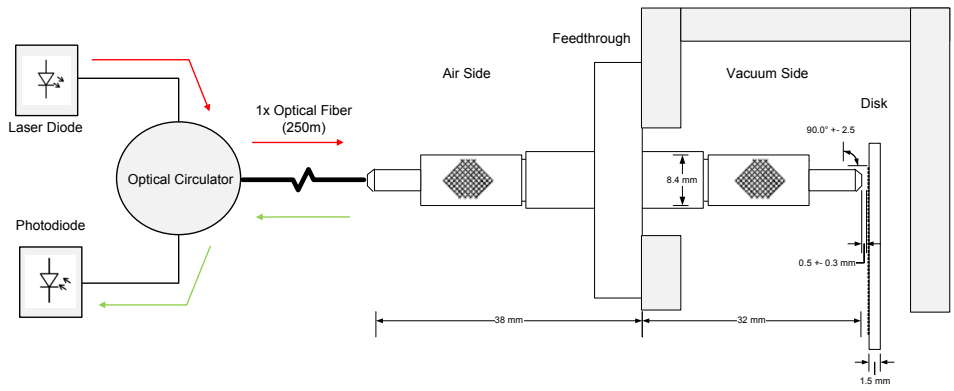

Figure 6.8: *Reflection approach schematic*

All the possible sources of loses were studied in order to provide a robust tolerance analysis. The most significative parameter to take into account in this approach is the distance fiber/disc. Since an optical fiber is used, its numerical aperture and the core size will define the power which will be coupled back in the fiber and re-directed with the circulator to the photodiode. As in the transmission approach, different wavelengths were studied (850 and 1310nm) to verify if the disc reflection varies with this parameter. The dependency of the coupling efficiency to distance for SMF and MMF was also studied.

In Fig. 6.9 different Zemax simulations are presented (red for MMF and Green for SMF). These simulations were obtained by variating the distances disc/fiber between 0 and 1mm, obtaining the coupling efficiency (shown in dB). As in the previous approach the usage of SMF means more loses with the distance compared to MMF. These theoretical results were validated by experimental measurements on the testbench. As shown in Fig 6.9, the purple line presents measurements with SMF, whose tendency follows roughly the theoretical calculations (green). The experimental validation with MMF presents a closer behaviour with the theory (orange for 850 and blue for 1310nm) where we can see that using 1310nm generates less loses. Considering a security distance of 250µm disc/fiber, the loses of the free space for SMF are around 15dB whereas for the MMF are around 8dB. Taking both into consideration the 0.6 reflection coefficient of the chrome. These results present an improvement of the coupling efficiency in the order of 5dB in both fibres with respect to the transmission configuration.

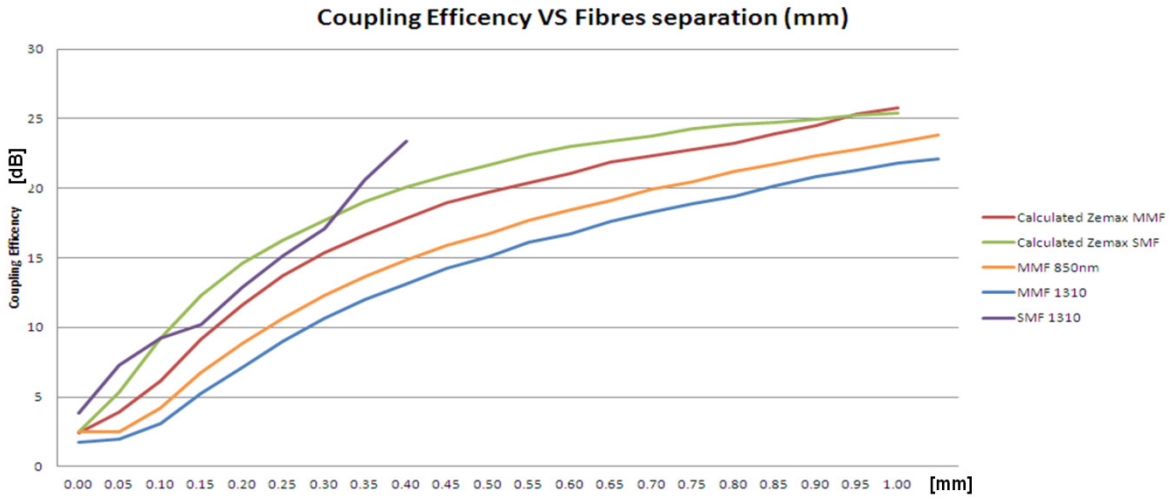

Figure 6.9: *Coupling efficiency (dB) VS Fiber/Disc (mm) separation for reflection approach*

The tilt tolerance was also studied to obtain the maximum nominal error admissible in the assembly. As in the previous approach, the data is provided by simulations of the two fibers at a distance of 250um. The chart in Fig. 6.10 presents the tilt applied in degrees versus the coupling efficiency in percentage. As expected, the MMF (red) a larger tilt tolerance, (around 10^{o}) than the SMF which only accepts a maximum tilt of 2.5^{o}.

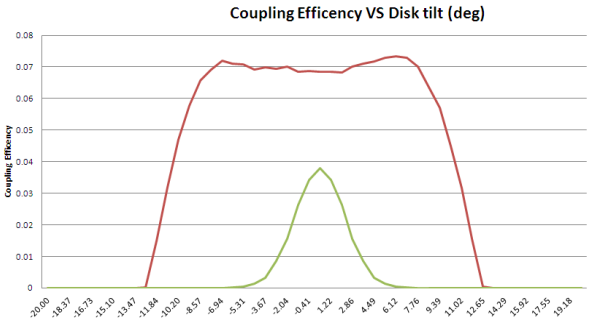

Figure 6.10: *Tilt tolerance (%) analysis for reflection*

Following these studies, another set of simulations were performed to verify the detection capability for each kind of fiber. The slit sizes used are the same as the previous approach (100, 50 and 20µm for MMF and 50, 10 and 5 µm for SMF), and the movement applied is again 180µm.

For the MMF, as in the transmission approach, slits of 100µm produce square signals with more amplitude than before since the coupling efficiency is better. Once the core of the fiber (62.5µm) is in the order of the slits (50µm) this signal is a sinusoid with the same amplitude as the previous one. These theoretical results have been validated with experimental measurements, shown in Fig.6.11. Once the slits are reduced to lower sizes, it is possible to see a large attenuation of the sinusoid signal as shown in the simulation of 20µ. There is compromise between amplitude and resolution. For this approach, is advisable the use of slits around 50µm to obtain the maximal amplitude. To have better angular resolution the slit size can be reduced until 20µm.

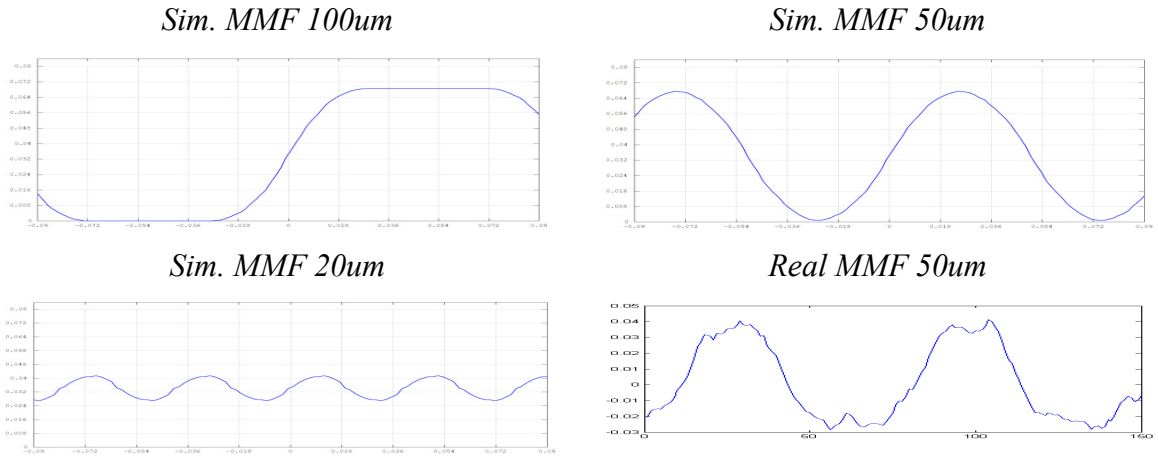

Figure 6.11:Rf. *MMF simulations with different patterns size and experimental verification*

The simulations of the SMF with physical optics in Zemax shows some evidences of Fresnel diffraction, this time the chrome is acting as reflecting surface and it can be also considered as slits in the Fresnel calculations. The most obvious evidence is the ringing of the edges in the case of the 50µm slits, this ringing is typical in the near field approximation of the Fresnel diffraction. Its signal has been experimentally validated and can be seen in the Fig. 6.12. A similar effect as in the transmission approach is happening while reducing the size of the slits. Due Fresnel diffraction, the coupling efficiency decreases as the slits decreases its width, the signal is still visible and detectable when the slits are around 10um, but once the value is lower, the detection capability is almost lost. These simulations have driven us to conclude that the usage of SMF in the reflection approach is limited only to slits in the order of 10mm or bigger.

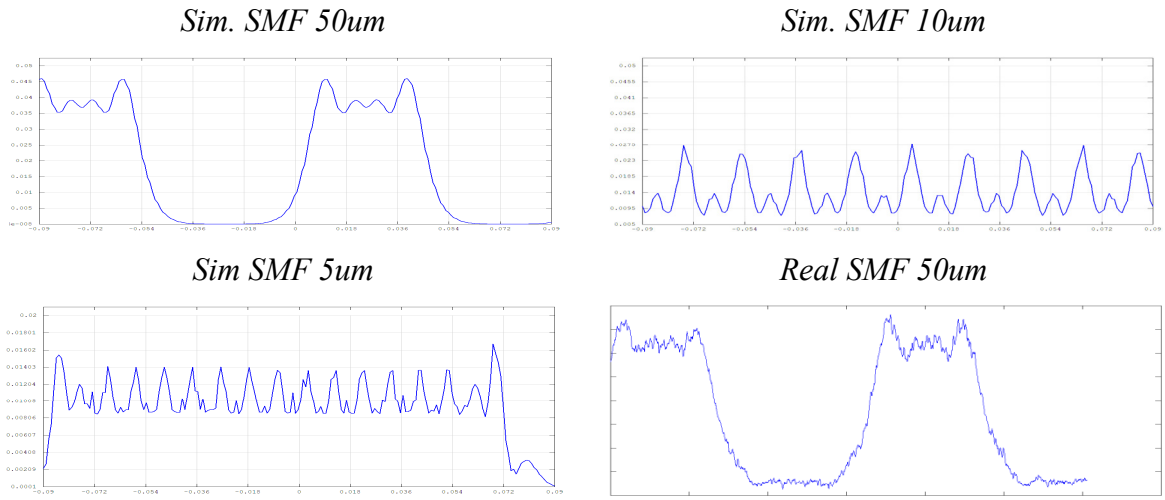

Figure 6.12: *RF SMF simulations with different patterns and practical verification*

The results of the analysis of the reflection approach are synthesized in the table 6.3. This configuration allows much better coupling efficiency than the transmission approach, and the detection of slits in the order of 10um is guaranteed with the usage of SMF.

	Fibre type	Disk/Fibre	Distance Tol.	Tilt Tol.	Misalilgnment Tol.	Free Space Loss	Component Loss	Received signal	Detection
Reflection	MMF	250 um	100 um	10.2 deg	--	8 dB	6.6 dB	3.46%	>62.5um
	SMF	250 um	50 um	2.5 deg	--	15 dB	6.6 dB	0.69%	>10um

Table 6.3: *Results synthesis of the reflection approach analysis*

6.1.3 Vacuum Focuser

A focuser was applied to the reflection approach in order to obtain a much better coupling efficiency, improve the tolerances reached by each kind of fiber and improve the detection capability, reaching as small focused spot sizes as possible (see Fig 6.13). For this, the assembly explained in the section 5.5.2 was used. This focuser assembly is vacuum and high temperature compatible, according to the characteristics of the optics (lens 352440) and its material ECO550 is able to cope up with temperatures up to 364^{o}. The housing chosen is all made of aluminum, where no plastic pieces or glues are used and make it suitable for vacuum. The lens 352440 characteristics makes it very flexible and it can be used in different configurations, allowing the implementation of an optical system 1:1, 1:2 and 1:1/2 by selecting different lens orientation and fiber/lens (D1) and lens/disc (D2) distances. With these configurations the focused spot size could be as big as the size of the core of the fiber, two times bigger or half the core size, improving this way the detection capability of the system.

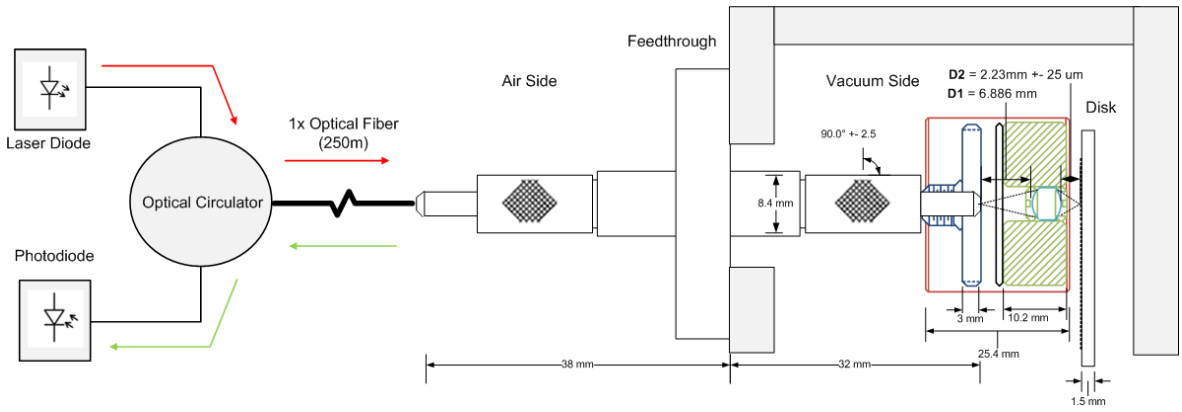

Figure 6.13: *Vacuum focuser approach schematic*

Zemax simulations were performed to obtain the suitable D1 and D2 distances for the different expected spot sizes. The optimization tool was used with the aim of obtaining as best coupling efficiency as possible with the smallest spot size possible at 1310nm. These simulations were performed with the models of MMF and SMF, obtaining this way spots of 62.5 and 32um for MMF and 20, 10 and 4.5um for SMF. The resulting distances are shown in the table 6.4. To experimentally verify the focused spot sizes of the MMF; a Spiricon CCD camera system was used as shown in the Fig 6.14. For SMF, focused spots were too small to be visible with this camera since its pitch wasn´t small enough. Experimental measurements directly on the disc have confirmed the focused spots size to be in the order of the simulations.

Focuser Combinations			
Fiber	Spot Size	D1 (mm)	D2 (mm)
MMF	62.5	4.35	3.806
	32	6.651	2.678
SMF	20	2.618	6.886
	10	4	4.15
	4.5	6.886	2.618

Table 6.4: *Vacuum Focuser distances combinations*

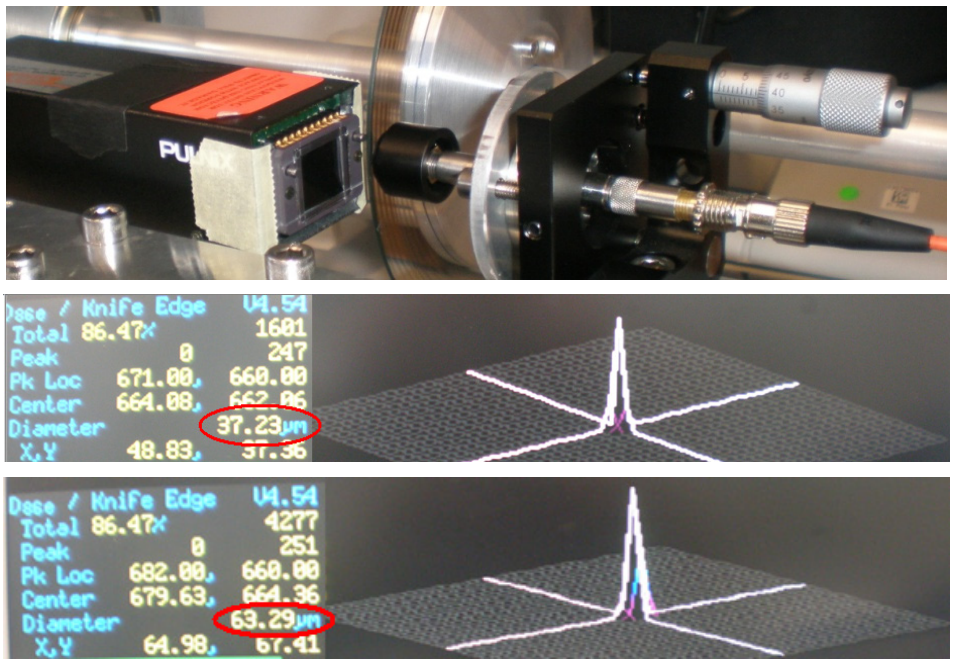

Figure 6.14: *Spot sizes obtained with MMF, experimentally validated with a Spiricon system.*

From the coupling efficiency point of view, this configuration is the most suitable. The simulations performed, considering the absorption of the materials and the lens coating for the wavelength range between 1050-1620nm, shown coupling efficiencies in the order of 70% with all the possible lens configurations. This is an improvement of factor 10 of the energy coupled back in the fiber compared to the previous reflection approach without lens. This means that taking into account all the sources of loses in the system such as

circulator (-1.65dB), 60% chrome reflection (-2.22dB), 3 connections (3 x -0.3= -0.9dB) and lens absorption (-1.54dB), the theoretical power loss of the system is in the order of -6.3dB. A theoretical percentage around 25% of the laser optical power is coupled back in the receiver after interacting with the disc.

To have a complete model of the loses of this lens system, practical verification of power coupling was performed by measuring the power of the laser diode (0.91dBm) and the signal received after reflections on the disc in the case of SMF (-7.5 dBm) and MMF (-4.77 dBm). These experimental results are showing that the losses of the complete system for SMF are 8.41dB, meaning that a 14% of the signal form the laser is received in the photodiode. For the MMF the loss of the complete system are around 6.4 dB, a 20% of the optical power. These results are matching with the Zemax modelization minus difference due to possible imperfections in the focuser assembly and misalignments fibre/lens.

In terms of tolerance, this assembly was also analyzed and the results are shown on Fig.6.15. The simulated coupling efficiency versus variation of the focal distance (D2), for +-100um in each case, shows in red the two focused spots obtained with MMF whereas the green lines the SMF's. When the spot is reduced, the tendency is a reduction in the disc/lens distance tolerance. If the tolerance is too small, the imperfections of the disc or the testbench analyzed in section 5.7 will have a remarkable negative effect in the detected signal, resulting by a reduction of amplitude (repeatable amplitude modulation as the disk turns). This chart has been normalized in order to be able to compare all the different combinations. By defining as tolerance as the point where the signal is reduced by half its maximal value; the D2 tolerance for MMF 62.5µm spot is around ±90µm, for the MMF 32µm spot is around ±28µm, in the case of the SMF the 20µm is around ±150µm which is the biggest tolerance observed.The SMF 10µm spot has around ±60µm and finally the smaller spot size, SMF 4.5µm spot, has the smaller tolerance, in the order of ±20µm.

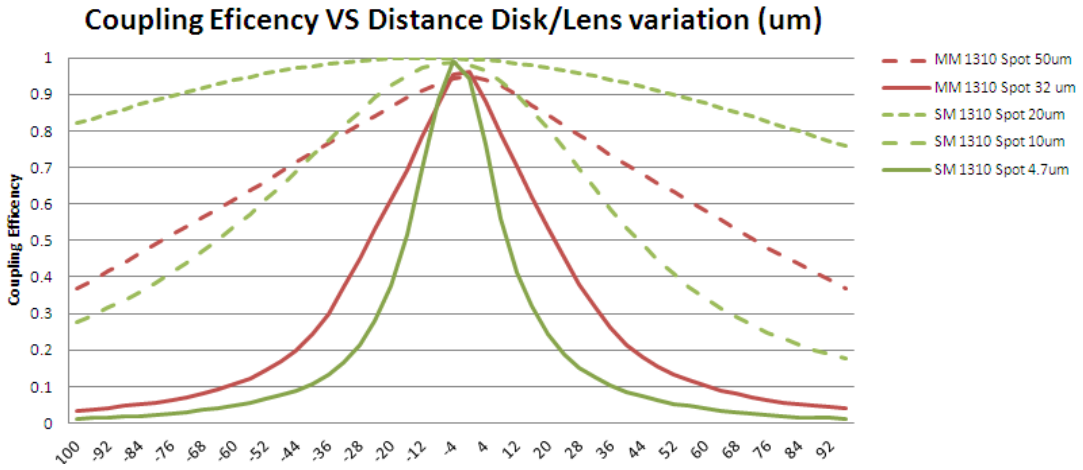

Figure 6.15: *D2 tolerance analysis of the different focuser combinations*.

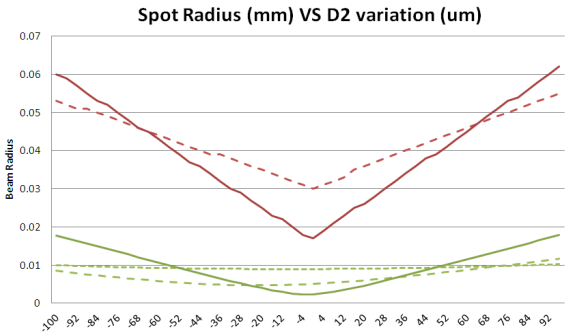

Figure 6.16: *Spot radius VS D2 variation*

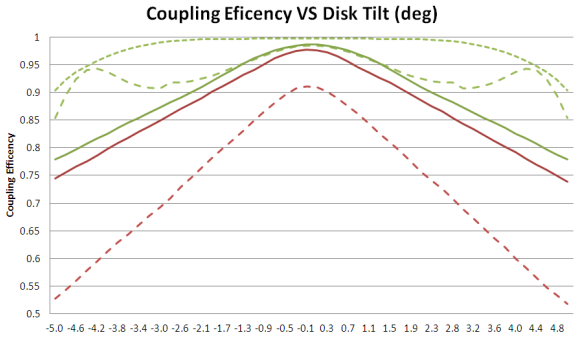

Figure 6.17: *Disc tilt tolerance analysis*

The tilt analysis was performed by simulating a disc tilt between -5° and +5° to check if this effect was an important factor to take into account. The simulation in Fig. 6.17 is showing that for any spot size with this focuser, the tilt tolerance is bigger than 5°.The same tendency as in the D2 tolerance is observed, when the spot is reduced, the tilt tolerance is also reduced. Fig. 6.16 shows also the spot radius versus D2 variation, which is basically the light path at the focal point. For the MMF, geometrical optics has been used and the radius variation with respect the focal point is sharp, whereas for the SMF simulations the Gaussian optics has been used and the variation is much smoother due the Gaussian waist of the light.

Regarding the detection capability of each spot size, the best signal is obtained with slits having the same width as the spot diameter. It is still possible to reach a detection capability with half the size of the spot, but with a loss of 3dB in the dynamic range and sinusoid signals. Obviously, if the slits are much bigger than the focused spot size, the

signals obtained are square with a good coupling efficiency. The Fig 6.18 shows the measured signals obtained for both fibres with slits of 50µm width.

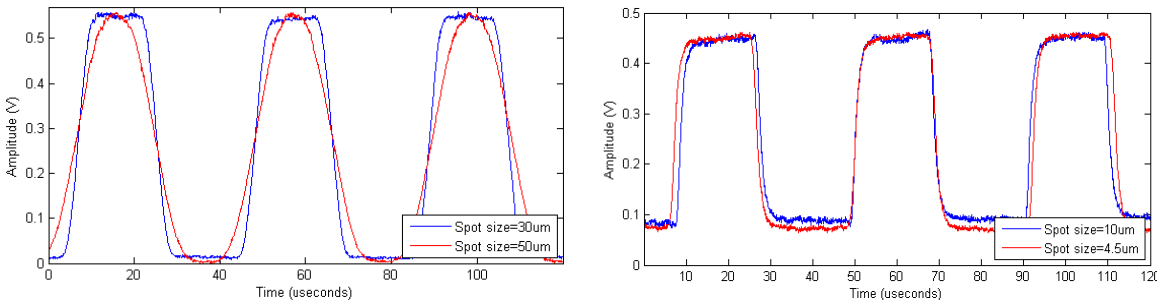

Figure 6.18: *Experimental measurements of different spot sizes for MMF(left) and SMF (Right)*

Measurements were taken with the testbench and a Lecroy oscilloscope to obtain a complete revolution of the disc and verify if the relative movement of the disc in the axial direction would affect the signal, and compare it to the simulations. Figure 6.19 shows a complete revolution with different spot sizes and fibers types. As it was predicted, the configurations more sensitive to imperfections are the MMF 30µm spot (up red), where the disc movement in the order of 25µm reduces the signal almost to 75% of its mean value. Also in agreement with the simulations the SMF 5µm spot (red down) shown an important attenuation due to this movement (slow envelope at the beginning of the turn). In some cases a quick modulation envelope appears (always in SMF and MMF and only at 1310nm), this effect will be analyzed in the section 6.3.

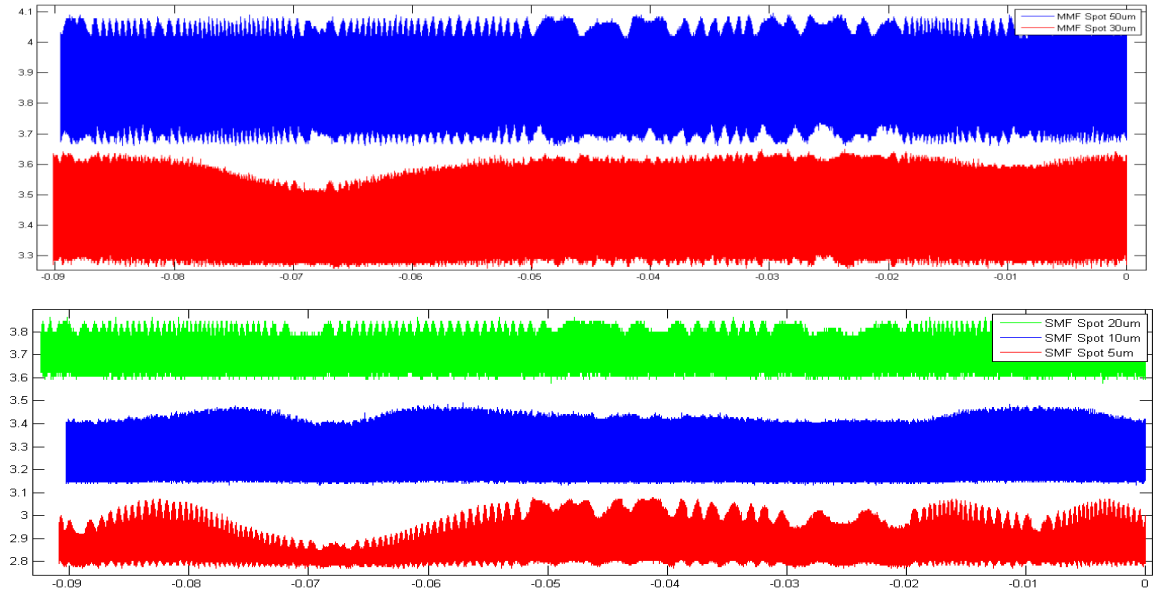

Figure 6.19: *Measured signal using the focusing approach for a complete disc revolution for MMF 62.5um spot (up blue), MMF 32um spot (up red), SMF 20um spot (down green), SMF 10um spot (down blue) and SMF5um spot (down red)*

The mechanical tolerances studied for any of these configurations of vacuum focuser can be reached on the final system, according to the mechanical team. The high performance obtained in the coupling efficiency as well as the possibility of having a resolution around 5um makes this approach is the most promising and suitable for the design of the optical position sensor. The table 6.5 summarizes the conclusions extracted from the study of this approach.

	Fibre type	Disk/Lens	Distance Tol.	Tilt Tol.	Misalilgnment Tol.	Free Space Loss	Component Loss	Received signal	Detection
Vacuum Focuser	MMF (62.5um)	3.806 mm	95 um	5 deg	--	0.1 dB	6.3 dB	22.90%	62.5 - 30 um
	MMF (32 um)	2.678 mm	30 um	10 deg	--	0.1 dB	6.3 dB	22.90%	30 - 15 um
	SMF (20um)	6.886 mm	145 um	8 deg	--	6.31 dB	6.3 dB	5.11%	20 - 10 um
	SMF (10um)	4.15 mm	70 um	7 deg	--	2.11 dB	6.3 dB	14.42%	10 - 5 um
	SMF (5um)	2.618 mm	25 um	10 deg	--	2.11 dB	6.3 dB	14.42%	5 - 2.5 um

Table 6.5: *Conclusions in the vacuum focuser approach*

Considering that a spot of 10um with SMF and a lens system 1:1 provides a quite good tolerance, in tilt as well as in D2 tolerance, a commercial solution with these characteristics was found. The commercial focuser 60FC-4-A4-03 with the micro focus optics 5M-A54.0-03-S from Schafter + Kirchhoff was experimentally and validated as a possible suitable standard solution (see Fig 6.20). This focuser whose mechanics are made of nickel silver and its optics made of CO550 (Similar to ECO550) is UHV compatible and the lens system is able to work until temperatures of 330°. According to the provider, the whole assembly would be suitable for our environment.

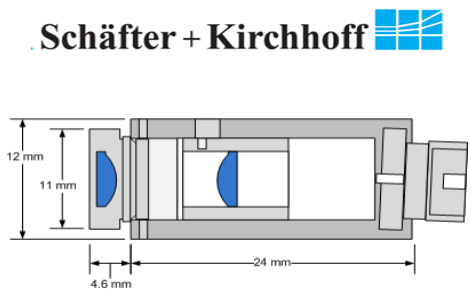

Figure 6.20: *Commercial focuser*

In the experiments performed in the laboratory as shown in the following table (table 6.6), similar results to the previous focuser from Thorlabs were obtained in terms of tolerance, Even a better coupling efficiency was obtained due to the compactness of this device and high precision alignment. The lens adjustments and fixations are done with high precision screws, which makes easier to calibrate. It is possible then, to assume that this focuser system is the optimal solution studied in terms of coupling efficiency and previously listed parameters.

	Fibre type	Disk/Lens	Distance Tol.	Tilt Tol.	Misalilgnment Tol.	Free Space Loss	Component Loss	Received signal	Detection
Commercial Focuser	SMF (10um)	2 mm	70 um		--	1 dB	6.3 dB	18.60%	10 - 5 um

Table 6.6: *Measurements and tests done with the commercial focuser.*

6.1.4 External Focuser

The best optical system candidate to design this sensor is based in the usage of aspheric lenses in order to improve the coupling efficiency and the detection capability. Therefore, a very precise positioning system must be implemented to place the lens at the exact focal distance with a tolerance between 100µm and 25µm, depending on the spot size. Considering the installation of a lens system may be very complex, fragile, and impossible to adjust after installation. An external focuser approach will be studied to place the optical system outside of the vacuum tank, focusing the beam on the disc through an optical viewport (see Fig. 6.21). The Base line solution is shown in Fig 6.21. The advantage of this solution is that external calibration can be performed by mean of linear stages.

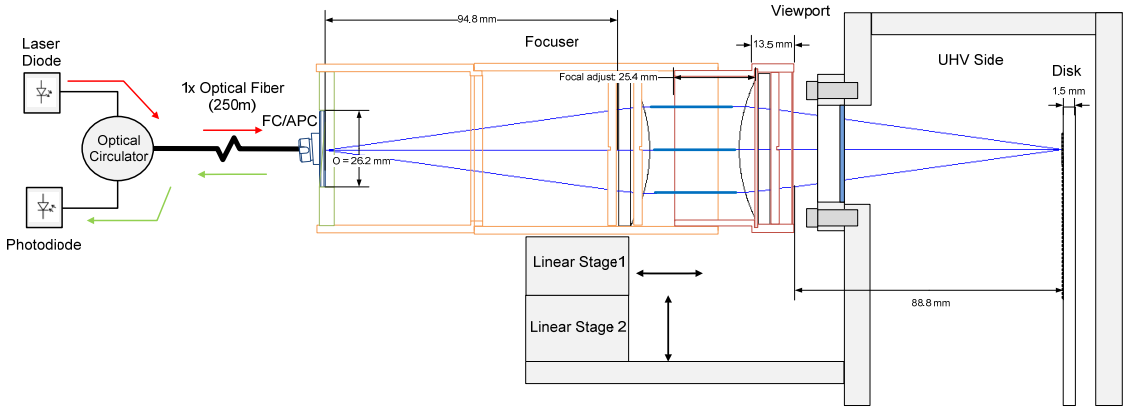

Figure 6.21: *External focuser assembly schematic*

Section 5.5.2 introduces in detail the lenses that have been selected for this approach based on the various constraints. By playing with the combinations of these lenses and the distances D1 and D2, different magnification factors can be obtained. According to the Zemax simulations, the combinations of the lens AL2550-C, AL50100-C and AL75150-C from "Thorlabs" allow to different spot sizes from 120 um to 6.86um, with a coupling efficiency similar to the vacuum focusers. The table 6.7 shows the lens positioning distances obtained with the Zemax optimization tool for different spot sizes.

External Focuser Combinations				
Combination	Fibre	Spot (um)	D1 (mm)	D2 (mm)
AL2550-C & AL50100-C	MM	125	46.767	95.37
AL50100-C & AL50100-C	MM	62.5	94.85	95.357
AL2550-C & AL50100-C	SM	20	46.767	95.367
AL50100-C & AL50100-C	SM	10	94.856	95.367
AL75150-C & AL50100-C	SM	6.86	149.167	92.532

Table 6.7: *External focuser distances combinations*

As in the previous approaches a tolerance analysis has been carried out through Zemax simulations and followed by an experimental verification. The charts presented in Fig.6.22 are showing the outcome for the D2 tolerance, the viewport tilt tolerance, the disc tilt tolerance and the light radius at the beam the focal point. The color code represents the different lens combinations shown in the table 6.7. The red ones for the 20µm spot size, the blue ones for the 10 µm spot and finally the green one for the 6.86 µm spot. The simulations are showing only the SMF configurations, since the MMF tolerances are much more relaxed.

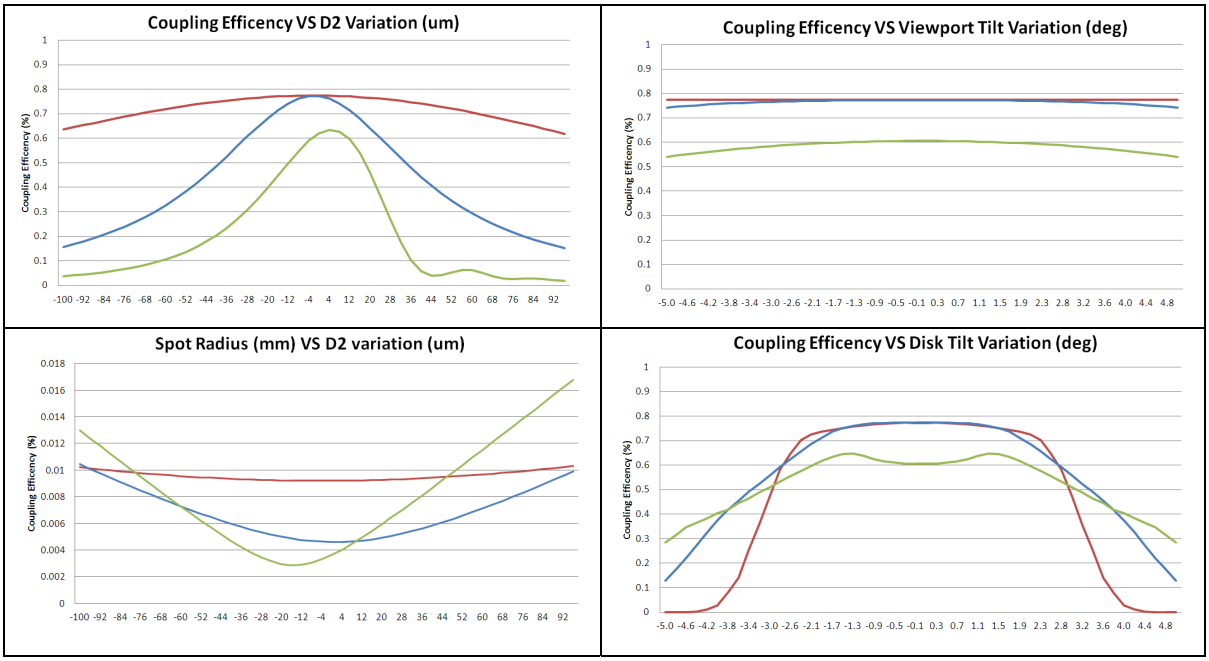

Figure 6.22: *External focusers tolerance analysis.*

The chart of the D2 tolerance (up left), shows as expected, that the smaller the spot size is, the smaller the tolerance in this distance is. With ±200µm of tolerance for the 20µm spot size, it goes down to ±50µm for the 10µm spot and ±32µm for the 6.86µm spot. These values are quite similar to the previous vacuum focusers. The tilt of the viewport with respect to the axis of the optical system was also studied, to know the influence with the coupling efficiency from -5 to +5 degrees (see Fig.6.22 up right chart). It was found that this range of misalignment had almost not influence as long as the light is reflected at the disc. Regarding the disc tilt with respect to the focuser, the simulations performed (down right) are showing that the 20µm spot size is the more restrictive, having a tolerance of ±3.2 degrees, then the 10µm spot has 4 degrees and for the 6.8µm, there is a maximum tolerance of 4.6 degrees. Finally the chart located in the down left sector is showing the

appearance of the Gaussian beam waist radius versus the D2. As the spot goes smaller, the Gaussian waist changes quicker with the distance.

Following these simulations, experimental verification with two focusers (10µm spot and 20µm spot) were performed to verify the power coupling, angular tilt and D2 tolerance. The fixed loses of the system it was assumed to be exactly the same as for the vacuum focuser. The global loses of 6.3dB was taken for the circulator, Cr reflectivity, lens absorption and connectors. The MMF approach and SMF 6.86µm spot size configurations couldn't be experimentally validated since the lens AL75150 and the fiber connector for MMF were not available. The table bellow summarizes the experimental values obtained.

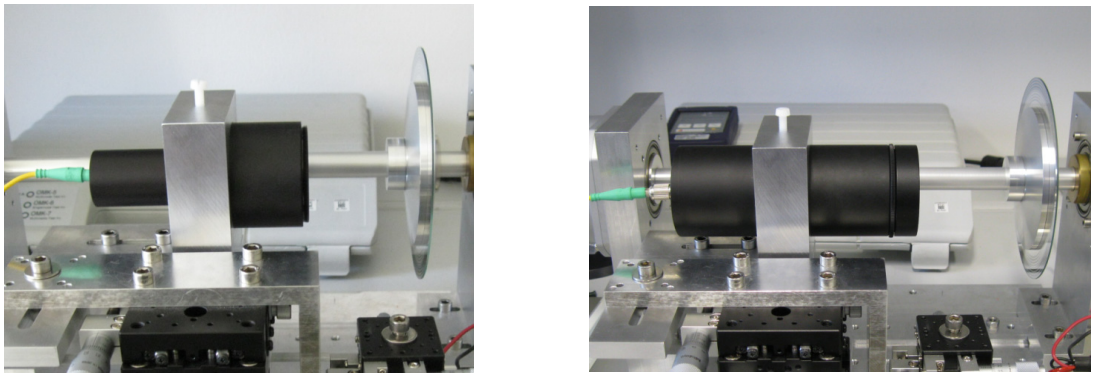

Figure 6.23: *External focusers configurations for 20µm spot size (left) and 10µm spot size (right)*

	Fibre type	Disk/Lens	Distance Tol.	Tilt Tol.	Misalilgnment Tol.	Free Space Loss	Component Loss	Received signal	Detection
External Focuser	MMF (125um)	95.37 mm	800 um	3 deg	--	--	--	--	125 - 62.5 um
	MMF (62.5)	95.357 mm	300 um	5 deg	--	--	--	--	62.5 - 30 um
	SMF (20um)	95.367 mm	200 um	3.2 deg	--	4 dB	6.3 dB	9.33%	20 - 10um
	SMF (10um)	95.367 mm	50 um	4 deg	--	3.48 dB	6.3 dB	10.51%	10-5 um
	SMF (6.86um)	92.532 mm	32 um	4.6 deg	--	--	--	--	5 - 2.5 um

Table 6.8: *Experimental results for the external focusers with SMF 10µm and 20µm spot size.*

As shown in table 6.8, the coupling efficiency is a bit lower than the one obtained with the vacuum focusers (around 10%). Due to the components big size, certain misalignment between lens/fibre as well as higher lens absorption could be the responsible of this difference. These experimentations confirm the Zemax modelisation of the Distance D2 (disc/lens) tolerance with ±200µm for 20µm spot size system, and ±50 µm for the 10µm spot size system.

Finally some samples were recorded with these two combinations in order to check the shape of the pulses and develop the processing algorithms. As shown in Fig 6.24, the shape of the pulses with the 10µm spot size starts showing some Fresnel diffraction (ringing in

the edges), whereas the 20µm spot size shows smoother transitions and cleaner signal. For both combinations the pulses uniformity and correct detection has been checked.

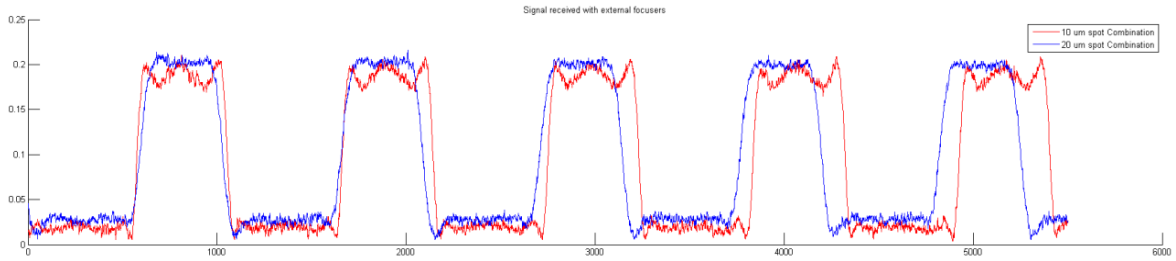

Figure 6.24: *Signal recorded with the 10 um and 20um external focusers.*

To conclude, this approach has been validated and the tolerances and the coupling efficiencies found to be similar to the vacuum focusers approach. This solution could be taken as a back-up solution in case the vacuum focusers where not found suitable for the environmental conditions of the accelerators, or as a provisional substitutive device in case maintenance or if where needed on the changes of the vacuum part of the design.

6.2 Avoiding Fabri-Perot Interferometer

An important problem was identified when using SMF in reflection approaches. In spite of having shown the expected good tolerances in the distance fiber/disc or lens/disc, the system was extremely sensitive to vibrations. It was also observed that while the disc was turning, and due to the imperfections identified in the section 5.7 of the testbench, the small changes of distance between disc/fiber or disc/lens, produced a very quick modulation in the signal, that in certain cases was constructive and in others the signal was reduced almost to 0, avoiding this way a correct edges detection, this effect can be seen in the Fig. 6.25.

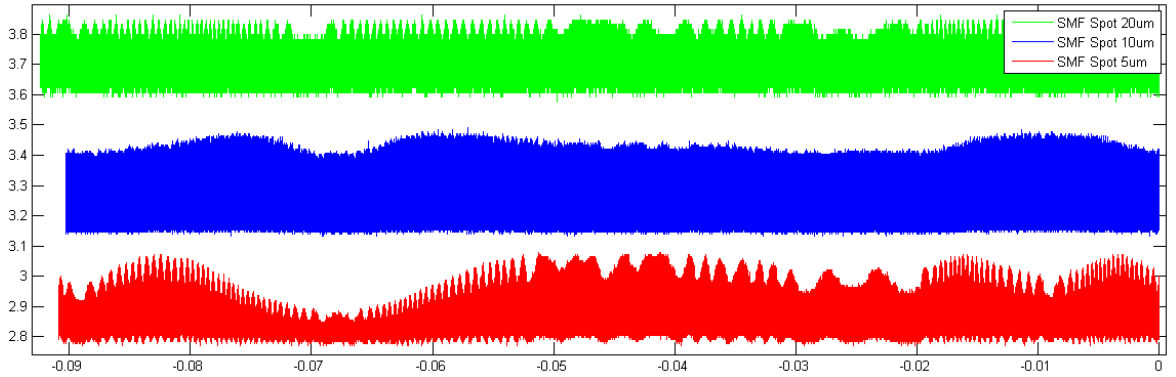

Figure 6.25: *Signal detected in a complete turn with SMF PC connectors and vacuum focuser, 20um spot (green), 10 spot (blue) and 5um spot (Red) configurations.*

The Fig 6.26 shows the signal during a complete turn of the disc using SMF and focuser in three different configurations 20, 10 and 5 um focused spot. Slow variations that can be seen in the signal when using the 10 and 5 um spots are due to the relative movement of the disc in the order of 25um. These relative movements are degrading the coupling efficiency, although, the quick modulation, more clearly visible on the smallest spot size (red) was not taken into account in the previous studies.

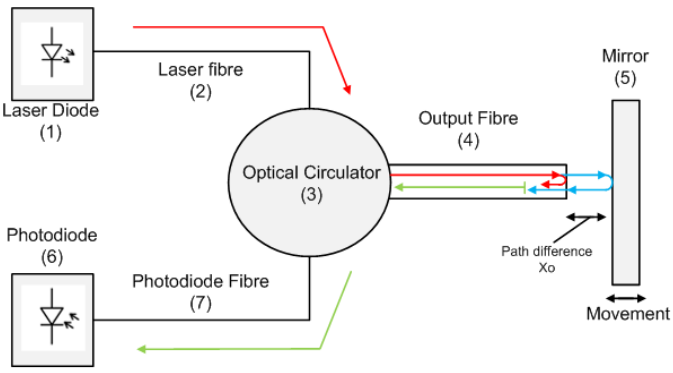

Figure 6.26: *Typical configuration for a Fabri-Perot Interferometer*

After careful consideration, the reason of these phenomena is that the assembly acts as an optical fiber Fabri-Perot interferometer, used to measure movements in the order of the laser wavelengh. In this interferometer, the interference occurs at the partially reflecting end face surface of the fiber. Considering our assembly represented in Fig. 6.26, the radiation from the laser diode (1) coupled in the fiber (2), goes through the optical circulator (3) to the fiber (4). Then, one part of radiation is reflected from the end face of the fiber (4) (due Fresnel reflection in the interface silica/air, shown in red), other part is transmitted into the air, reflected in the mirror (5) (shown in blue) and coupled back in the fiber 4. The optical beam reflected from the end face of the fiber 4 interferes with the beam reflected from the mirror. As a result, the intensity of the optical radiation (in green) at photodetector (6) is periodically changed depending on the distance x_0 between the fiber and mirror as follows:

$$I = 2I_0\left(1 + \cos\left(\frac{4\pi}{\lambda}x_0 + \varphi_o\right)\right) \qquad (6.1)$$

The equation 6.1 describes that displacements in the order or half of the wavelength (1310/2= 655nm) changes the part-length difference of the interfering rays by 2π,explaining the high vibration sensibility of this sensor. Moreover, since the laser diodes are not perfectly monochromatic, there are no interferences with distances in steps of the coherence length, such as l_c, $2l_c$, 3lc…etc. In general the spectrum is equal to Δλ=3-5nm; equation 6.2 explains the relationship between Δλ and l_c.

$$l_c = {\lambda^2}/{\Delta\lambda} \quad , \quad \varepsilon = \pi\left({l}/{l_c}\right) \qquad (6.2)$$

Finally equation 6.3 represents the behavior of a Fabri-Perot interferometer, where $I_1=R_1I_0$ is the intensity of the light reflected from the end face surface of the fiber and $I_2=(1\text{-}R_1)^2RI_0$ is the intensity of the light reflected from an external mirror and returned back into the fiber. Io is the intensity of the laser diode radiation, R1 is the reflectivity of the end face of the fiber and R is the reflectivity of an external mirror.

$$I = I_0\left\{R_1 + (1-R_1)^2R + 2(1-R_1)\sqrt{RR_1}\,\frac{\sin\varepsilon}{\varepsilon}\cos\left(4\pi\frac{x_0}{\lambda}\right)\right\} \qquad (6.3)$$

In order to verify the hypothesis that this phenomena was the cause of this quick modulation in the signal, some simulations where done by using the equation 6.3 with the known parameters of the system.

Firstly, the signal from the reflection approach was acquired with a SMF placed at 200um from the surface; the signal considered was from a section of the disc where the known distance variation disc/fiber was around known to be 2.5 um (see Fig. 6.28 up). Then, two simulations were performed for Phisical Contact (PC) and Angular Physical Contact (APC) fibers taking into account two different kind of mirrors, the first mirror considered models the chrome surface (Fig. 6.28 blue middle and down) and second one the borofloat glass (Fig. 6.28 red middle and down). The first simulation, in Fig 6.28 centre, models the usage of a PC fiber (the one that has been used in Fig. 6.28 up) which is characterized for a Fresnel back-reflections in the order of -17dB. The second simulation, Fig. 6.28 down, considers the usage of APC. It is known that APC fibers avoid back reflections inside the fiber, by means of a angled (8^o) ending reflecting the light out of the fiber in a way that there is no propagated light through the fiber again (see Fig 6.27), keeping at the same time the same insertion loss as PC fibers, the measured Fresnel back-reflections in an APC fiber are around -40dB. The parameters used for the simulations are summarized in the next table.

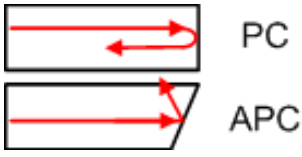

Figure 6.27: *PC/APC fiber comparison*

	Distance	Variation	Io	Cr. Reflexibility	Bf. Reflectivity	Coupling Eff.	Fibre Type	Fresnell Reflections	
Simulation 1	200um	2.5um	1	60%	6%	90%	PC	-17dB	2%
Simulation 2	200um	2.5um	1	60%	6%	90%	APC	-40dB	0.01%

Table 6.9: *Simulation parameters used in Matlab to model the system with PC/APC fibers*

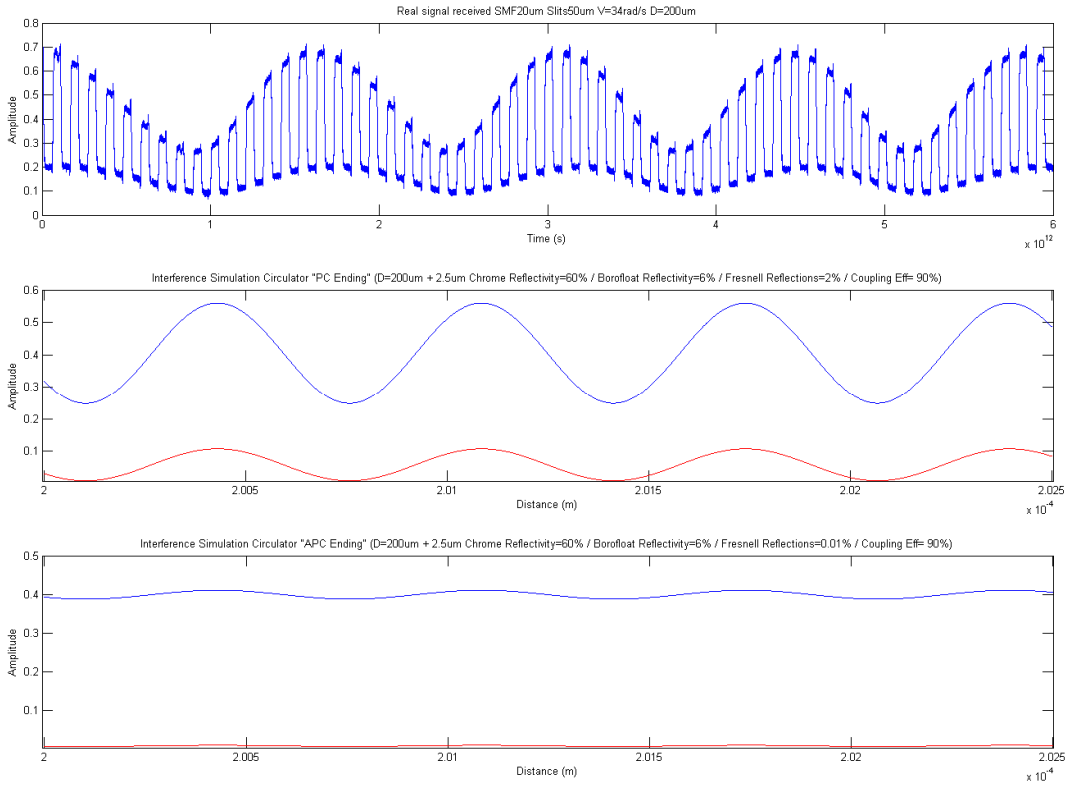

Figure 6.28: *Reflection signal recorded by a SMF when turning disc (up), System simulation considering PC fiber (centre), System simulation considering APC fiber ending (down).*

As it can be seen in the Fig 6.28 (up), the behavior of the envelope of the slits pattern has been accurately modelised with the equation 6.3 in figure 6.28 (centre). This concludes that the source of the modulation (in the chrome reflections as well as in the borofloat reflections) is interferences due to the PC ending of the fiber. It is also shown that 2% (-17dB) of back-reflections for the PC ending are able to affect our signal of interest by changing its amplitude, in a constructive way but also destructive, justifying the importance of avoiding this type of disturbances. At the bottom of figure 6.28, the is considering an APC fiber that provides 0.01% (-40dB) of back-reflections, resulting by a diminution of the effect in the order of 200 times. The perturbating modulation has been practically avoided by changing the characteristics of the end of the fiber.

To confirm these results, an APC fiber setup was build and the signal obtained was compared with the PC ending version using the same the lens system. The figure 6.29 shows the 2 setups and the large improvement of the signal shape when the APC fibre type was introcuded. The power of the laser, the distances used in the focuser and the zone of the disc are exactly the same in both cases.

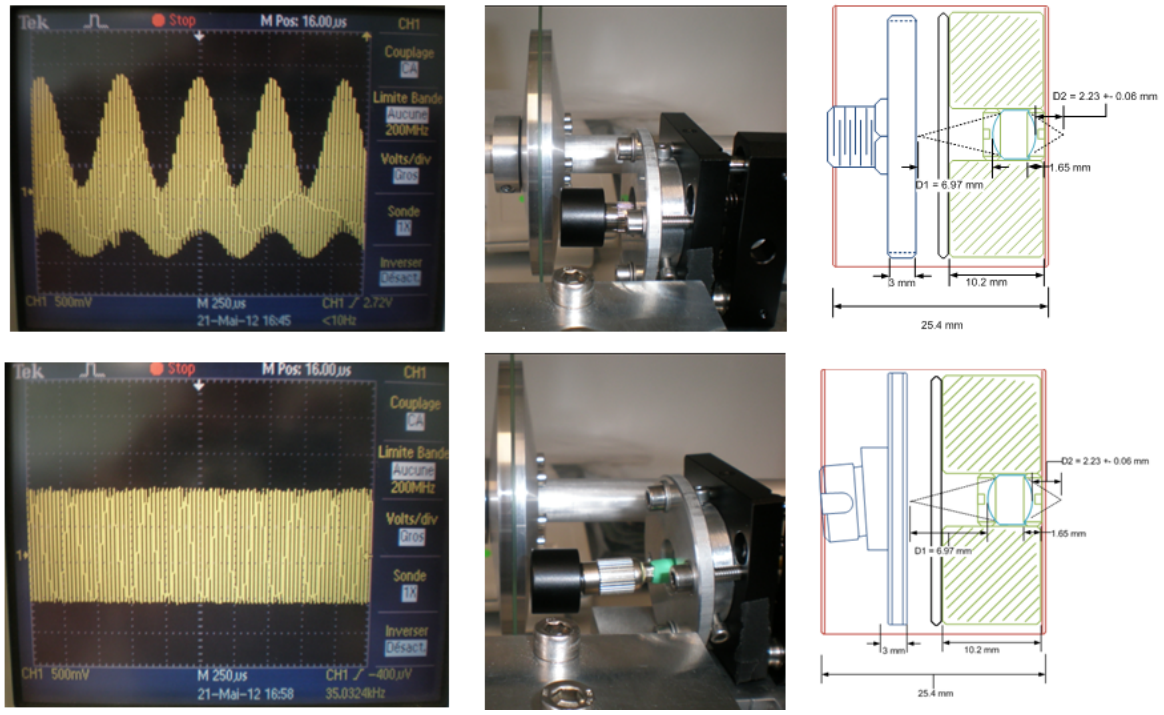

Figure 6.29: *Experimental justification of APC usage, Upper row: PC SMF. Down row: APC SMF*

Some extra measurements were taken in order to verify that both systems had about the same coupling efficiency, visible in table 6.10. Complete turns were also recorded for the different lens configurations in order to verify that the effect was completely avoided by using APC ending fibers (see Fig. 6.30). These measurements emphasize the usage of APC fiber ending and highlight the importance of avoiding the back reflections in a laser system as ours. The only constrain of this solution is that the FC/APC focuser connector is tilted in order to compensate the tilt of the fiber, so care must be taken to place the lens parallel with the disc.

	Fiber Back Reflections	Cr Signal	Bf. Signal
PC	-16dBm (2.5%)	-6dBm (25%)	-13dBm (5%)
APC	-44.57dBm (0.004%)	-7dBm (20%)	-19.5dBm (1.2%)

Table 6.10: *Measurements taken in both cases*

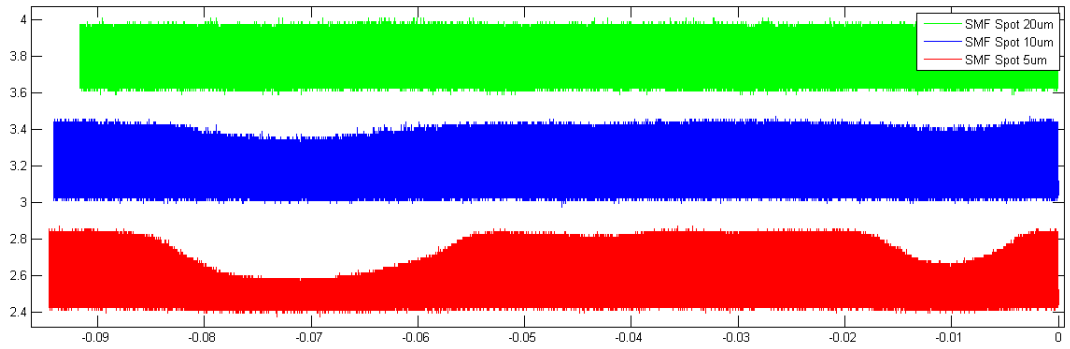

Figure 6.30: Recorded signals using APC connector for different spot sizes, highlighting the vanishment of the perturbative interference produced by back reflections.

6.3 Optical power balance

An important issue in a sensor or optical link design is to evaluate and design the power budget of the system. The first step to be done is to measure and characterize each component of the link and express its standard loses in dB. In our case we have measured each component separately for the wavelengths 850 and 1310 nm. This takes into account that the components for 850nm are made of MMF whereas the components for 1310 are only for SMF. As shown in the table 6.11, each laser diode and photodiode has certain maximal power, saturation point and minimal sensitivity. For the design, the power received after all the components and the interaction with the disc must be still bigger than the photodiode sensitivity. We have fixed a minimum signal of -25dBm in order to have a good signal to noise ratio with the used components.

Component loss analysis			
Element	Wavelengh		Units
	850	1310	nm
Laser Model	KLD085VC	BOB1310FP	
Laser Power	1.59	4	dBm
Photodiode Model	POF562A	PTINS155ST83-n-O	
Photodiode Sensibility	-41	-36	dBm
Photodiode Saturation	-7	-3	dBm
Circulator	1.65	1.65	dB
Connections	0.3	0.3	dB
MMF Feedthrough	2.9	2.21	dB
SMF Feedthrough	--	--	dB
SMF Cable	1	1	dB/Km
MMF Cable	3.5	1.5	dB/Km
Cr. Reflectivity	2.22	2.22	dB

Table 6.11: *Component loss analysis*

The table 6.12 compares all the approaches analyzed in this chapter in terms of tolerance, coupling efficiency, detection capability and loss margin until before -25dBm using the maximal power of its laser diode in each case. For the MMF approaches, the 850nm laser diode and photodiode were used whereas for the SMF the 1310nm couple was used. The green highlighted rows are what it has been considered a good compromise. The usage of SMF with a spot of 10 um guaranties a good performance and detection capability, taking into account its relative large tolerances and good coupling efficiency. It is possible to see that the systems without lenses have a very low loses margin to -25dB. Assuming the aging of the components and the RIA of the fibers, these approaches could be limited. On the other hand, the focusers are showing very good performance and a large margin in terms of loses, having enough power to compensate a possible darkening of the fibres. This final table drives us to conclude that it's possible to use both vacuum focusers for 10um, and the external focuser for 10um as a backup solution.

											Balance MMF 850nm 1.59dBm Balance SMF 1310nm 4dBm	
	Fibre type	Disk/Fibre	Distance Tol.	Tilt Tol.	Misalilgnment Tol.	Free Space Loss	Component Loss	Total Loses	Received signal	Detection	Received power	Margin to -25 dBm
Transmission	MMF	250 um	250 um	13 deg	350 um	18 dB	5 dB	23 dB	0.50%	>62.5um	-21.41 dBm	3.59 dB
	SMF	250 um	250 um	2.5 deg	50 um	22 dB	5 dB	27 dB	0.19%	>10um	-23 dBm	2 dB
Reflection	MMF	250 um	100 um	10.2 deg	--	8 dB	6.6 dB	14.6 dB	3.46%	>62.5um	-13.01 dBm	11.99 dB
	SMF	250 um	50 um	2.5 deg	--	15 dB	6.6 dB	21.6 dB	0.69%	>10um	-17.6 dBm	7.4 dB
Vacuum Focuser	MMF (62.5um)	3.806 mm	95 um	5 deg	--	0.1 dB	6.3 dB	6.4 dB	22.90%	62.5 - 30 um	-4.81 dBm	20.19 dB
	MMF (32 um)	2.678 mm	30 um	10 deg	--	0.1 dB	6.3 dB	6.4 dB	22.90%	30 - 15 um	-4.81 dBm	20.19 dB
	SMF (20um)	6.886 mm	145 um	8 deg	--	6.31 dB	6.3 dB	12.62 dB	5.11%	20 - 10 um	-8.62 dBm	16.38 dB
	SMF (10um)	4.15 mm	70 um	7 deg	--	2.11 dB	6.3 dB	8.41 dB	14.42%	10 - 5 um	-4.41 dBm	20.59 dB
	SMF (5um)	2.618 mm	25 um	10 deg	--	2.11 dB	6.3 dB	8.41 dB	14.42%	5 - 2.5 um	-4.41 dBm	20.59 dB
Commercial Focuser	SMF (10um)	2.39 mm	70 um		--	1 dB	6.3 dB	7.3 dB	18.60%	10 - 5 um	-3.3 dBm	21.7 dB
External Focuser	MMF (125um)	95.37 mm	800 um	3 deg	--	--	--	--	--	125 - 62.5 um	--	--
	MMF (62.5)	95.357 mm	300 um	5 deg	--	--	--	--	--	62.5 - 30 um	--	--
	SMF (20um)	95.367 mm	200 um	3.2 deg	--	4 dB	6.3 dB	10.3 dB	9.33%	20 - 10um	-6.3 dBm	18.7 dB
	SMF (10um)	95.367 mm	50 um	4 deg	--	3.48 dB	6.3 dB	9.78 dB	10.51%	10-5 um	-5.78 dBm	19.22 dB
	SMF (6.86um)	92.532 mm	32 um	4.6 deg	--	--	--	--	--	5 - 2.5 um	--	--

Table 6.12: *Options comparison and power balance for the 4 approaches of this chapter*

CHAPTER 7

Signal processing and system performance validation

This chapter address the topics related to the accuracy, resolution and repetitively of the system designed. The performances reached by the system will be compared against the initial specifications and with a commercial encoder system. Finally, the results of calibration with a commercial encoder system will be studied.

7.1 Experimental setup

This section aims to study and validate the usage of the designed fibre incremental encoder to be applied on the next generation WS wire position measurement system. Several detection methods will be considered and the 2 sides of the disc. The Chrome side which has the advantage to avoid the light crossing the glass material of the disc (avoiding the glass darkening influence due to radiation) and the glass side (as it's done in the CD/DVD systems). 9 turns of the disc will be recorded. The experimental setup used for the following measurements is based on the usage of the testbench presented in the section 5.7, which holds and rotates the disc, ideally at constant speed. Attached to the shaft the Heidenhain RON 225 encoder previously presented will be used as a reference for comparison and calibration. The setup used to scan the tracks of the disc will be based on the usage of the commercial focuser from Schafter + Kirchhoff provides the best coupling efficiency as seen in chapter 6.

7.1.1 Commercial encoder RON225

This device, according to the technical specifications by the company, reaches the expected performance of our system. The RON225 must be supplied by a voltage of 5V and has three output channels, Ref (reference mark for detecting the beginning of a rotation), ChA (which has 9000 pulses per rotation, giving 18000 edges) and ChB, which has the same characteristics as the ChA but with a displacement of 90 degrees electrical in order to perform a 4 Fold interpolation. The table 7.1 summarizes the initial characteristics of the encoder, and the Fig 7.2 shows the accuracy measurements provided by the company.

	Incremental signals	Line Pulses	Line Edges	Reference	Measuring step (°)	System accuracy (°)
RON 225	2	9000	18000	1	0.005	1.38E-03

Table 7.1: *Initial characteristics of the RON 225 encoder*

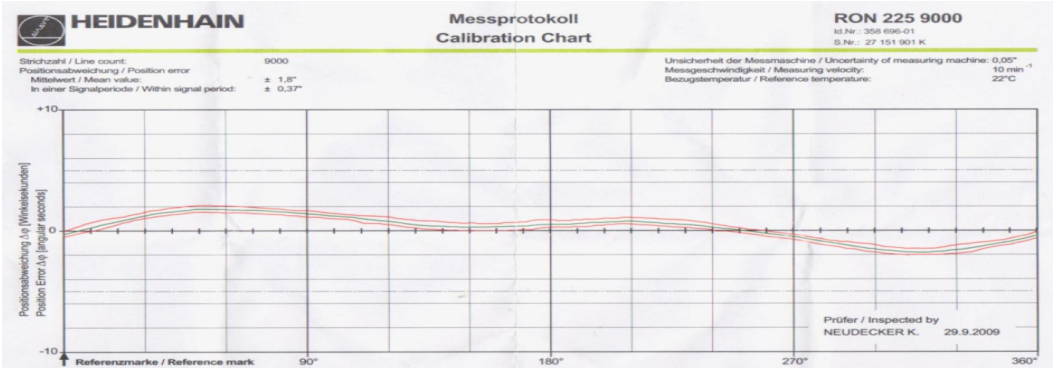

Figure 7.2*: Encoder RON225 accuracy measurements provided by Heidenhain*

7.1.2 Incremental fiber encoder configuration

To validate the design of this encoder, three different configurations were used: The 50µm track of the V1 disc, and the tracks 10µm and 5µm of the V2 disc. The Schafter focuser was used with SMF with a spot size in the order of 10um. With this spot size, it is the slit size and period which defines the shape of the recorded signals (square for 50um slits and sinusoid for 10um slits).

To be able to compare measurements of multiple rotations of the disc, the reference channel of the RON225 was used since the 2 encoders are fixed on the same shaft. The phase difference between the ref signal mark and the first edge of the disk is taken into account by the software to align the information of these 2 encoders. The measurements of the RON225 device are used as a reference to calibrate the disc and visualize which accuracy is reached by the system. The Fig 7.3 shows the test-bench, the electronics and the instruments used for performing these measurements.

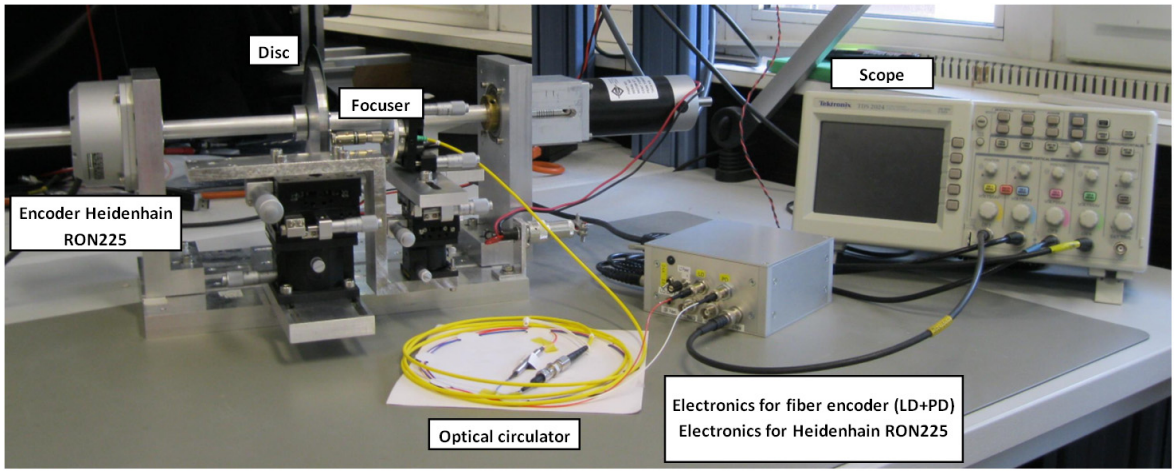

Figure 7.2: *Fiber incremental encoder set-up for performance validation*

7.2 Signal processing description

The signals from the fiber system and the commercial encoder channels were sampled and recorded with a Lecroy Osciloscope with a sampling frequency of 50MHz, later they were processed with Matlab. The sampling frequency was selected as the turning disk at the maximal speed, 200rad/s, would reach 130 KHz with the disk V1, whereas 1.6MHz for the V2 and 5um pattern. This would result by having 30 points per period at minimum. The Fig 7.3 shows the sampled raw signal from each encoder. Where we can see the 8 times difference in resolution between the 50um track of the V1 disc and ChA+ChB.

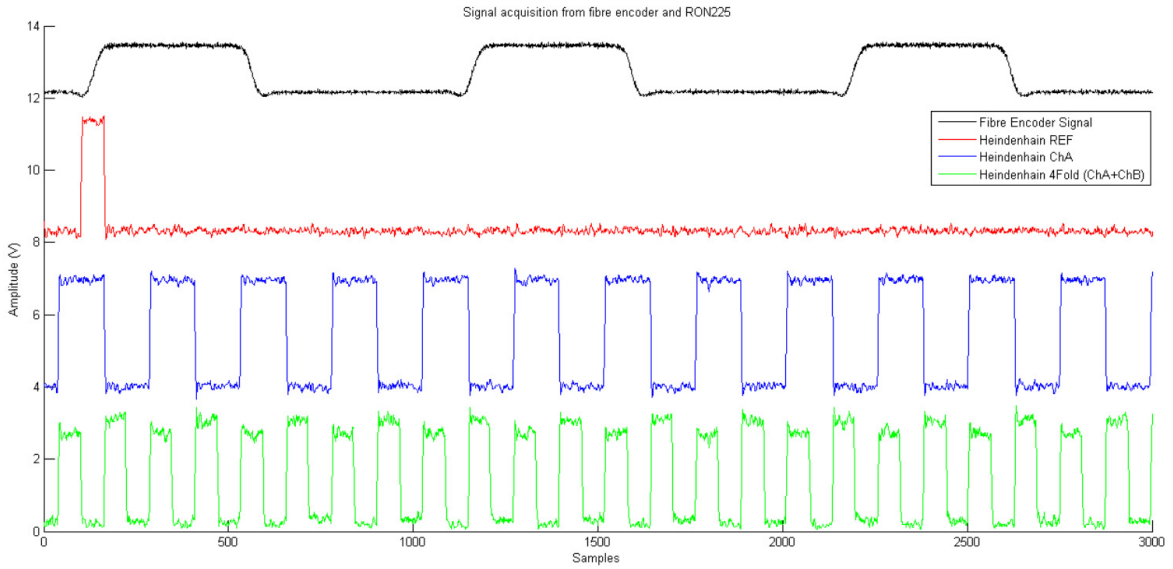

Figure 7.3: *Sampled raw signal of the fibre encoder (50mm) and RON225 performed with a Lecroy Osciloscope*

The processing applied to the raw signal starts with a low pass filter (0-10MHz), then a simple threshold detection is applied based on the mean value of the whole revolution and a hysteresis of half the standard deviation. The hysteresis and mean values for edges detection are constant over all the measurements taken. Every time the signal crosses its threshold values, an event is detected and the time between these events is recorded. This times are then analyzed in order to detect undesired effects such as the graduation errors produced by not equally spaced lines in the disk. A position study will also be carried out in order to identify mechanical errors such as disc eccentricity.

The usage of a light focuser makes the system very sensitive to defects on the disc such as scratches or dust. The system records signals which are reflected by only one slit, with a spot of about 10um, any disc imperfection of dust means a loss in the reflected light that could be detected as another slit. Traditional systems are using the light of several slits by using a window grating in front of the mobile disc to avoid this sensitivity to imperfections (see chapter 4). To overcome this potential problem, a validity check has been added to the detection algorithm. This check applies a temporal limit where the events are expected. If an undesired pulse is happens out of these limits, it is not taken into account by this processing. The time limitation uses the information of the previous temporal distances and starts waiting for an event in the defined window of T(N-1) – 10%. The polarity of the event is being expected (rising or falling edge), so only the crossing with the respective threshold is taken into account. This approach assumes a correct detection of the first events. The Fig 7.4 shows how this analysis is performed.

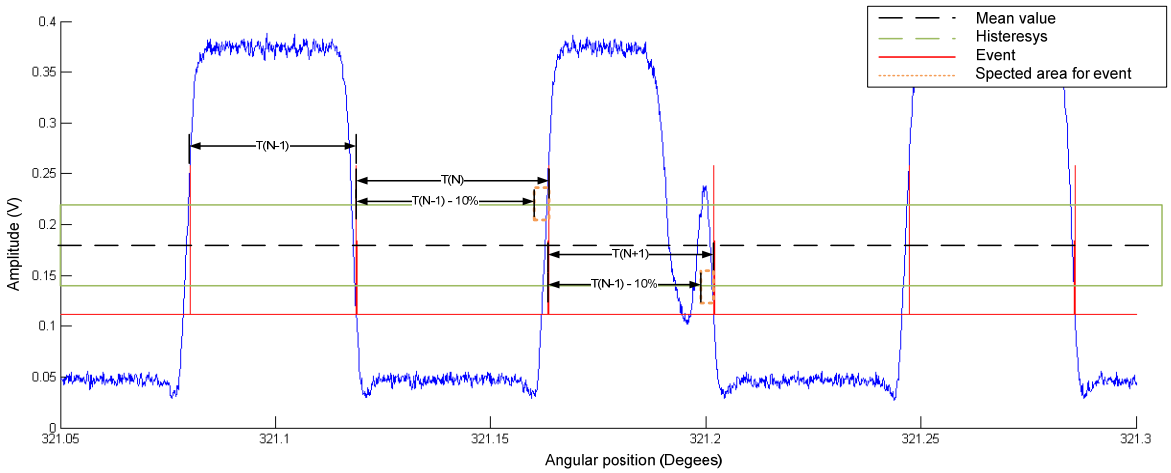

Figure 7.4: *Event validation check schematic*

This strategy helps to improve the quality of the detection by avoiding defects (see Fig 7.4). However this strategy doesn´t work properly if the imperfections are just in the expected area and if its width is significative. The Fig. 7.5 shows schematic of the signal processing steps, as well as the following analysis that are performed.

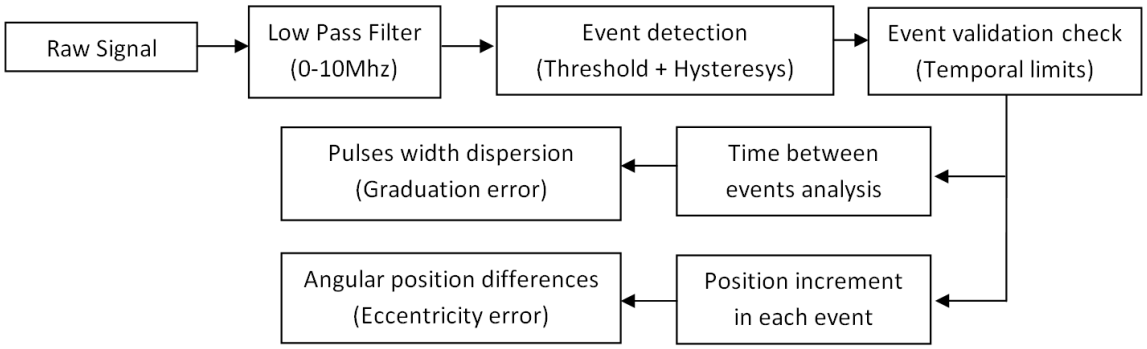

Figure 7.5: *Processing algorithm overview*

7.3 System characterization

In order to evaluate which is the accuracy that can be reached with the disk and focuser system, errors such as eccentricity and grating must be considered. To illustrate the measurements performed for this characterization, the disc V1 with its 50µm track is explained in detail.

The first measurement performed is the absolute position error of the fibre system over a whole rotation. To plot this chart, measurements from both encoders are needed (optical fiber and RON225). The absolute position of each of the encoders has been calculated considering constant angular increments when an event is detected. The difference between

the two absolute positions is plotted (blue line) on Fig. 7.6, the Ref channel of the RON225 encoder was used to mark the beginning each revolution.

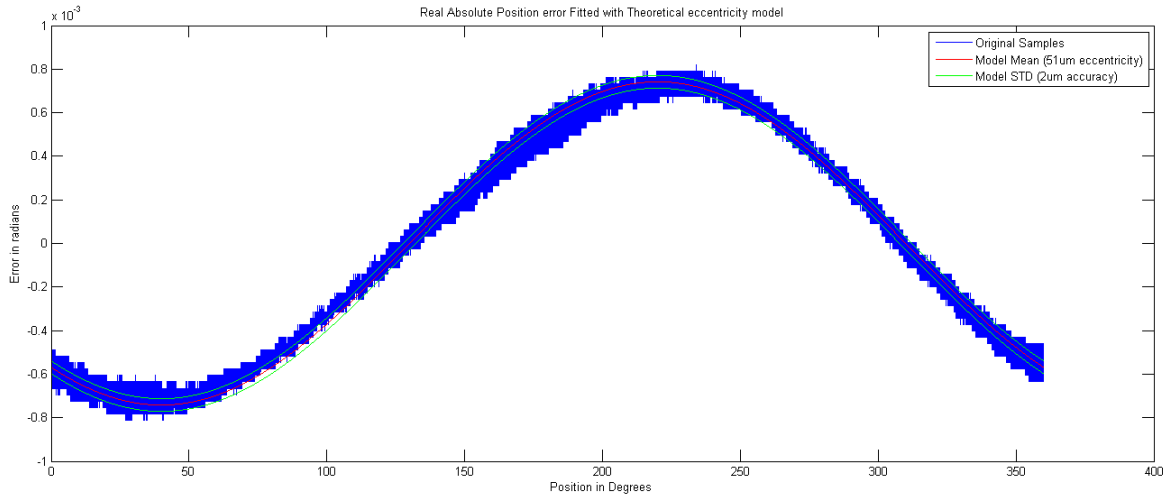

Figure7.6: *Absolute position error of the fibre encoder (50um track) compared with RON225*

The resolution of this absolute error is determined by the resolution of the RON225, which is 87µRad. This is the reason of the steps of the blue signal. To make a correlation with the most likely source of error, the eccentricity model (see section 4.2) has been used to explain the sinusoidal variation of the absolute error. By fitting this model to the absolute position error, the values of 51mm for the eccentricity (identified in section 5.7) and a grating error of 1.67e-3^{o} (29 micro radians, based on the 2um slit accuracy guaranteed by the provider) have been found. The theoretical model of an eccentricity of 51µm is shown with the red line, and the 2 green lines are showing the expected grating error of 2µm. This model emphasizes the contribution of the disc eccentricity to the inaccuracy of such system. The chart of the Fig 7.7 shows that the maximum permissible eccentricity would be 1.7µm in order to reach the desired accuracy, taking into account only the eccentricity. This permissible eccentricity must be smaller since the grating error adds up to this initial error. All these considerations force us to perform a calibration method to overcome this issue.

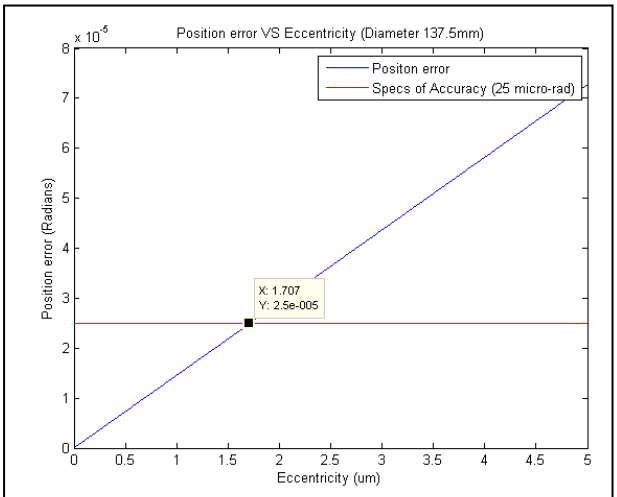

Figure 7.7: *Maximal permissible eccentricity*

Another interesting characteristic to obtain from the disk measurements is the slit width dispersion around a small area. By this, it is possible to obtain the relative position accuracy due to the grating and the event detection algorithm. This information is obtained by measuring the duration between successive events and calculating its mean value and standard deviation over a small window. The Fig 7.8 shows the duration and standard deviation between events by detecting rising and falling edges, over a whole revolution (9 turns have been averaged). The outcome is that there is a big dispersion in the measurements; the successive points are oscillating between the higher line and the lower one. This effect is due to the irregularity of the width of the chrome and glass slits. The slow variation of distance between these two lines is due the constant threshold applied, as the amplitude of the original signal varies, the event detection is not always performed on the exact half of the pulse amplitude. By applying a small running window on this signal, considering that the speed is constant over that period and calculating the standard deviation of each temporal interval, the grating and processing error over a whole turn can be drawn (see Fig 7.9). Since we are considering the standard deviation and not the mean value, the eccentricity error is not shown here. This accuracy is compared to the one obtained with the RON225 shown in blue on Fig 7.9.

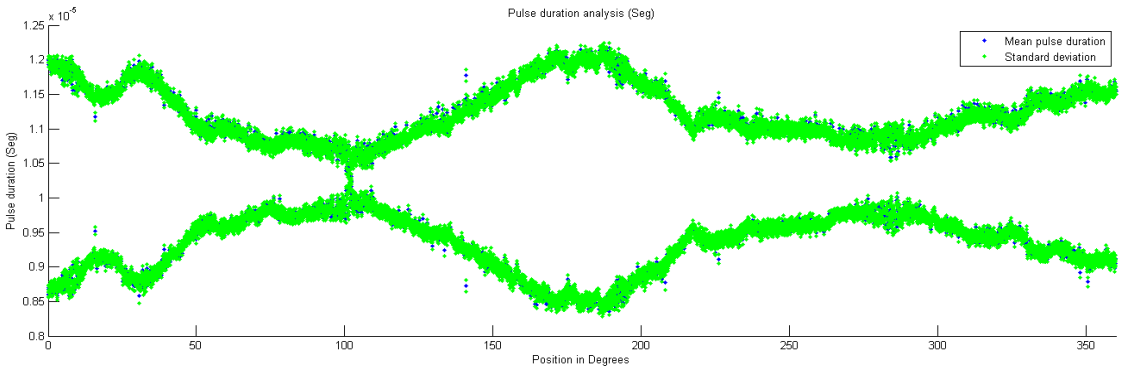

Figure7.8: *Time between events, detecting both edges (optical fibre encoder 50µm slits)*

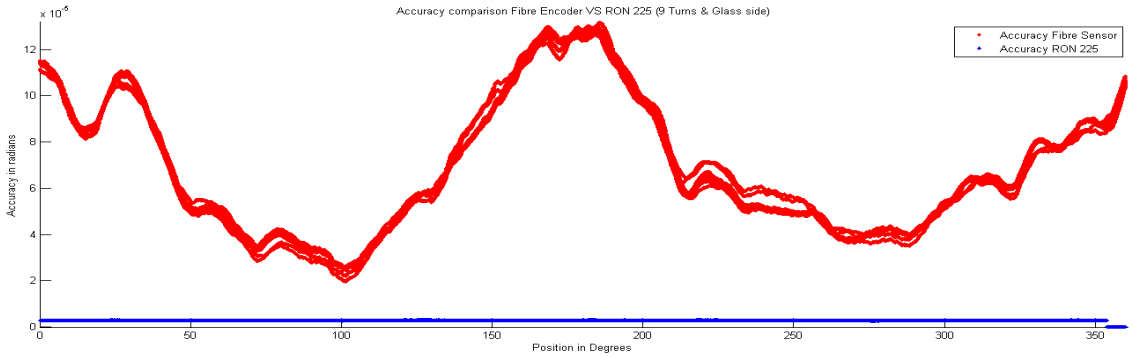

Figure 7.9: *Grating and processing accuracy comparison between the 2 encoders by detecting both signal edges*

Fig 7.9 shows that the grating error in this case is quite big in comparison to the RON225 (blue). This error is far from the specs of 25µRad, in fact, we have an error one order of magnitude bigger (120 µRad). If no calibration is performed, simple edge detection is not suitable for our application in terms of accuracy. The same analysis was performed by detecting only the rising edges of the signal. By this way, the period of the slits is taken into account instead of every edge. This reduces the resolution to half of the nominal value, but as shown in Fig 7.10 and Fig 7.11, the accuracy has been improved by about 8µRad.

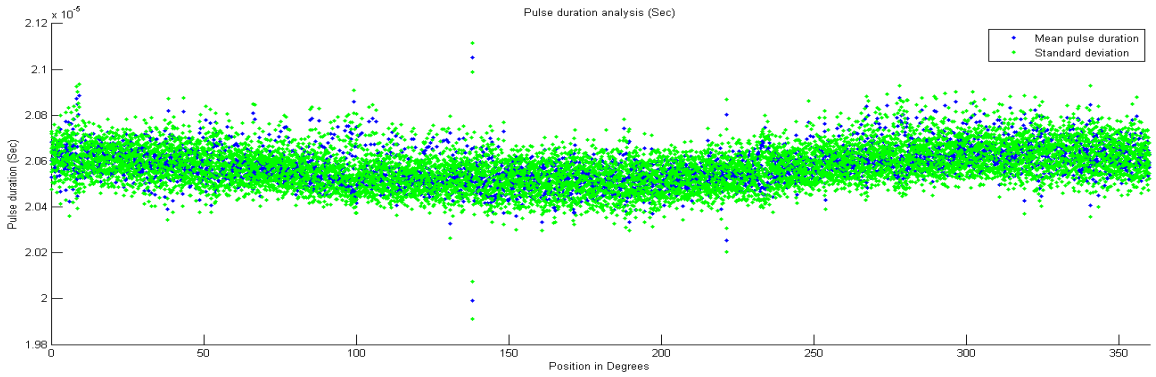

Figure 7.10: *Time between events, detecting slit period*

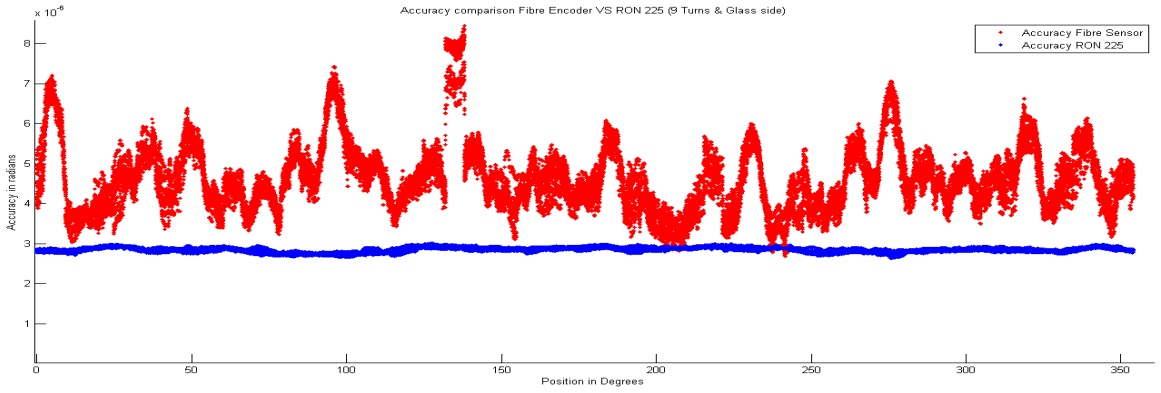

Figure 7.11: A*ccuracy comparison, detecting slit period*

With this improvement to the event duration dispersion (see Fig 7.10), it´s possible to see a slow change of the speed, the time between events varies slowly, due to the eccentricity or non uniform speed of the shaft while turning. A large improvement of the accuracy is reached by detecting the period. This time, the grating and detection error is only 8µRad, which is much smaller than the theoretical estimation based on a slits accuracy of 2um (29µRad).

This signal analysis help us to conclude that if no calibration is performed, edges detection with the V1 disc is not suitable for our application since the grating error is already bigger than the desired accuracy. However, if the period detection is used, the system is less sensitive to the amplitude changes in the original signal (due relative movement disc/focuser), and independent of the chrome width. To comply with the accuracy specified, the eccentricity must be bellow 1mm which is not easily reachable. This means that in order to reach our desired specs the design must be or very well mechanically assembled and the disk very precisely manufactured, otherwise calibration can be performed since the grating and eccentricity errors are repeatable.

7.4 Calibration method to increase the accuracy

Since a large part of the accuracy errors are repeatable, a calibration is possible to increase the accuracy. The measurements from the Heidenhain encoder will be taken as a reference for calibration and the results obtained are analyzed to estimate the accuracy improvement achieved.

Several disc revolutions are recorded by using the same starting point for reference (all the revolution information is in phase). The analysis uses the rising and falling edge detection. The error with respect to the RON225 is extracted for each revolution, considering constant angular increments. The first revolution is taken as a reference and the value of its error in each increment is obtained, this information is used to build a look-up table of correcting factors for each of the incremental steps of the disc. After calibration, the small differences between revolutions, leads to residual errors which would be the accuracy reached after the calibration. The Fig 7.12 shows a comparison of the averaged error over 9 turns obtained before and after applying this calibration procedure (blue), the desired accuracy limits are drawn in red (25µrad).

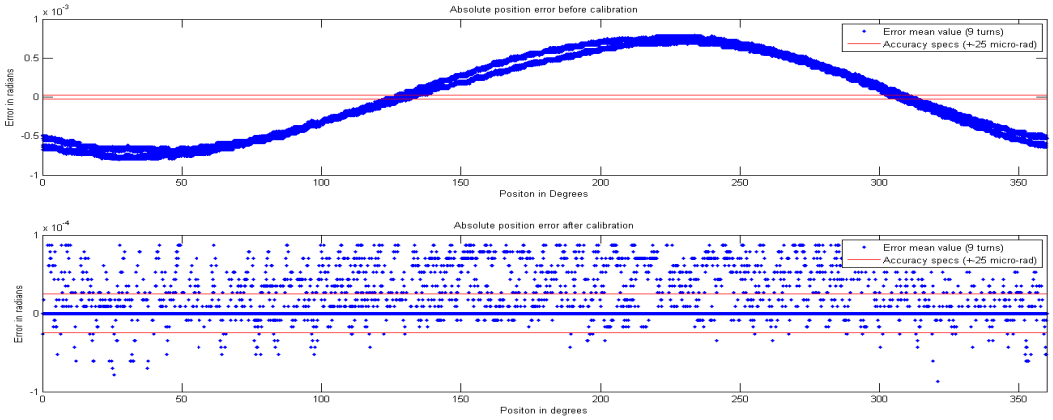

Figure 7.12: *Initial (up) and calibrated (down) accuracies reached using the Heidenhain encoder.*

The calibration improves the accuracy by a factor 10. However, the maximum residual averaged error of this 9 disc revolutions falls around ±100µrad. This could be due to the resolution of the RON225, which is 87µrad, the error points of a single revolution always falls in - 87µrad, 0 and +87µrad without intermediate values. A calibration using an encoder with higher resolution would provide better calibration information. Small vibrations can also cause a phase change in the signal due relative movement fibre/disc, this effect produces an offset in the residual error, which is in fact happening in the Fig 7.12 (down), the different turns are a bit displaced with respect to the calibration turn and that's the reason why the residual error is not completely symmetric to 0. To have a better idea of the calibration results, the Fig 7.13 shows a histogram and a Gaussian fit over it. It's shown that the distribution of the error is mainly concentrated in the desired accuracy area around ±25µRad (limited with blue lines).

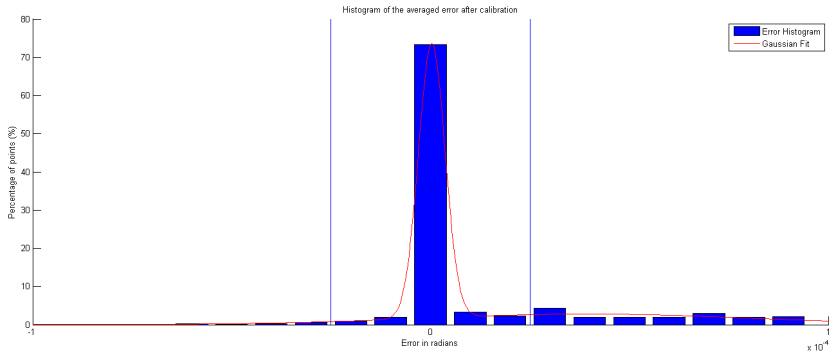

Figure 7.13: *Normalized distribution of the accuracy error, histogram (blue) and Gaussian fit (red)*

In the following pages are summarizing results of the experimentation performed with different slits sizes and by using the two detecting methods. The previous calibration procedure is applied to compensate the errors of the eccentricity and partially the grating and detection algorithm errors.

7.5 System performance validation for different sensor configurations

A) Disc Version 1 with slits of 50µm (Edges detection)

The Fig 7.14 summarizes the analysis performed in the previous sections. To be noted, the previously explained dependency of the original signal amplitude to the pulse duration detection, and therefore, to the accuracy reached (down left). The signal amplitude variation (see Fig7.14 up left) is caused for the changes of distance disc/lens during the rotation. As shown in the pulse duration analysis (left center), the standard deviation of each point is very close to its mean value, therefore the repetitively is good. Regarding the accuracy before calibration, taking into account the processing and grating, the uncertainty is around 120µRad to be added to the eccentricity (750µRad) resulting by a global uncertainty of 870µRad. After performing calibration (right center), the improvement shows a maximal error of 87µRad (the RON225 resolution), and a standard deviation around 16.7µRad, there is a small phase offset of 2µRad (error mean value) that could be due to small vibrations in the test bench. However, the desired resolution is not reached without interpolation in this configuration as it is in the order of 727µRad.

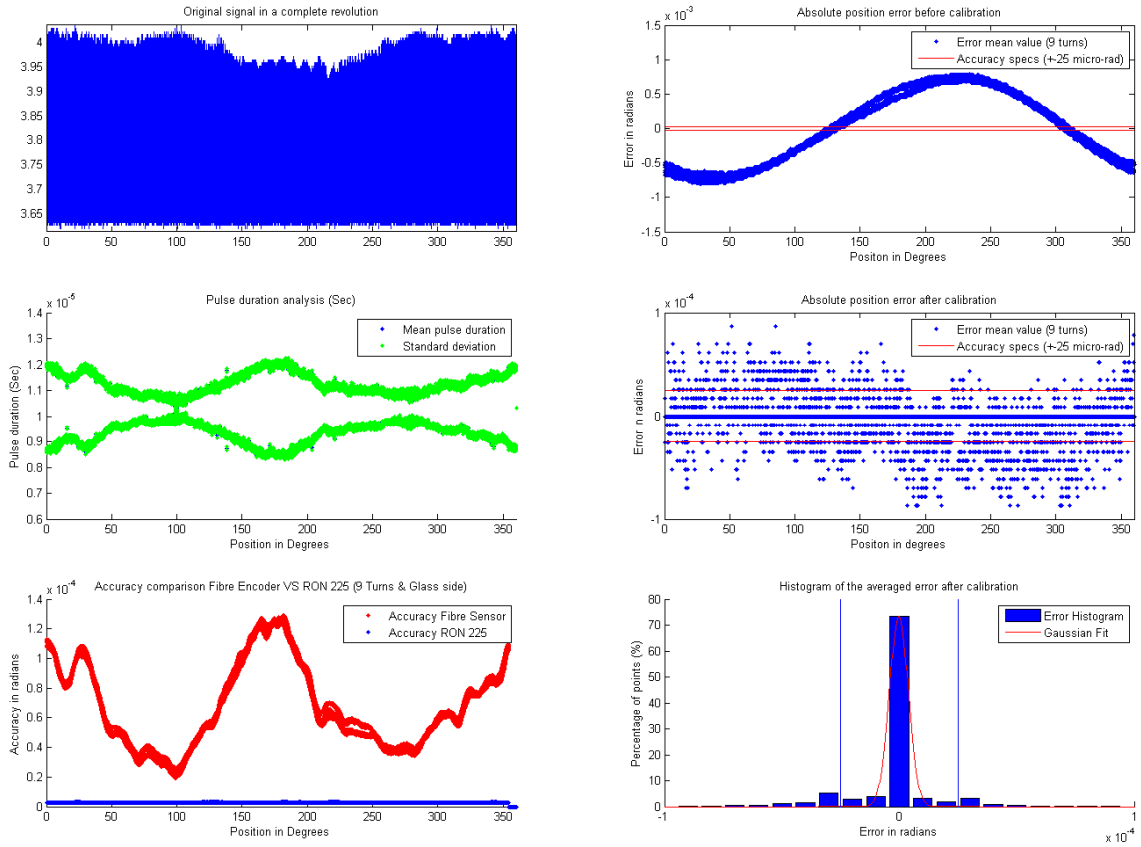

Figure 7.14: *Processing and calibration of **edges detection** with the **50µm** track of **Disc V1**.*

B) Disc Version 1 with slits of 50µm (Period detection)

This processing show that by detecting the period, the dependency of the accuracy to the original signal amplitude changes has been reduced (see Fig 7.15 left center). As shown on the pulse duration analysis, this time the points are much closer to each other forming only one line. Before calibration an improvement in the grating and processing accuracy is already visible compared to the double edge detection, this time it is about 8µRad. The results after applying calibration are exactly the same as in the previous configuration. The calibration device has not enough resolution to take these small variations into account. The improved results before calibration would mean that if the eccentricity could be reduced to less than 1µm, it would be possible to use this disc without calibration. In that case, we would reach the specs in terms of accuracy, but not in resolution with 1450µRad while the desired is 500µRad.

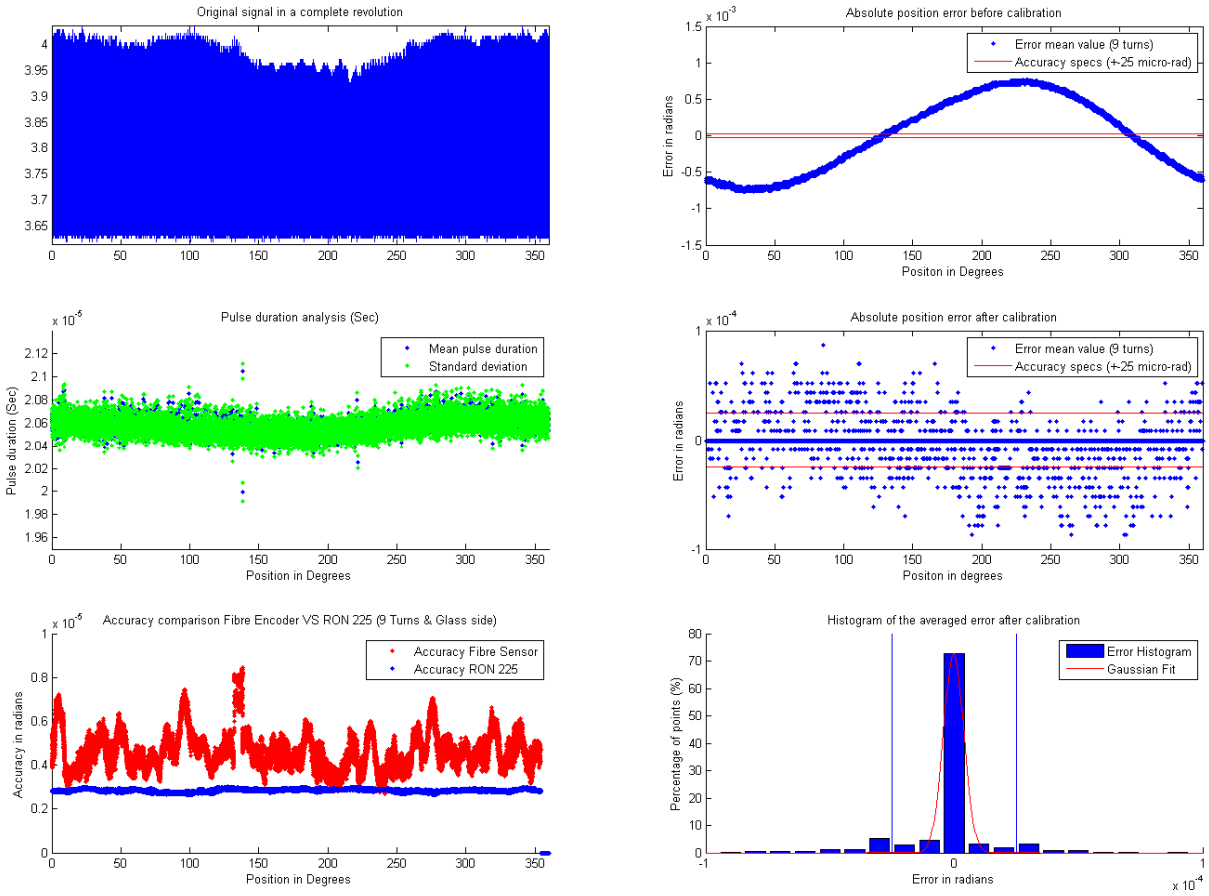

Figure 7.15: *Processing and calibration of **period detection** with the **50µm** track of **Disc V1.***

C) Disc Version 2 with slits of 10µm (Edges detection)

These measurements were performed with the version 2 disc with smaller slits (10µRad) and therefore better resolution by design. This new version has 2 slits 3 times bigger than the rest that acts as references. The pulse duration analysis (see Fig 7.6 left center) shows again the non symmetries between the chrome and glass widths. On this plot, the higher point on the left is a long pulse (first reference), the second high point is one slit hat has not been correctly detected (the defect is repeated over all the disc revolutions), and the third point (up of the legend) is the second reference. The different disc revolutions in terms of event spacing are quite repeatable since the standard deviation of every point in this chart is very close to the mean value. Regarding the accuracy before calibration, the error of the detection and the non symmetry of the slits lead to 60µRad (left down). The absolute error before the calibration is as always a sinusoid, global accuracy 1000µRad, but since there are slits bigger than the rest (1 repeatable error + 2 references) there are three angular jumps (right center). Additionally, the visible ringing signals are due to small interferences (see section 6.2). When performing the calibration, the global accuracy is improved and the maximal error reached is 87µRad with a standard deviation is around 27µRad. The measured resolution is 157µRad.

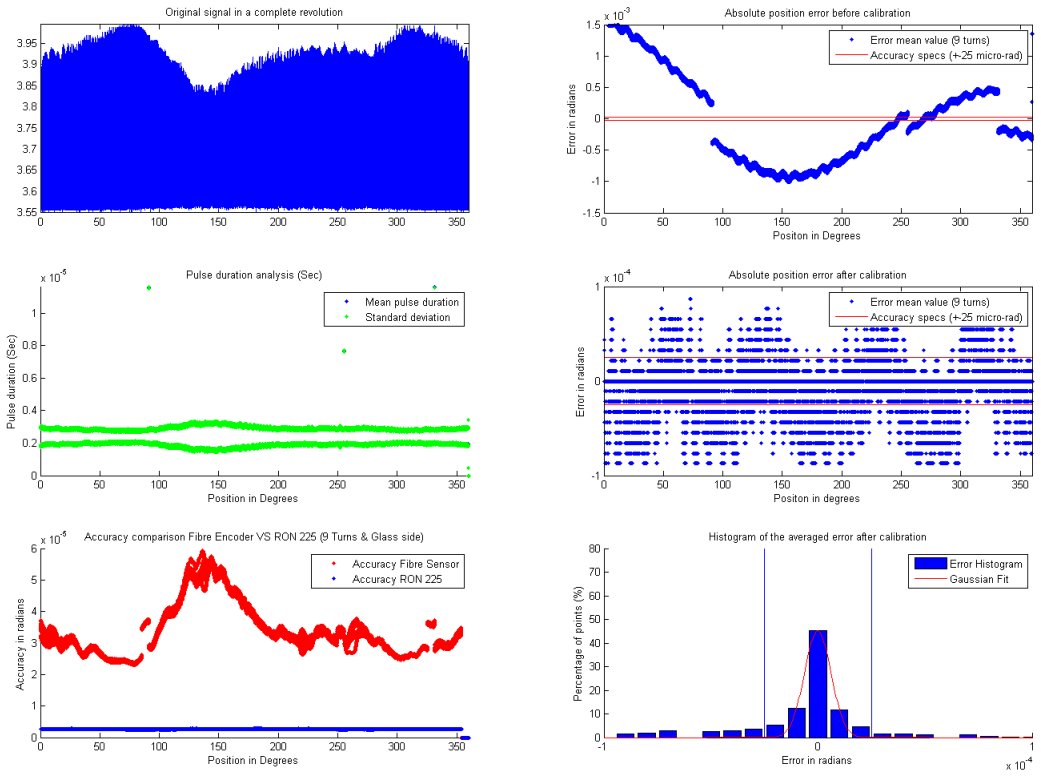

Figure 7.16: *Processing and calibration of **edges detection** with the **10µm** track of **Disc V2**.*

D) Disc V2 Slits 10µm (Period detection)

As seen before, period detection minimizes the detection algorithm error and reduces the dependency to the original signal amplitude. Therefore more reliable information of the disc manufacturing accuracy could be extracted. With this version, a improved accuracy is expected by using an improved manufacturing process than version 1. Measurements analysis on Fig 7.17(down right) is confirming this statement. Comparing the accuracy of this configuration with the 50µm period detection, the improvement is evident, whereas before it was 8µRad it now has been improved up to 0.75µRad, even better than the one obtained with the RON225(2.5µRad), (which has to be added to the eccentricity error, 750µRad). Regarding the repeatability, the pulses duration analysis (left center) shows that it's guaranteed, since the standard deviation of the different turns is quite small. The calibration procedure that avoids eccentricity error shows that certain random noise is introduced by interferences or vibrations (right center). The results obtained with the calibration are a maximal error 87µRad with a standard deviation of 27µRad and a resolution reduced to 314µRad. The grating error reduction due to the manufacturing process relax a bit the limits of the maximal mechanical eccentricity allowed; if used without calibration 1.5 µm can be tolerated, then the specs would be reached in terms of accuracy and resolution.

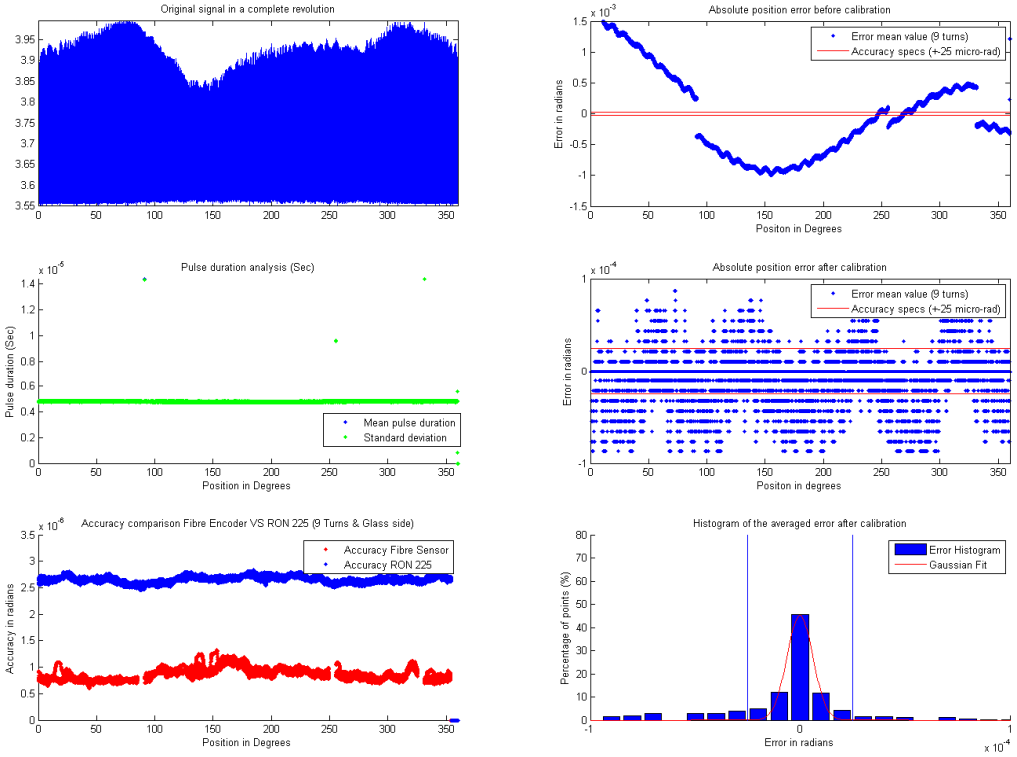

Figure 7.17: *Processing and calibration of **period detection** with the **10µm** track of **Disc V2***

E) Disc version 2 with slits of 5µm (Edges detection)

Finally the 5µm track of the version 2 disc was analyzed to determine the physical detection limits with this configuration by maximizing the resolution up to 70µRad. The measured slits are half of the spot size width, 5µm slits and 10µm spot size. Therefore the power coupled back is half of the nominal value and the recorded signal is smooth and with a sinusoid shape when a slit is detected. With such small slits, the system is much more sensitive to vibrations (phase changes between disc revolutions), and to small imperfections. The pulse duration analysis (see Fig 7.18 left center) shows 5 characteristic events that are not completely repetitive near 50, 200 and 250^{o} indicating that some slits are not correctly detected. The references are near 100 and 330^{o}. The cause the non repeatability of these events could be relative displacement of the sensor, due to vibrations, producing delays between revolutions. This relative movement makes that the defects and references are not detected the same event number; note that each of these events has two blue points, like if one of the revolutions were displaced. The accuracy with the detection algorithm and grating error is bellow 30µRad, which is better than the 10µm slits with the same algorithm. However, the calibration is not performed correctly, the accuracy after calibration (center right) has a phase jump in the middle due to the focuser relative movement, which leads to a maximal error of 140µRad, with a mean offset of 28µRad and a standard deviation of 33µRad

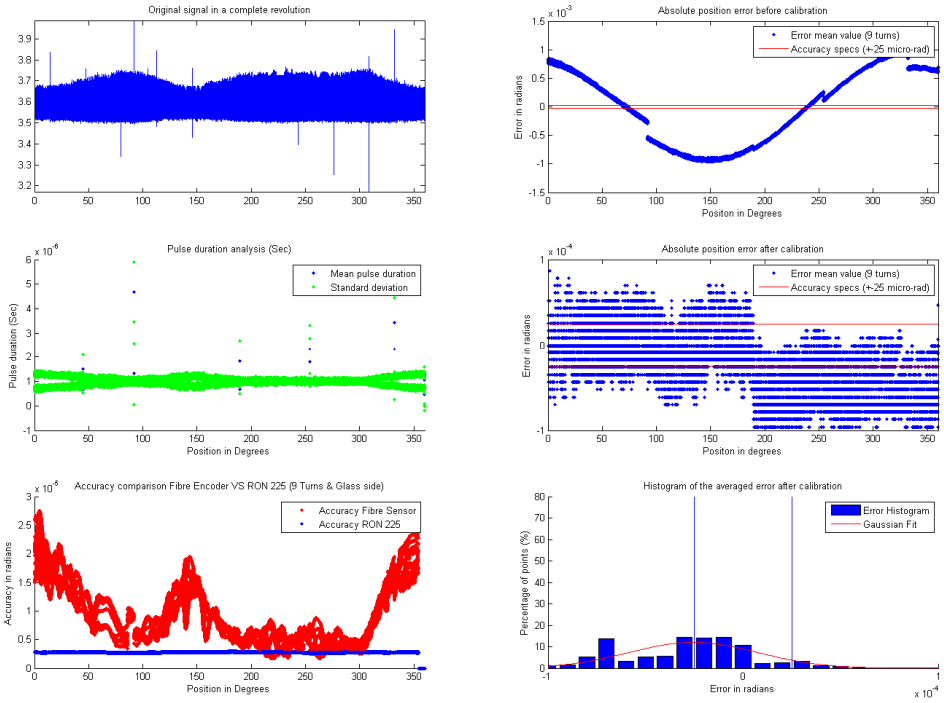

Figure 7.18: Processing and calibration of **edges detection** of the **5µm** track of **Disc V2**

F) Disc Version 2 with slits of 5µm (Period detection)

The same drawbacks as the previous detection algorithm have been identified with this version. The difference in the results is a reduced resolution (140µRad) and a better detection and grating accuracy down to 2.5µRad, period detection is not able to solve the phase changes between turns.

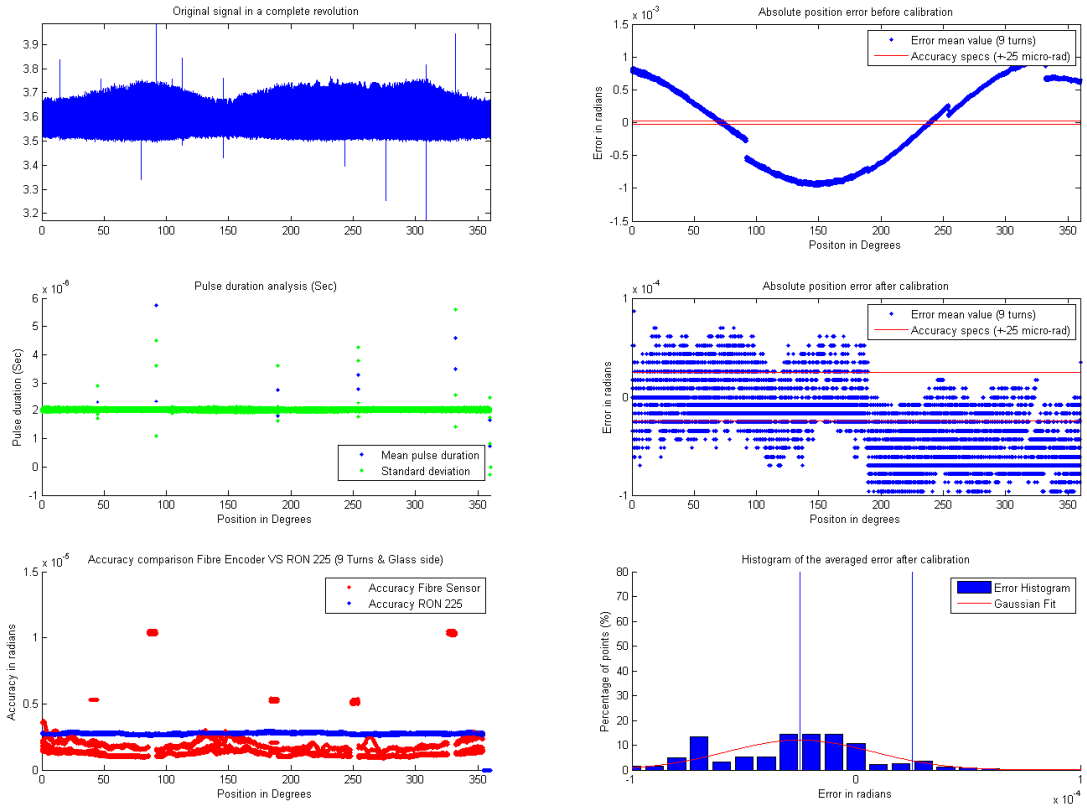

Figure 7.19: Processing and calibration of **edges detection** in the **5mm** track of **Disc V2**

7.6 Conclusions

The table 7.3 synthesizes the experimental results obtained with all the sensor configurations analyzed in section 7.5.

					Accuracy Before Calibration			Accuracy improvement after Calibration **	
Disc	Detection Method	Track (µm)	# Events	Resolution (µRad)	Processing + Grating (µRad)	Eccentricity* (µRad)	Total Uncertainty (µRad)	Measurements Offset (µRad)	Measurements Uncertainty (µRad)
V2	Edges	5	90000	69.8	27	750	777	-28	33
	Period		45000	139.6	2.5	750	752.5	-28.3	33
	Edges	10	40000	157.1	60	750	810	-5	27
	Period		20000	314.2	0.75	750	750.75	-5.6	27.2
V1	Edges	50	8640	727.2	120	750	870	-2	16.7
	Period		4320	1454.4	8	750	758	-2	17
	* Experimental eccentricity: 50µm								
	** Calibration device Heidenhain RON225: Resolution 87µRad, Accuracy: 24µRad								
	*** System desired performance: Resolution 500µRad, Accuracy 25µRad								

Table 7.3: *Results of the experimental verification for the different potential sensor configurations*

The results of these experimental validations drive us to conclude that the configuration that fits the initial specifications in terms of resolution, accuracy and repeatability is based

on the usage of the version 2 disc with the 10μm track. The measurements have shown a better immunity to vibrations than the 5mm slits and no phase displacement with very repetitive measurements. The eccentricity errors where successfully compensated with the calibration algorithm performed. However a calibration device with higher resolution and accuracy must be used in order to provide a more accurate encoder calibration map. The resolution of the RON225 was not enough to sense the differences between the two detection algorithms performed with the 10μm slits. The uncertainty of this device is already in the below of the desired accuracy (8μm) (note that the final accuracy without calibration depends highly of the eccentricity). With regard to which side of the disc to use, the glass side would be better since the chrome protected by the glass is always clean, however, the experimental validation shown similar results by using the chrome side.

Along the thesis development, several configurations have been studied to reach the desired specifications. Designing the system with a power budget large enough to compensate the aging of the different components. A power margin has been left on the lasers to overcome the expected increases of the RIA, for the SMF used in the final prototype, and the potential darkening of the lenses. The design has been optimized in terms of power coupling, tolerances, and detection capability by characterizing each approach in detail and providing a frame of mechanical specifications to make the different possible configurations work properly. The most promising approach is based on a lens system that has been deeply studied. Finally, the accuracy and resolution has been analyzed with different detection methods and calibration has been performed in order to compensate the effect of the disc eccentricity error, obtaining very promising results.

7.6.1 Characteristics of the final system obtained

The final system performance reached is the following:

Resolution: 157μRad
 # Edges in a disc revolution: 40.000
 # Channels: 1
 # Turn References: 2
Disk Diameter: 140 mm
Light spot size: 10μm
Accuracy without calibration: 750.75μRad (Algorithm: 0.75μRad; Ec.50μm: 750μRad)
Accuracy with calibration: 27μRad (Using Heidenhain RON225 for calibration)
Max Temp: 200^{o}C
Ultra High Vacuum Compatible: 1x10^{-10}Torr.

7.6.2 Optical position sensor integration into the VWS and future work

The integration of the encoder system is performed by a mechanical team. Basically a disc holder is attached to the shaft at the opposite side of the motor. The disc holder is flexible to avoid stress on the glass due to the high temperatures inducing dilatation of metals. Regarding the focuser, the prototype will be flexible enough to use both systems (Thorlabs and Schafter). The focusers are inserted in a metallic jacket and then in one of the holes of the metallic piece in front of the disc (there are several holes, one per track). The assembly is done in a way that the distance focuser/disc can be calibrated in the laboratory with an accuracy of 10µm. Once reached the suitable distance, the focuser system is fixed with screws. The optical fiber for UHV crosses the scanner from one side to the other through the external part of the assembly, avoiding the folk's trajectory. The fiber will be protected with a tube or cover.

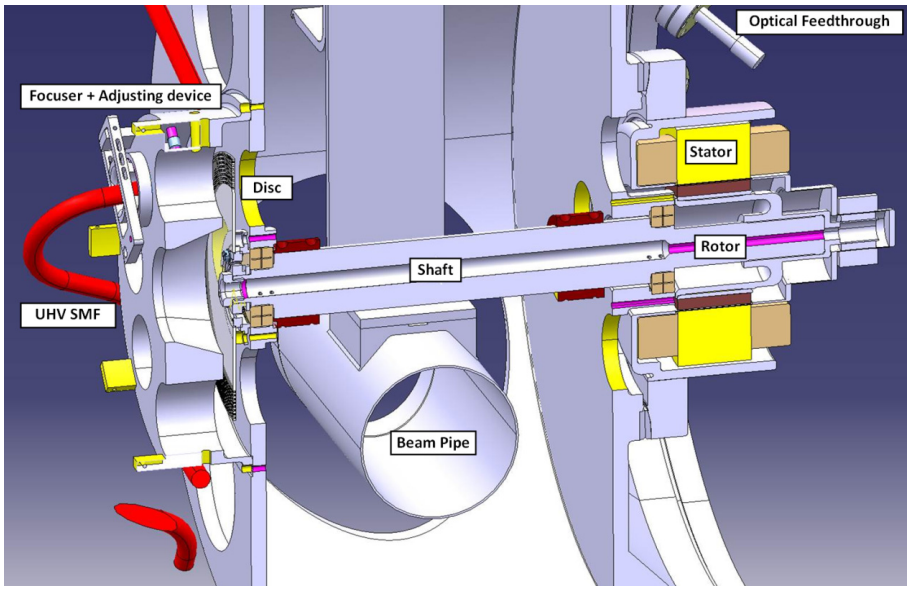

Figure 7.20: *Integration of the position sensor in the Wire Scanner.*

Regarding future improvements, the system could be better calibrated by adding redundancy with another focuser in order to perform a self calibration directly mounted on the working shaft or by applying a high resolution and accuracy calibration procedure to the complete prototype in order to extract a very precise encoder map, which would include all the sources of errors. Regarding the processing, more intelligence could be applied (dynamic thresholds for example) in order to process off-line the signals and be able to detect the slits more accurately. Using these techniques, the 5µm track could be used if the phase errors would be compensated. Further studies need to be concluded to check if a specific type of calibration needs to be developed for the final system.

Bibliography

[1] L. Evans, (ed.) and P. Bryant, (ed.), LHC Machine, JINST 3 (2008) S08001.

[2] ATLAS Collaboration, ATLAS Experiment at the CERN Large Hadron Collider.,JINST 3:S08003 (2008) 1–437.

[3] ALICE Collaboration, K. Aamodt et al., The ALICE experiment at the CERN LHC,JINST 3 (2008) S08002.

[4] LHCb Collaboration, A. Alves et al., The LHCb Detector at the LHC,JINST 3 (2008) S08005.

[5] CMS Collaboration, R. Adolphi et al., The CMS experiment at the CERN LHC,JINST 3 (2008) S08004.

[6] S.Y. Lee. *Accelerator Physics, Second Edition. 2004 World Scientific.* Link

[7] F. Roncarolo. *Accuracy of the Transverse Emittance Measurements of the CERN Large Hadron Collider. 2005 Politecnico di Milano (Italie) Link*

[8] E.B. Podgorsak. *Radiation Phisics for Medic al Physicist. 2010 Biological and Medical Phicics, Biomedical Engineering*. Link

[9] W. Herr and B. Muratori, *"Concept of luminosity", 2005. Link*

[10] L. Ponce et al. *LCH* Proton Beam Diagnostics Using synchrotron radiation. *2004 CERN Accelerators and beams department*. Link

[11] B. Denhing et al. *Accuracy of the SPS transverse emittance monitors. 7th European Workshop on Beam Diagnostics and Instrumentation for Particle Accelerators. France 2005. Link*

[12] G. Burtin, J. Camas, G. Ferioli, R. Jung, J. Koopman, R. Perret, A. Variola and J. M. Vouillot, *The luminescence profile monitor of the CERN SPS, CERN-SL-2000-031 BI, presented at European Particle Accelerator Conf., Vienna (Geneva, E.P.S., 2000).* Link

[13] C. Fischer, J. Koopman, *Ionization profile monitor tests in the SPS, Proc. European Particle Accelerator Conf., Vienna, 2000, CERN-SL-99-046 BI (2000).* Link

[14] F.Roncarolo et al. *Synchotron Radiation Measurements at the CERN LHC. Prod. DIPAC 2011, Germany.* Link

[15] J. Bosser. *Beam Instrumentation. 1994 Services Educatifs-Engeignement Technique.*

[16] B. Bouchet et al. Wire scanners at LEP. *Proceedings of the 1991 IEEE Acc. Conference, San Francisco*, 1991. Link

[17] S. Burger et al. *The **PS Booster** Fast Wire Scanner. Proceedings of DIPAC2003, Mainz,Germany*, 2003. Link

[18] S.E. Forde. *Wire Scanner Motion Control Card. 2007 Bergen University Collete (Norway)*. Link

[19] A. Lokhovitskiy et al. *Fast Wire Scanner Calibration. Proceedings of DIPAC2009, Switzerland 2009*. Link

[20] B. Dehning et al. *Carbon Fiber Damage in Particle Beam. HB2010 conference. Switzerland 2010.* Link

[21] M. Koujili et al. *Fast and High Accuracy Wire Scanner. Proceedings of DIPAC2009, Switzerland 2009*. Link

[22] M. Koujili et al. "*Design of an actuator for the fast and high accuracy Wire Scanner," Electric Machines & Drives Conference (IEMDC), 2011 IEEE International*, vol., no., pp.1450-1455, 15-18 May 2011. Link

[23] M. Kouijili. PhD Thesis to be published

[24] Richard J. Graetz. *"On-axis Shelf-Calibration of Angle Measurements Errors in Precision Rotary Encoders". Master Thesis*. February 2011. Link

[25] P.A. Orton et al. *"Automatic shelf-Calibrationi of an Incremental Motion Encoder". IEEE Instrumentation and Measurements Budapest, Hungray, May21-23,2001.* Link

[26] T Watanabe1, H Fujimoto, and T Masuda. *"Self-calibratable rotary encoder". Journal of Physics: Conference Series, 13:240–245, 2005*. Link

[27] X. D. Lu and D.L. Trumper. "*Self-calibration of on-axis rotary encoders*". CIRP Annals - Manufacturing Technology, 56(1):499 – 504, 2007 Link

[28] F. Berghams et al., "*An Introduction to Radiation Effects on Optical Components and Fiber Optic sensors", Springer, Netherlands (2008), pg. 127-165* Link

[29] J. Kuhnhenn and U. Weinand. *"Irradiation Test of a Fujikura multi-mode fibre (RRMA 0S 0131/ TNo.2)". Fraunhofer-Institut, 08/2010.*

[30] J. Kuhnhenn and U. Weinand. *"Irradiation Test of a Fujikura single-mode fibre (ID:RRSMFB380A)". Fraunhofer-Institut, 08/2010.*

[31] J. Kuhnhenn and U. Weinand. "Irradiation test of a Draka graded-index optical fibre (ID: 400019000570040)". *Fraunhofer-Institut, 08/2010*

[32] J. Kuhnhenn and U. Weinand. "Irradiation test of a Draka single-mode fibre (ID:100019011840020)". *Fraunhofer-Institut, 08/2010*

[33] V. Agoritsas et al The Fast Wire Scanner of the Cern PS.1995 Link

[34] C. Bovet et al. *Wire Scanners For **LHC**. LHC-Project-Note-108*, 1997. Link

[35] C. Fisher et al. *Comparative Transverse Distribution Measurements between the New SPS Rest Gas Ionisation Monitor and the Wire Scanner Monitor. 9th European Particle Accelerator Conference.Switzerland 2004.* Link

[36] F. Roncarolo, B. Denhing. *Transverse Emittance blow-up due to the operation of wire scanners. Analytical predictions and measurements. 21st IEEE Particle Accelerator Conference. USA 2005.* Link

[37] T. Lefevre et al., *First Beam Measurements with the LHC Synchotron Light Monitors. 2010 Proc. IPAC Kyoto, Japan.* Link

[38] Norbert C. Cheung. *An innovative Method to increase the resolution of Optical Encoders in motion servo systems. Power Electronics and Drive Systems, 1999. PEDS '99.* Link

[39] Ching-Jung Yang et al, *ASIC with interpolator for incremental optical encoders. 2003 7th Internationoal conference on Mechatronics Technology.* Link

[40] Byeong Ha Lee et al. *"Interferometric Fiber Optic Sensors". Sensors 2012, 12, 2467-248, February 2012.*

[41]"Precission Machine Design" 1992 Alexander H Slocum.

[42] Thijs Wijnands Et al. "Radiation Tolerant Optical Fibers: From Sample Testing to Large Series Production" Journal of lightwave technology, Vol. 29, No. 22, November 15, 2011.

[43] Loori Moore "Single Mode Fiber Coupling: Sensitivities and Tolerancing", opti521 Tutorial. December 8,2006